

RUPRECHT-KARLS-UNIVERSITÄT HEIDELBERG



KIRCHHOFF-INSTITUT FÜR PHYSIK

Dissertation  
submitted to the  
Combined Faculties for the Natural Sciences and for Mathematics  
of the Ruperto-Carola University of Heidelberg, Germany  
for the degree of  
Doctor of Natural Sciences

presented by

Dipl. Phys.: Michael Schottner  
born in: Heidelberg, Germany  
Oral examination: 18<sup>th</sup> December, 2002

**Algorithms**  
**for the application of**  
**Hartmann-Shack wavefront sensors**  
**in ophthalmology**

Referees: Prof. Dr. Josef F. Bille  
Prof. Dr. Brenner

## **Abstract**

The topic of this thesis is the development of procedures and algorithms for applications of Hartmann-Shack wavefront sensors in ophthalmology.

Two compact systems were built to do measurements of the entire optical system of the human eye. Automatic pre-correction modules were integrated to compensate a sphere of  $-11.25$  dpt to  $3.25$  dpt and an astigmatism of up to  $4$  dpt.

In the field of image processing, procedures were developed, which allow to recognize strongly aberrated wavefronts. Numerous algorithms are presented, which are suitable to use the extensive raw data to get some significant coefficients. In addition to a modal approach with Zernike Polynomials, alternative possibilities of representation of the wavefront with non-modal and heterogeneous procedures are presented.

Within the framework of this thesis, extensive measuring software was developed. An additional program that simulates image data was developed, with which a great number of parameters can be varied and aberrations in the form of Zernike Polynomials up to 10th arrangement can be used.

In addition to simulations, results of measurements at representative human eyes are presented.

Finally, a conclusion and a view on possible future evolution is given.

## **Zusammenfassung:**

Diese Arbeit befasst sich mit Verfahren und Algorithmen für die Anwendung von Hartmann-Shack-Wellenfrontsensoren in der Ophthalmologie. Für die Durchführung der Experimente wurden zwei kompakte Systeme aufgebaut, die Messungen der Aberrationen des gesamten menschlichen Auges ermöglichen. Zur Erweiterung des Messbereiches wurden automatische Vorkorrektur-Module entwickelt, die Defokus und Astigmatismus kompensieren. Damit sind Untersuchungen an Augen mit einer Sphäre zwischen  $-11.25$  und  $+3.25$  Dioptrien und einem Astigmatismus von bis zu  $4$  Dioptrien möglich.

Im Bereich der Bildverarbeitung wurden Verfahren entwickelt, die es erlauben, auch sehr stark verzerrte Wellenfronten zuverlässig zu erkennen. Zahlreiche Algorithmen werden vorgestellt, die dazu geeignet sind, die umfangreichen Rohdaten auf wenige anschauliche Maßzahlen zu komprimieren. Neben der Entwicklung in Zernike-Polynome werden auch alternative Möglichkeiten der Darstellung der Wellenfront mit nicht-modalen und heterogenen Verfahren vorgestellt.

Im Rahmen der Arbeit wurde umfangreiche Messsoftware entwickelt, in die alle behandelten Algorithmen integriert wurden. Zusätzlich wurde ein Programm erstellt, das Messbilder simuliert, bei denen eine Vielzahl von Parametern variiert werden können und Aberrationen in Form von Zernike-Polynomen bis zu  $10$ . Ordnung möglich sind.

Neben Simulationen werden auch Ergebnisse von Messungen an repräsentativen menschlichen Augen vorgestellt.

Abschliessend wird eine Zusammenfassung und ein Ausblick auf denkbare zukünftige Entwicklungen gegeben.

# Contents

<b>1</b>	<b>Introduction</b>	<b>1</b>
<b>2</b>	<b>The human eye</b>	<b>3</b>
2.1	Anatomy of the human eye . . . . .	4
2.1.1	Cornea . . . . .	4
2.1.2	Crystalline lens . . . . .	5
2.1.3	Iris . . . . .	5
2.1.4	Retina . . . . .	6
2.2	Transmittance of the optical media . . . . .	7
2.3	Reflectance of the retina . . . . .	8
2.4	Main refractive errors . . . . .	8
2.4.1	Myopia . . . . .	9
2.4.2	Hyperopia . . . . .	9
2.4.3	Astigmatism . . . . .	9
2.4.4	Spherical Aberration . . . . .	10
2.4.5	Chromatic Aberration . . . . .	10
2.5	Visual Acuity . . . . .	11
2.6	Corrections of the optical aberrations . . . . .	13
2.6.1	Eye glasses . . . . .	13
2.6.2	Contact lenses . . . . .	13
2.6.3	Refractive surgery . . . . .	13
<b>3</b>	<b>Principles of wavefront sensors</b>	<b>14</b>
3.1	Hartmann test . . . . .	14

---

3.2	Hartmann-Shack wavefront sensor . . . . .	16
3.3	Extensions of the HSS . . . . .	17
3.3.1	General compensation of aberrations . . . . .	18
3.3.2	Sphere compensation . . . . .	19
3.3.3	Cylinder compensation . . . . .	19
<b>4</b>	<b>Optical setup of the devices</b>	<b>21</b>
4.1	Basic components of the wavefront sensors . . . . .	21
4.1.1	Lens array . . . . .	22
4.1.2	Light source . . . . .	23
4.1.3	Camera . . . . .	23
4.2	Extensions of the wavefront sensors . . . . .	23
4.2.1	Laser monitoring . . . . .	23
4.2.2	Polarization elements . . . . .	23
4.3	Optical setup of System 1 . . . . .	24
4.3.1	Pinhole . . . . .	24
4.3.2	Pupil observation system . . . . .	24
4.3.3	Sphere compensation . . . . .	25
4.3.4	Optical setup . . . . .	26
4.4	Optical setup of System 2 . . . . .	27
4.4.1	Sphere compensation . . . . .	27
4.4.2	Cylinder compensation . . . . .	28
4.4.3	Optical setup . . . . .	29
<b>5</b>	<b>Algorithms for the use with wavefront sensors</b>	<b>31</b>
5.1	Image preprocessing . . . . .	31
5.2	Spotfinding algorithms . . . . .	34
5.2.1	Spot centering . . . . .	35
5.2.2	Static spotfinding . . . . .	36
5.2.3	Adaptive spotfinding . . . . .	36
5.3	Modal wavefront estimation . . . . .	38
5.3.1	Estimation of wavefront deviations . . . . .	38

---

5.3.2	Development of the wavefront in Taylor Polynomials . . . . .	43
5.3.3	Development of the wavefront in Zernike Polynomials . . . . .	45
5.4	Zonal estimation . . . . .	48
5.5	Mixed estimation . . . . .	50
<b>6</b>	<b>Wavefront analysis software</b>	<b>53</b>
6.1	HSS Analysis 2.x . . . . .	53
6.2	HSS Analysis 3.x . . . . .	59
6.3	HSS Real 1.x . . . . .	60
6.4	HSS Simulator 1.x . . . . .	61
6.4.1	General parameters . . . . .	61
6.4.2	Generating wavefronts . . . . .	63
6.4.3	Spot shapes . . . . .	63
6.4.4	Additional pattern modifications . . . . .	65
6.4.5	Output . . . . .	65
6.4.6	Effects of wavefront distortions . . . . .	66
<b>7</b>	<b>Simulations with the algorithms</b>	<b>68</b>
7.1	Spot finding algorithm . . . . .	68
7.1.1	Underground . . . . .	69
7.1.2	Noise . . . . .	70
7.1.3	Spot size . . . . .	71
7.1.4	Spot shape . . . . .	72
7.2	Limits . . . . .	73
7.3	Speed optimization . . . . .	74
<b>8</b>	<b>Experiments with the wavefront sensor</b>	<b>77</b>
8.1	Artificial eye . . . . .	77
8.2	Selected patients . . . . .	78
8.2.1	Example 1 . . . . .	78
8.2.2	Example 2 . . . . .	79
8.2.3	Example 3 . . . . .	80
8.2.4	Example 4 . . . . .	81

---

8.3	Time series . . . . .	82
8.4	Spherical aberration . . . . .	83
8.5	Comparison with VISX WaveScan <sup>TM</sup> . . . . .	84
<b>9</b>	<b>Summary and discussion</b>	<b>85</b>
<b>A</b>	<b>Calculation of Zernike polynomials</b>	<b>87</b>
A.1	Calculation . . . . .	87
A.2	Polar coordinates . . . . .	88
A.3	Cartesian coordinates . . . . .	91
<b>B</b>	<b>Important software functions</b>	<b>96</b>
B.1	Creation of spots . . . . .	96
B.2	Calculation of z-values . . . . .	97
B.3	Calculation of spot positions . . . . .	100
	<b>References</b>	<b>106</b>
	<b>Acknowledgements</b>	<b>110</b>



# Chapter 1

## Introduction



**Figure 1.1:** Konrad von Soest (1404)

A human gathers most of the information about the environment with the eyes. Therefore every loss of vision quality hardly influences our daily life. Directly after the invention of the first optical lenses, efforts were undertaken to use them for correction of common refractive errors like nearsightedness and farsightedness. Although these early glasses were not suitable to regain full vision with a natural field of view, the benefit for the users was immense.

In the last century, numerous improvements of the glasses were made. New technologies allow to produce thin lightweight glasses with anti-reflex coatings, that mean more comfort for everyone who wears them. The ability to correct optical errors of the eye is limited by the parameters that are used to manufacture these glasses. This data consists of only a few numbers, that are determined by an optician or optometrist. Since the optical properties of individual eyes can vary strongly, not every eye can be fully corrected using these few numbers. New optical products like bifocal and multifocal glasses or soft contact lenses do not exceed these limitations, too.

First efforts to correct individual optical errors were undertaken only in recent years. New technics of refractive surgery and contact lens design allow to help those people for whom the standard corrections are not sufficient. These correction procedures require detailed information about the aberrations of the eye. The suitable instrument, with which an optician can obtain these information, is the Hartmann-Shack wavefront sensor. Its optimization is the topic of this thesis.

The second chapter gives a short description of the optical properties of the human eye as far as they are of interest for the understanding of the following chapters. Special attention is given to the anatomical properties, which are important for the optical setup

of the wavefront sensor device. Another part of chapter two is the influence of aberrations like shortsightedness or farsightedness on the visual quality and how they can be corrected.

In chapter 3 the functionality of wavefront sensors is described. After a short overview of the basics of wavefront sensing, the possibilities to compensate strong aberrations within the device is topic of this chapter. The integration of a precompensation of sphere and cylinder is shown.

The optical setup of the devices used for the experiments in this thesis are described in chapter 4. It is started with the basic components and the special requirements for measurements at the human eye. A description of the integration of some extensions follows. Finally, detailed information about the two systems with their special properties is given.

Topic of the fifth chapter are all algorithms, that are used to calculate significant results from the raw data of a wavefront sensor, that consists only of an image with a spot pattern. The main part of the chapter deals with the image procession and the recognition and assignment of the spots. After this, the calculation of wavefront gradients is described. The chapter concludes with the possibilities to use these gradients to estimate the wavefront and to reduce this wavefront data to some significant values.

These algorithm were integrated in computer programs. All these programs were developed in the framework of this thesis. A full description of the software is given in chapter 6. The programs are: HSS Analysis 2.x and HSS Analysis 3.x, that are responsible for a complete analysis of wavefront data, HSS Real 1.x, that is optimized for real-time application, and HSS Simulator 1.x, that was used for test of the other three programs.

Chapter 7 shows the results of simulations, that have been done in combination with simulated spot patterns and the analysis software. The first part deals with the effect of general image parameters concerning the image quality to spot finding algorithm. After this, the limits of the algorithm are analyzed. The chapter concludes with an optimization of the algorithm's speed. The time required for the execution of the time-critical software modules is analyzed and possible accelerations are explained.

In chapter 8 results of measurements at four selected patients are shown. Additional, examples for examinations of time series and spherical aberrations are given.

A summary and a discussion is given in chapter 9. Additionally, some ideas for possible future development are shown.

Two thesis is completed by two appendices. The first appendix gives additional information about the calculation of Zernike Polynomials. Significant software functions are listed in the second appendix.

# Chapter 2

## The human eye

Comparing with other optical devices like photo cameras the human eye seems to be a very simple device because it only consists of a few optical components. Nevertheless the human eye is a high performance vision system. The basics of anatomy, physiology and optics of the human eye are described in this chapter as far as it is important for the understanding of the following chapters.

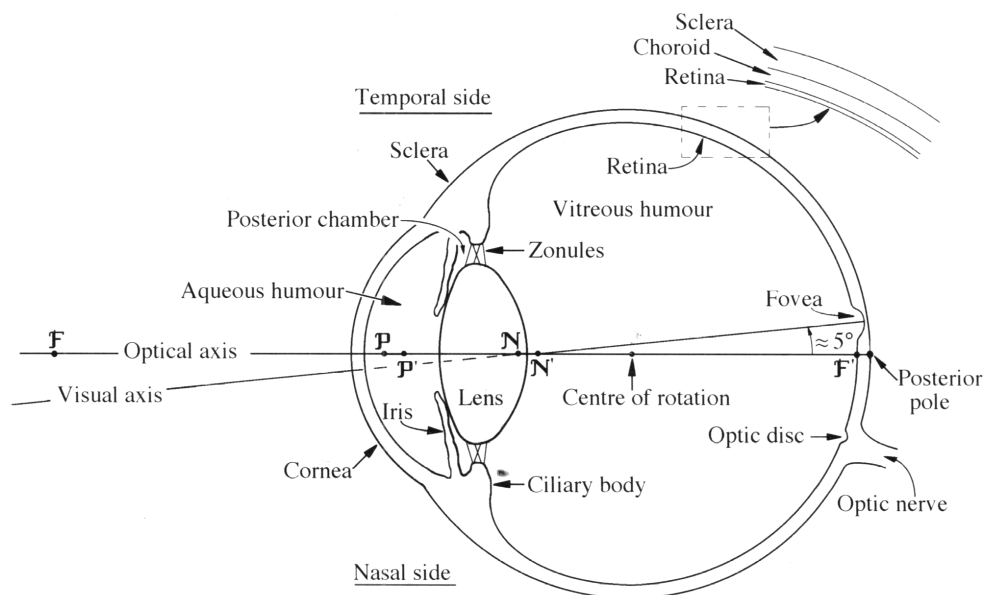


Figure 2.1: Anatomy of the human eye [Atc00]

## 2.1 Anatomy of the human eye

Four components are of special interest, regarding the optical properties of the eye. These are the cornea, the iris, the crystalline lens and the retina (see fig. 2.1). The dimensions of the components are shown in fig. 2.2.

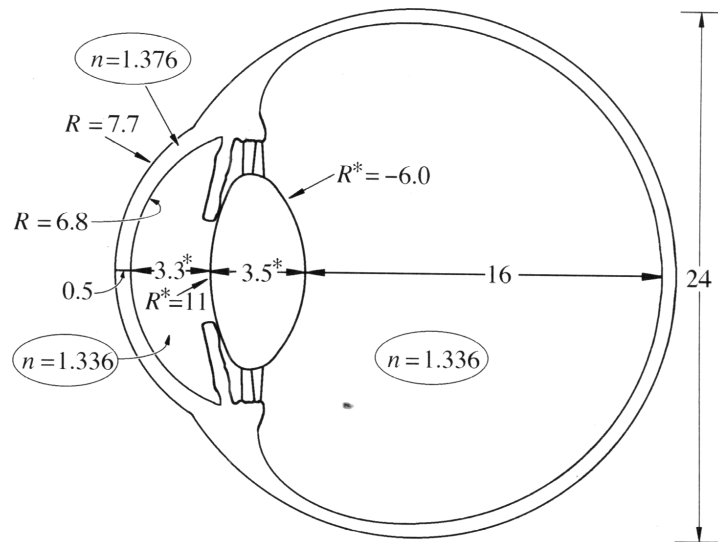


Figure 2.2: Dimensions of the human eye[Atc00]

### 2.1.1 Cornea

The cornea is the transparent anterior portion of the fibrous coat of the globe of the eye. The curvature is somewhat greater than the rest of the globe. The cornea is the first and most important refracting surface of the eye, having a power of 43 D. The anterior surface has a radius of curvature of about 7.8 mm, the posterior surface of about 6.5 mm and the central thickness is about 0.5 mm. It consists of five layers, starting from the outside: (1) the epithelium; (2) Bowman's membrane; (3) the stroma; (4) Descemet's membrane and (5) the endothelium. The cornea owes its transparency to the regular arrangement of the collagen fibres, but any factor which affects this lattice structure (e.g. swelling, pressure) results in a loss of transparency.

The anterior surface of the cornea is covered by a tear film of a total thickness of about  $10\ \mu\text{m}$ . This precorneal film is responsible for a smooth surface of the cornea by compensating rough parts of the cornea. Holes in the tear film cause great influence on the optical quality of the eye and lead to complications measuring eyes with wavefront sensors.

### 2.1.2 Crystalline lens

Although it has only two optical surfaces, the crystalline lens is the most complex optical component in the eye. It can be seen as an asymmetric deformable biconvex gradient index lens with a refractive index of about  $n=1.4$  in the center decreasing to the periphery. The crystalline lens is the part of the human optical system that is responsible for the accommodation (see fig. 2.3a). Due to increasing size and decreasing flexibility, the maximum amount of accommodation decreases with age (see fig. 2.3b).

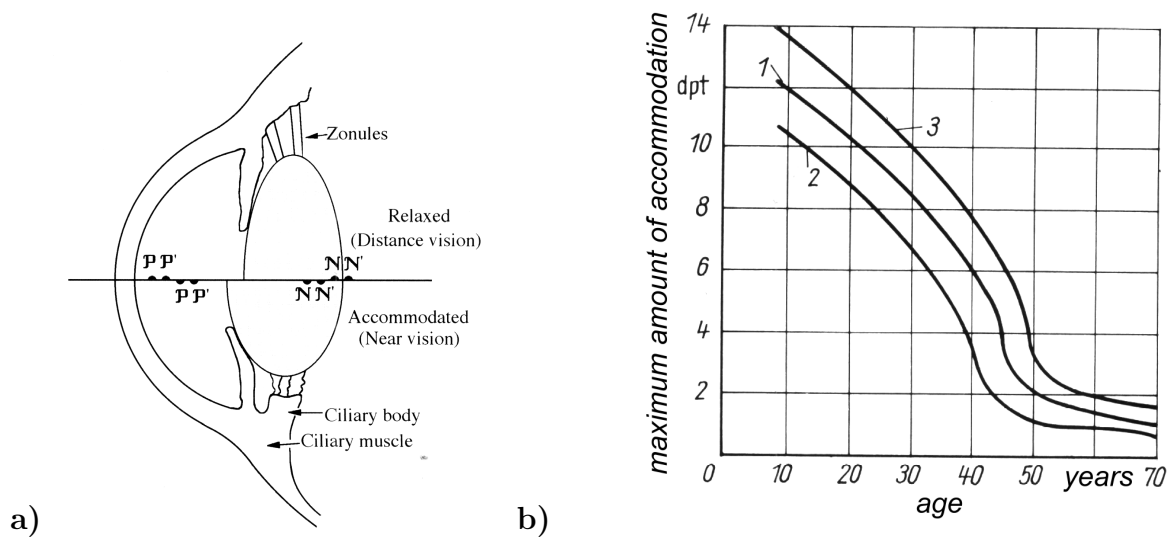


Figure 2.3: **a)** The effect of accommodation on the lens shape and lens position, and the principal and nodal points of the eye[Atc00] **b)** Maximum amount of accommodation as a function of age[Meh96]

### 2.1.3 Iris

The aperture or opening of the iris is known as pupil. Its size is determined by two antagonistic muscles, which are under autonomic control. The effect of light on the pupil diameter is shown in fig. 2.4b.

An extended pupil has several effects on the vision:

- increasing light level at the retina
- decreasing depth of focus (see fig. 2.4a)
- increasing diffraction-limited resolution
- more or less dislocated visual axis with all resulting effects

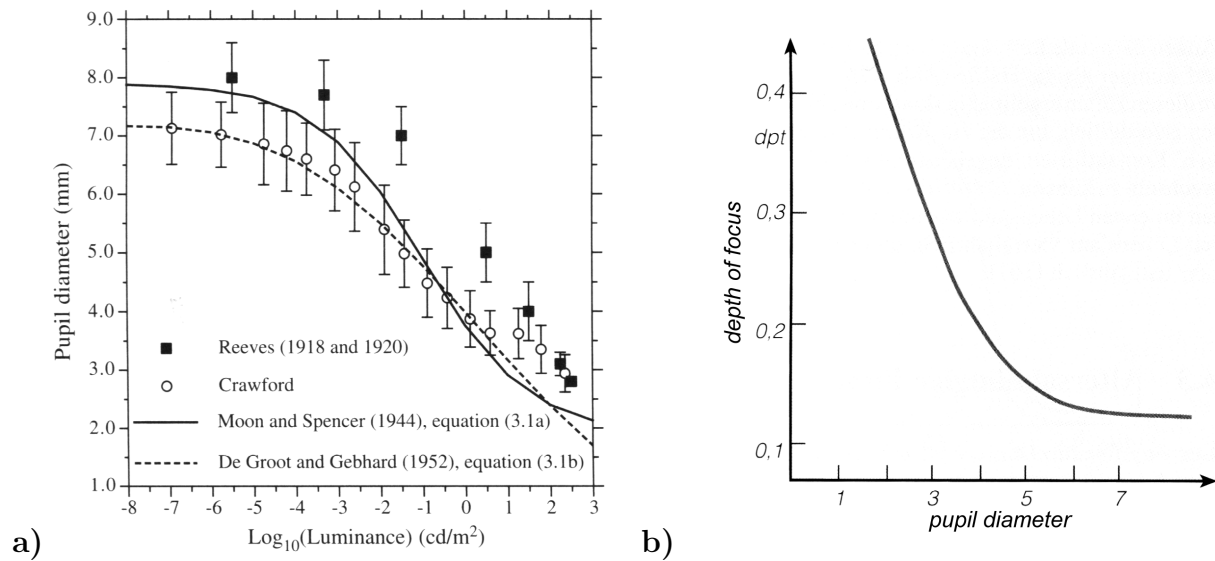


Figure 2.4: a) Pupil diameter as a function of light level[Atc00] b) Depth of focus as a function of pupil diameter[Meh96]

### 2.1.4 Retina

The light-sensitive tissue of the eye is the retina. It consists of a number of cellular and pigmented layers and a nerve fibre layer (see fig. 2.5a). The light sensitive cells are placed at the back of the retina. Light must pass through the other layers to reach these cells. There are two types of these cells, known as rods and cones. The cones predominate in the fovea, that is responsible for the highest visual acuity in the eye, and are responsible for color vision and vision at high light level (photopic vision). The rods are responsible for the vision at low light levels and are not sensible for color vision (scotopic vision). The distribution of rods and cones in the retina is shown in fig. 2.5b.

#### Stiles-Crawford Effect

Stiles and Crawford discovered, that the luminous efficiency of a beam of light entering the eye and incident on the fovea depends upon the entry point in the pupil. This effect is important to retinal image quality and is a consequence of the wave-guide properties of the photoreceptors. It is predominantly a cone phenomenon, and hence predominantly a photopic phenomenon. As a result of this effect, optical aberrations in the periphery affect the vision less than aberrations near the visual axis.

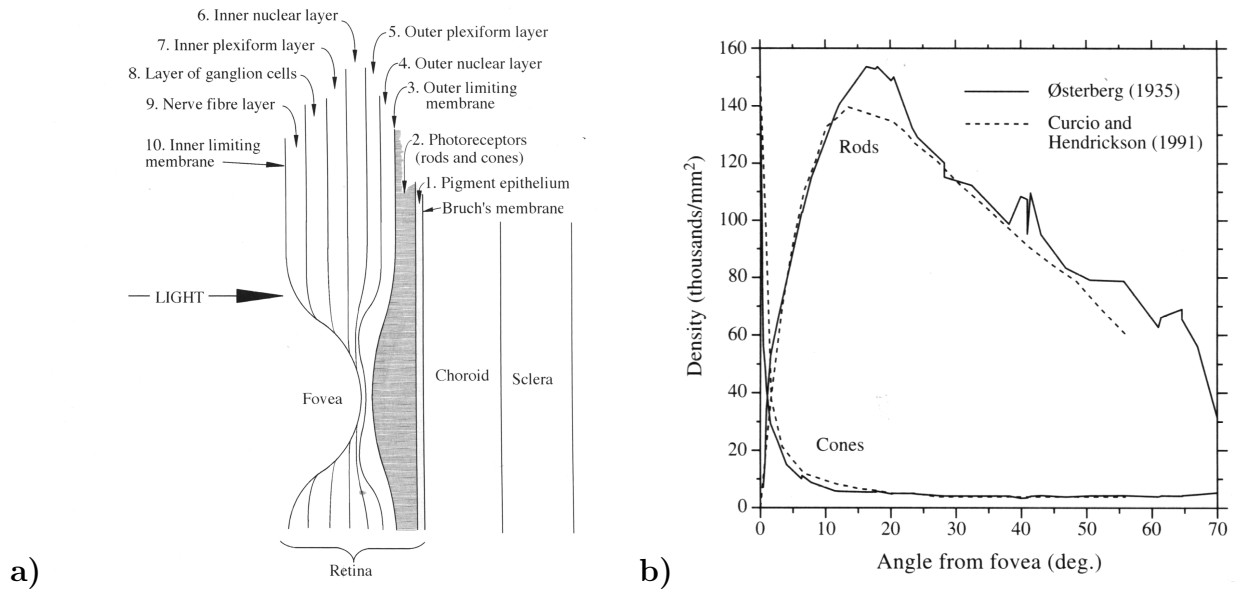


Figure 2.5: a) The layers at the back of the human eye building the retina[Atc00] b) The density of cones and rods across the retina in the temporal direction[Atc00]

## 2.2 Transmittance of the optical media

For all optical diagnostic methods in the human eye, the transmittance of the whole eye is very important. In figure 2.6 you can see that the eye is almost transparent for electromagnetic waves with a wavelength between 450 and 1200 nm. This fact makes it possible to use invisible light from the infrared spectrum for diagnostic and surgical applications in the eye.

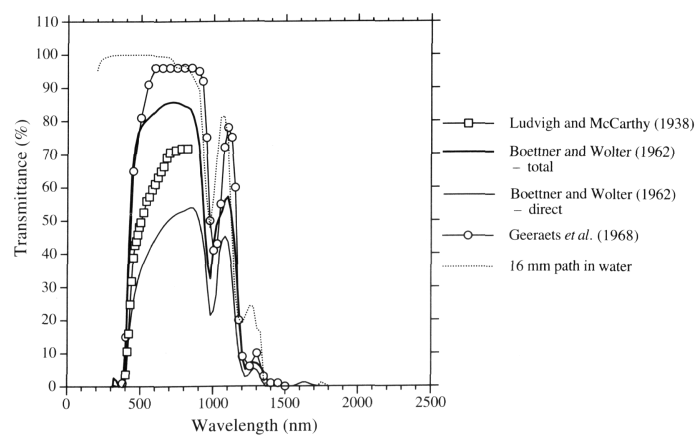


Figure 2.6: Transmittance of the human eye[Atc00]

## 2.3 Reflectance of the retina

Optical instruments like the wavefront sensor, discussed in the following chapters use the light reflected by the retina. In figure 2.7 the spectral reflectance of the fundus is shown. One can see, that light with a wavelength above 600 nm can be used for this kind of measurements.

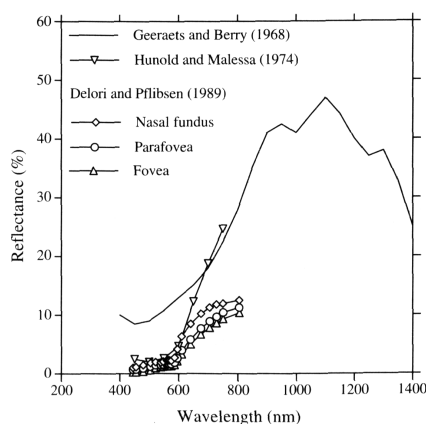


Figure 2.7: Spectral reflectance of the fundus[Atc00]

## 2.4 Main refractive errors

The refractive state of the eye which focuses distant objects on the retina while the lens is relaxed, is called emmetropia. Most of the human eyes don't match this condition. They have one or more refractive errors. The most common refractive errors are described in the following section.

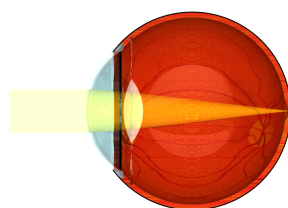


Figure 2.8: Emmetropia: In a relaxed eye distant objects are focused on the retina.



### 2.4.1 Myopia

Myopia is the refractive condition of the eye, in which the images of distant objects are focused in front of the retina, when accommodation is released (fig. 2.9a). It is also known as shortsightedness. Emmetropia can be achieved by decreasing the optical power of the optical system (fig. 2.9b).

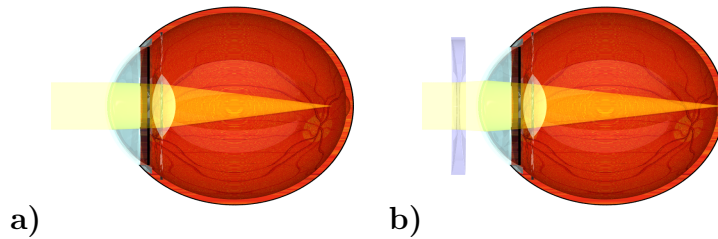


Figure 2.9: a) Myopia: In a relaxed eye distant objects are focused in front of the retina. b) Myopia corrected with a negative lens

### 2.4.2 Hyperopia

Hyperopia is the refractive condition of the eye, in which the images of distant objects are focused behind the retina, when accommodation is released (fig. 2.10a). It is also known as farsightedness. Emmetropia can be achieved by increasing the optical power of the optical system (fig. 2.10b).

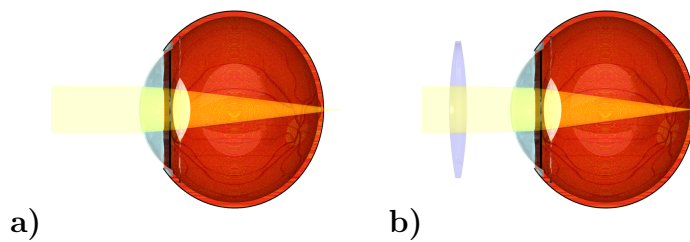


Figure 2.10: a) Hyperopia: In a relaxed eye distant objects are focused behind the retina. b) Hyperopia corrected with a positive lens.

### 2.4.3 Astigmatism

Astigmatism is the condition of refraction, in which the image of a point object is not a single point but two focal lines at different distances from the optical system. In most astigmatic eyes the refractive power of the vertical meridian (with the rule) or the horizontal meridian (against the rule) is the greatest.

### 2.4.4 Spherical Aberration

The spherical aberration is a defect of the optical system due to a variation in the focusing between peripheral and paraxial rays. The larger the pupil size, the greater the difference in focusing between two rays. When the peripheral rays are refracted more than the paraxial rays, the aberration is said to be positive or undercorrected. When the peripheral rays are refracted less than the paraxial rays, the aberration is said to be negative or overcorrected. The relaxed eye has a small amount of positive spherical aberration (up to 1 dpt for pupil of 8 mm)[Mil98].

### 2.4.5 Chromatic Aberration

Like other optical systems, the eye suffers from chromatic aberrations as well as from monochromatic aberrations. This is caused by the different focus lengths of light with different wavelength. The effect of wavelength on refraction is shown in fig. 2.11.

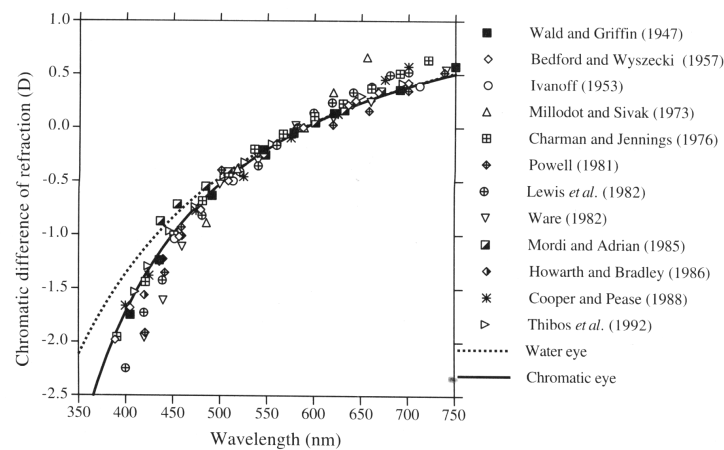


Figure 2.11: Results of experimental studies of chromatic difference of refraction as function of wavelength.[Atc00]

## 2.5 Visual Acuity

The Visual acuity is capacity for seeing distinctly the details of an object. It can be quantified as the reciprocal of the minimum angle of resolution (in minutes of arc), that can be measured using a vision chart with Landolt rings, Snellen test types or equivalent objects (see fig. 2.12).

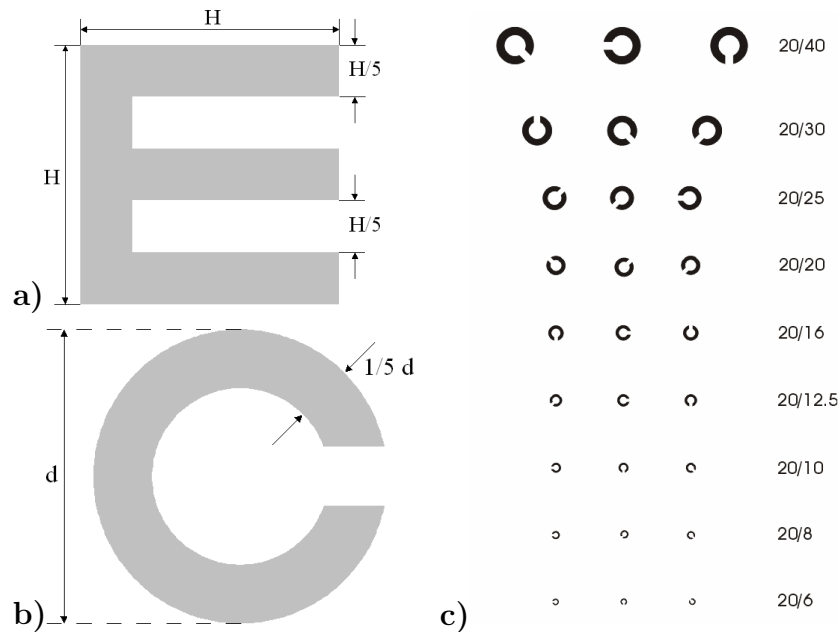


Figure 2.12: a) Snellen test types b) Landolt broken ring c) Snellen vision chart

All aberrations have an influence on the visual acuity. A relationship between uncorrected hyperopia/myopia and visual acuity is shown in fig. 2.13b and 2.13c. The influence of astigmatism on the visual acuity is shown in fig. 2.13a. You can easily see, that the effect of astigmatism on the visual acuity is approximately 50 percent of those caused by hyperopia or myopia. Another parameter that influences the visual acuity is the eccentricity (see fig. 2.13d). An eccentricity of 5 degrees corresponds to myopia and hyperopia with 1 dpt and or an astigmatism of 1.75 dpt. Finally there is an influence of the age (see fig. 2.14).

a)

Approximate relationship between uncorrected astigmatism and visual acuity		
astigmatism (D)	Snellen visual acuity	
	(m)	(ft)
4.50	6/60	20/200
3.50	6/36	20/120
2.50	6/24	20/80
1.75	6/18	20/60
1.25	6/12	20/40
0.75	6/9	20/30
0.25	6/6	20/20
0.00	6/5	20/16

b)

Approximate relationship between uncorrected absolute hypermetropia and visual acuity		
hypermetropia	Snellen visual acuity	
	(m)	(ft)
+4.5 D	6/120	20/400
+3.5 D	6/90	20/300
+2.5 D	6/60	20/200
+2.0 D	6/36	20/120
+1.5 D	6/24	20/80
+1.0 D	6/18	20/60
+0.75 D	6/12	20/40
+0.50 D	6/9	20/30

c)

Approximate relationship between uncorrected myopia and visual acuity		
myopia	Snellen visual acuity	
	(m)	(ft)
-10.0 D	6/600	20/2000
-6.00 D	6/232	20/775
-5.00 D	6/170	50/565
-4.00 D	6/126	20/420
-3.00 D	6/85	20/285
-2.50 D	6/68	20/225
-2.00 D	6/50	20/165
-1.50 D	6/33	20/110
-1.00 D	6/20	20/65
-0.50 D	6/9	20/30

d)

Average relative visual acuity in the central region of the retina			
eccentricity (degrees)	acuity (%)	Snellen fraction	
		(m)	(ft)
0	100	6/6	20/20
0.5	80	6/7.5	20/25
1	66	6/9	20/30
1.5	57	6/11	20/37
2	49	6/12	20/40
2.5	41	6/14.5	20/48
3	39	6/15	20/50
3.5	37	6/16	20/53
4	35	6/17	20/57
4.5	33	6/18	20/60
5	32	6/19	20/63
6	29	6/21	20/70
7	27	6/22	20/73

Figure 2.13: Relationship between visual acuity and a) uncorrected astigmatism b) uncorrected hyperopia c) uncorrected myopia d) eccentricity [Mil98]

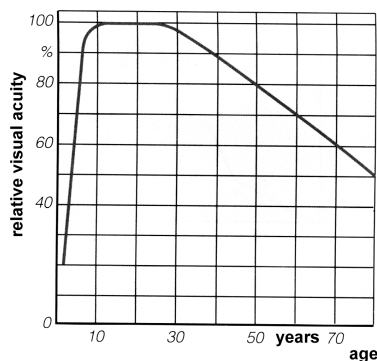


Figure 2.14: Relative visual acuity in dependence of the age [Meh96]

## 2.6 Corrections of the optical aberrations

### 2.6.1 Eye glasses

The oldest and most common possibility for a correction of the refractive errors of the human eye are eye glasses. The first glasses are designed only for a correction of nearsightedness and farsightedness and had only one refracting surface with a spherical shape. Later spectacles have two refracting surfaces, one spherical and one cylindrical surface. Up-to-date spectacles have a toric surface instead of a spherical. The newest development in the spectacles research are bifocal and multifocal glasses.

There is one important limitation to all spectacles: they are only designed for the correction of sphere and cylinder. Additionally especially when glasses with high power are used, higher aberrations are created for off-axis.

The parameters needed for the shaping of a spectacles glass are the sphere in diopters, the cylinder measured in diopters with the angle to the vertical. Additionally the distance from the glasses to the eye is needed.

### 2.6.2 Contact lenses

Another possibility of correction of refractive errors in the eye is the contact lens. They are available as hard, hard-flexible or soft lenses for daily, monthly or permanent use. Most contact lenses are only suitable to correct myopia and hyperopia. Hard lenses are also suitable to correct smaller aberrations caused by the anterior surface like astigmatism of up to 1 dpt. Modern self-stabilizing soft lenses are also able to correct higher amounts of astigmatism. Future contact lenses will be able to correct higher order aberrations. They have to be manufactured individually for every patient and require data of all aberrations of the eye. A suitable device for the required measurements is the wavefront sensor.

### 2.6.3 Refractive surgery

Permanent correction of aberrations can be achieved also by refractive surgery. Current surgical techniques are PRK (**P**hoto **R**efractive **K**eratectomy) and LASIK (**L**aser in **s**itu **K**eratomileusis). Latest clinical studies showed, that aberration-free refractive surgery is possible[Bil02]. Corrections of higher order aberrations also require wavefront data.

# Chapter 3

## Principles of wavefront sensors

### 3.1 Hartmann test

A simple method used in wavefront diagnostics is the Hartmann test. It consists of two parts. The first part is a plate with a hole pattern, placed in the plane where the wavefront should be sensed. Behind the plate the wavefront is divided in a number of small parts. Every part of the wavefront could be seen as a single approximately plain wavefront with a homogeneous direction of propagation.

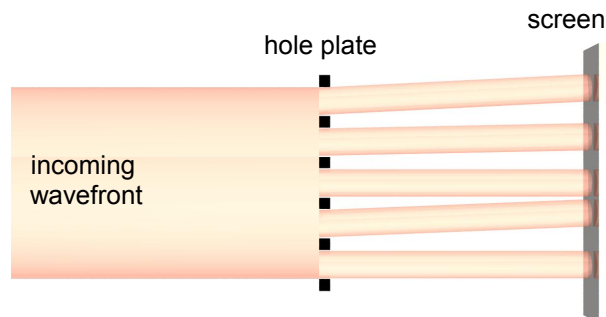


Figure 3.1: 2-dimensional Hartmann test

In a distance  $D$  behind the hole plate a plain screen is placed. For automatic wavefront analysis, a camera chip can be used as screen.

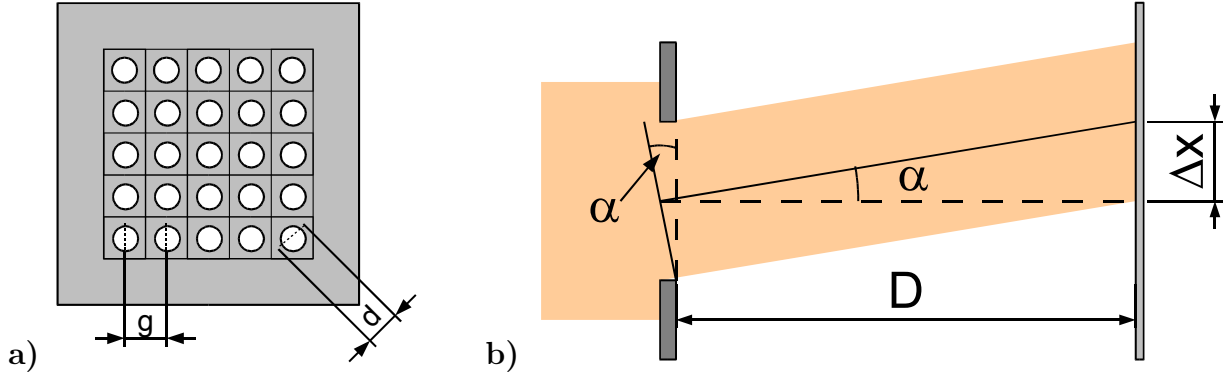


Figure 3.2: a) The Hartmann screen front view b) Geometric properties of one subaperture

The shift  $\Delta x$  of the center of the light spot on the screen is proportional to the local tilt of the wavefront  $W$  at the hole plate.

$$\alpha_x \approx \tan(\alpha_x) = \frac{dW(x, y)}{dx} = \frac{\Delta x}{D}; \quad \alpha_y \approx \tan(\alpha_y) = \frac{dW(x, y)}{dy} = \frac{\Delta y}{D} \quad (3.1)$$

Two neighboring spots on the screen overlap, if the lateral shift of one point equals:

$$\Delta x_{\max} = g - d \quad (3.2)$$

This corresponds to an maximum angle  $\alpha$  of:

$$\alpha_{\max} \approx \tan\left(\frac{g - d}{D}\right) \quad (3.3)$$

The principle used in this kind of sensor has several limitations:

- A big fraction of the light is blocked by the hole plate.
- The intensity within the spots is at the most just as high as within the original wavefront.
- Small shift of the spots may cause overlapping.
- No information can be obtained about the wavefront at the blocked areas.

## 3.2 Hartmann-Shack wavefront sensor

The Hartmann-Shack wavefront sensor uses a principle similar to the Hartmann test [Sha71]. The only difference is a 2-dimensional array of lenses that replaces the hole plate. Instead of the variable distance  $D$ , the distance between lens array and screen has to be equal to the focal length of the lenses in the array.

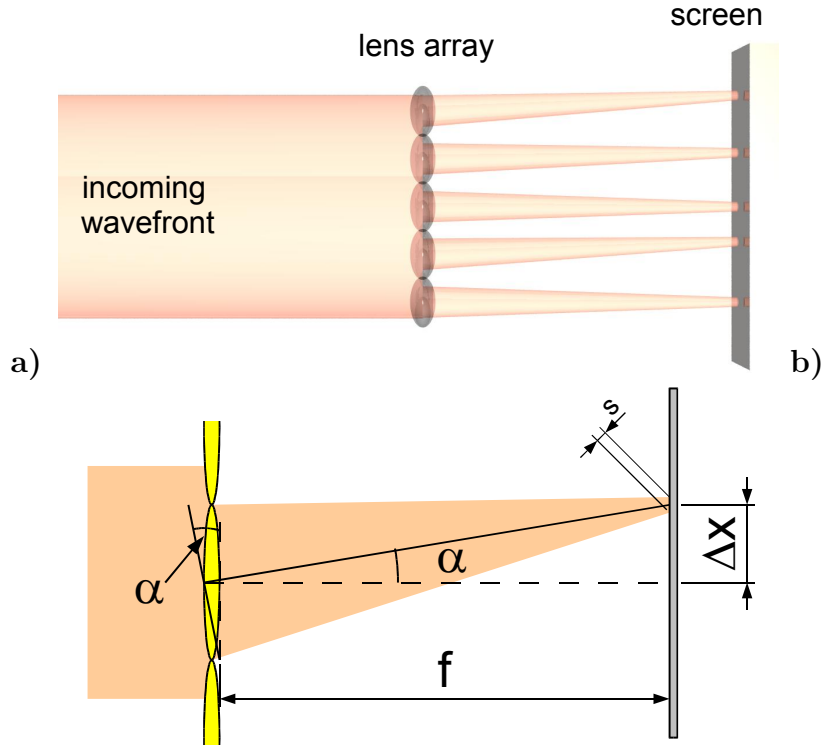


Figure 3.3: a) 2-dimensional Hartmann-Shack wavefront sensor (HSS) b) Geometric properties of one subaperture

For the lateral shift of the focus spots exists a similar equation:

$$\alpha_x \approx \tan(\alpha_x) \frac{dW(x, y)}{dx} = \frac{\Delta x}{f}; \quad \alpha_y \approx \tan(\alpha_y) \frac{dW(x, y)}{dy} = \frac{\Delta y}{f} \quad (3.4)$$

Since the size of the focus spots  $s$  can be much smaller than the size  $d$  of the holes of the Hartmann hole plate, overlapping is less probable.



### 3.3 Extensions of the HSS

If it is not possible to place the lens array in the plane where the wavefront should be detected, a telescope is necessary (see fig. 3.4). The detection plane and the sensor plane are conjugated to each other.

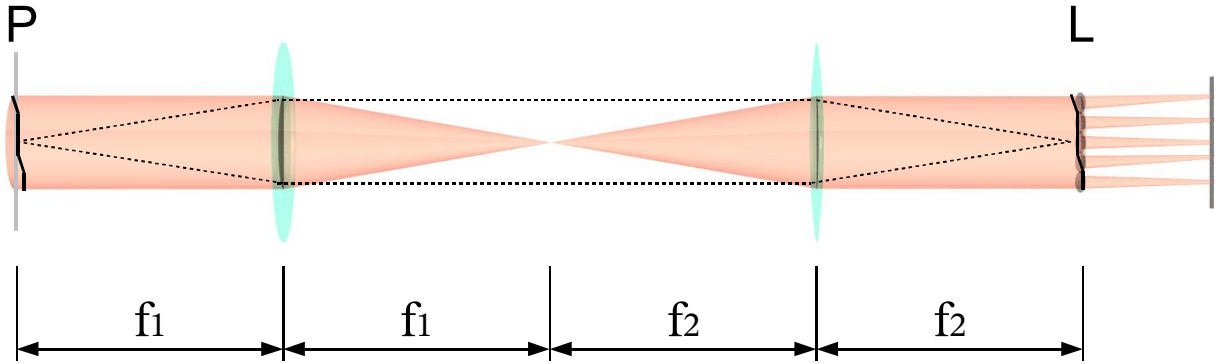


Figure 3.4: HSS with a telescope. For equal values of the focal lengths  $f_1$  and  $f_2$ , the wavefront at the position of the plane **P** is equal to the wavefront at the lens array **L**.

If lenses with different focal lengths are used, the telescope is suitable to magnify the wavefront in lateral direction. A point  $A_P(x_P, y_P)$  in the plane **P** is imaged to  $A_L(x_L, y_L)$  in the plane of the lens array **L** with:

$$x_L = -x_P \cdot \frac{f_2}{f_1}; \quad y_L = -y_P \cdot \frac{f_2}{f_1} \quad (3.5)$$

The gradient  $(dW(x_P, y_P)/dx_P, dW(x_P, y_P)/dy_P)$  at **P** corresponds to an gradient  $(dW(x_L, y_L)/dx_L, dW(x_L, y_L)/dy_L)$  at **L** with:

$$\frac{dW(x_L, y_L)}{dx_L} = -\frac{f_1}{f_2} \frac{dW(x_P, y_P)}{dx_P}; \quad \frac{dW(x_L, y_L)}{dy_L} = -\frac{f_1}{f_2} \frac{dW(x_P, y_P)}{dy_P} \quad (3.6)$$

The optical path difference is not affected by the telescope since the product of lateral magnification and magnification of the gradient is independent of the ratio between  $f_1$  and  $f_2$ .

If more than one telescope is put in the optical path, the resulting magnification is the product of all single magnifications. The planes between the telescopes are again conjugated to the sensor plane and the detection plane.

### 3.3.1 General compensation of aberrations

The dynamic range of HSS is limited by its focal length and sub-lens diameters. The sensitivity of the wavefront sensor for small aberrations limits the maximum measurable aberrations. A common case is a wavefront with high values of sphere or astigmatism and small additional higher order aberrations. A solution for this kind of wavefronts is a defined precompensation of sphere and astigmatism.

A general approach for compensation of any aberration is to put a correcting element between two telescopes in a plane  $P_1$  that is conjugated to the sensor plane and to the detection plane (see fig. 3.5). The correcting element at  $P_1$  can be any kind of thin lens.

The positions of the wavefront at the sensor plane L corresponds to the following position at the detecting plane P:

$$x_L = x_P \cdot \frac{f_2 f_4}{f_1 f_3}; \quad y_L = y \cdot \frac{f_2 f_4}{f_1 f_3} \quad (3.7)$$

and to the position at the compensation plane  $P_1$ :

$$x_L = -x_P \cdot \frac{f_4}{f_3}; \quad y_L = -y \cdot \frac{f_4}{f_3} \quad (3.8)$$

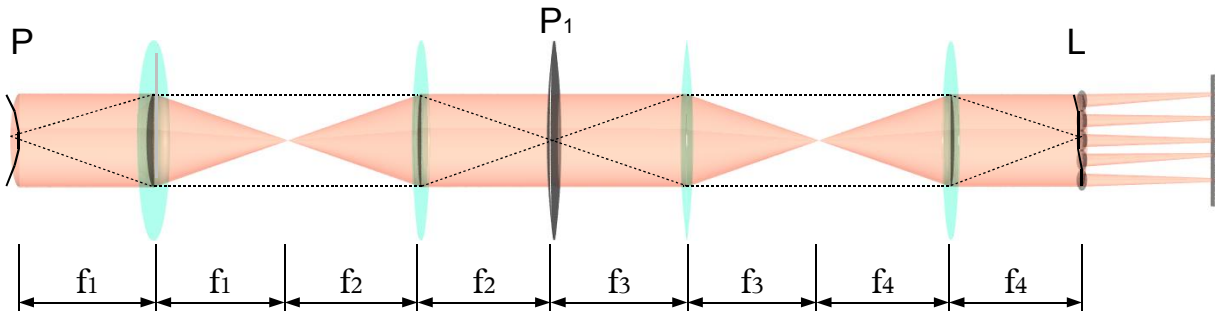


Figure 3.5: General compensation of aberrations. The phase plate  $P_1$  directly affects the wavefront at the sensor L.

With this optical setup, it is possible to compensate any amount of sphere by putting a positive or negative lens into the beam at position  $P_1$ . If two 1:1-telescopes are used, a wavefront with a positive/negative sphere can be compensated by a negative/positive lens with the same amount at the position  $P_1$ . If the sphere is the only aberration, the result will be plain wave at the sensor plane L.

Similar results can be achieved with a compensation of astigmatism. A cylinder lens has not only an astigmatic component but also a sphere component. Therefore compensation of pure astigmatism requires at least two elements: a cylinder lens and a spherical lens or two cylinder lenses.

### 3.3.2 Sphere compensation

A more flexible setup for a compensation of sphere is to modify the distance between the two lenses of a telescope (see fig. 3.6). The effective power  $1/g$  of a telescope extended by a  $d$  can be calculated with the lens equation:

$$\frac{1}{f_1} = \frac{1}{f_1 + d} + \frac{1}{f_1 - g} \quad (3.9)$$

The solution for the effective power is:

$$\frac{1}{g} = \frac{d}{f_1^2} \quad (3.10)$$

If the focal length  $f_1$  is 50 mm, for example, the effective power  $D$  is:

$$D = \frac{1}{g} = \frac{d}{(50 \text{ mm})^2} = \frac{d}{2.5 \text{ mm}} \text{ dpt} \quad (3.11)$$

With this result, you can say that every 2.5 mm translation corresponds to a compensation of 1 diopter.

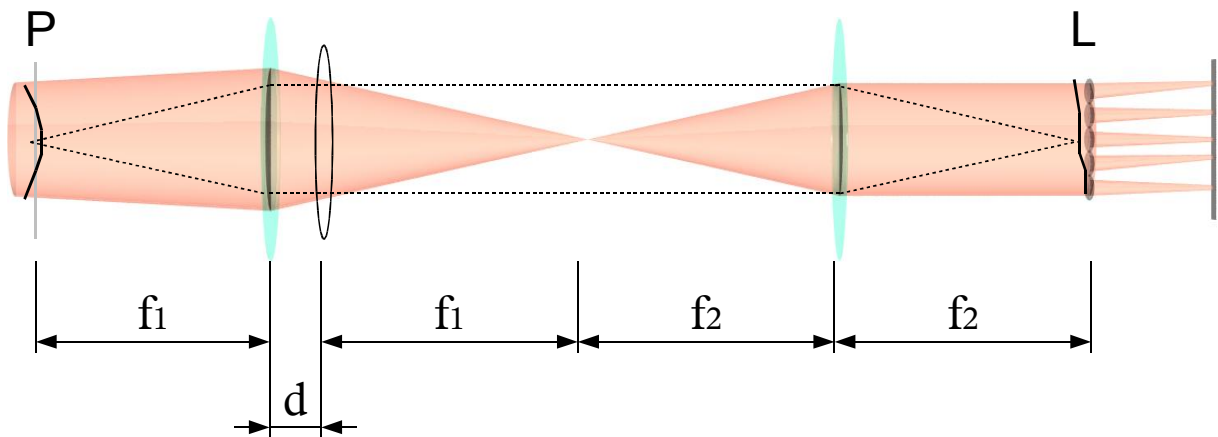


Figure 3.6: A telescope used for correction of sphere.

### 3.3.3 Cylinder compensation

Although it is possible to put a cylinder lens with the desired power and axis between two telescopes as shown in fig. 3.5, a more flexible solution is preferred. Instead of a single cylinder lens, a pair of two cylinder lenses with the same amount of power ( $P_{1,2}$ ) but opposite sign can be used.

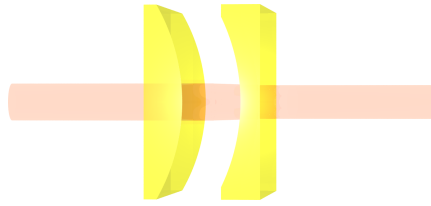


Figure 3.7: Two rotating cylinder lenses suitable to compensate astigmatism with any power and any axis.

If the angle between the axes of the two cylinder lenses is zero, the resulting effective cylinder has 0 dpt. A rotation of the two axes against each other cause an effective cylinder of up to twice the power of one cylinder lens at the 90°-position. If the rotation angle of the first, positive lens is  $\alpha_1$  and the rotation angle of the other cylinder lens is  $\alpha_2$ , the resulting astigmatism has the power:

$$P_{\text{effective}} = 2 \cdot P_{1,2} \cdot |\sin(\alpha_1 - \alpha_2)| \quad (3.12)$$

The angle of the resulting astigmatism is:

$$\alpha_{\text{effective}} = \frac{\alpha_1 + \alpha_2}{4} - 45^\circ \quad (3.13)$$

Higher order aberrations caused by this setup are very small for distances between the two cylinder lenses that are small in comparison with their focal lengths.

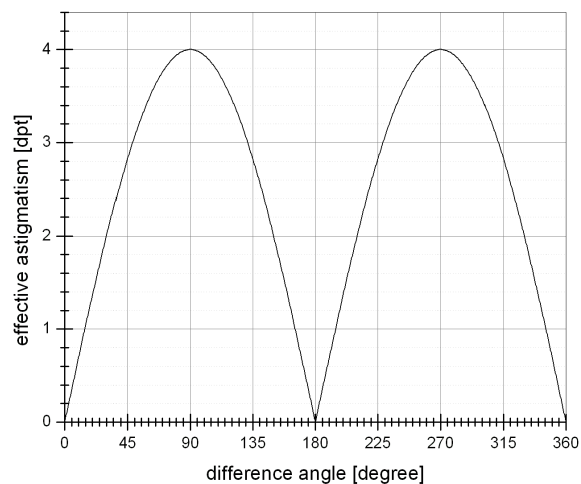


Figure 3.8: Effective astigmatism as result of two rotated cylinder lenses with focal lengths of 500 mm and -500 mm.

# Chapter 4

## Optical setup of the devices

For the tests of the algorithms and applications at human eyes two complete systems have been build. The first system is a small device with sphere compensation that is suitable for clinical application. The second system has been built for experimental purposes. It has a build-in compensation of sphere and cylinder, and is based mainly on LINOS Microbench. Three additional copies of the first system have been built in cooperation with Philips to do extended clinical studies. Experiences with these systems have been used to improve the reliability of the algorithms especially with problematic eyes.

In the first part of this chapter, the basic components of the devices are described. The extensions, that are part of both systems, are topic of the following section. The chapter concludes with descriptions of the two systems with their individual extensions.

### 4.1 Basic components of the wavefront sensors

The basic setup for all systems is shown in fig. 4.1. The necessary components are the wavefront sensor, consisting of a lens array and a camera chip, the light source, a beam splitter and a telescope consisting of two lenses.

For applications at the human eye the wavefront sensor has to fulfill several conditions:

- The lateral extension of the wavefront sensor should match to the size of the wavefront limited by the pupil of the eye (diameter about 2-7 mm).
- The number of rows and columns of sublenses used for the measurements should allow the determination of higher order aberrations. In combination with the previous condition the size of the sublens is limited to values smaller than  $400\ \mu\text{m}$  to have at least 5 rows and columns usable for the reconstruction of the wavefront.
- A light source should have a wavelength that will be transmitted by the optical media of the eye and that will be reflected by the retina. Furthermore, the spectral

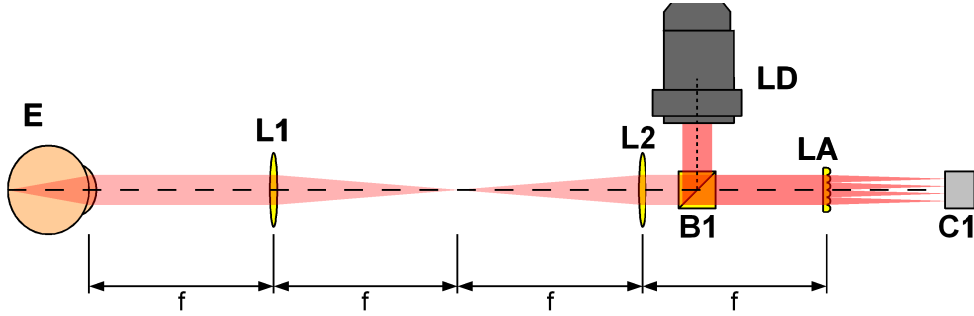


Figure 4.1: Basic components for measurements with a HSS at the human eye. The beam of the light source **LD** is reflected by a beam splitter into the optical axis of the system. The parallel beam is focused on the retina by the eye **E**. The two lenses **L1** and **L2** are necessary for a lens array **LA** that is conjugated to the pupil plane of the eye. The camera **C1** detects the HSS spot pattern.

sensitivity of the retina for this wavelength should be low to avoid blending of the patient.

- The light intensity should be less than the maximum intensity allowed for long-time exposure of the human eye to an collimated beam.

### 4.1.1 Lens array

The properties of the lens array determine the sensitivity, the dynamic range and the lateral resolution of the HSS. The first parameter is the distance between the sub lenses that should be equal to their diameter. A sub lens diameter of 300-400  $\mu\text{m}$  allows to use about 15-20 rows and columns of the lens array with a 6 mm pupil. The smallest standard lens arrays available have a total diameter of 0.5" or 1", so they cover more than the 7 mm of the maximum wavefront's lateral extension. The focal length is responsible for the dynamic range of the sensor. Values between 30-50 mm are a good compromise between higher sensitivity and larger dynamic range. The parameters of the lens arrays used in the systems are shown in table 4.1.

No.	sub lens diameter	focal length
1	400 $\mu\text{m}$	53 mm
2	312.5 $\mu\text{m}$	34 mm
3	300 $\mu\text{m}$	30 mm

Table 4.1: Main parameters of the lens arrays used for the experiments

### 4.1.2 Light source

For best results a collimated monochromatic light source is required. The best solution is a diode laser, that is small, adjustable and that emits light with the described qualities. The next question is the choice of a wavelength. Light with a wavelength in the near infrared is transmitted by the optical medias of the eye and reflected by the retina and doesn't blend the patient. A wavelength of 780 nm is a common wavelength for diode lasers and is almost invisible because of the low spectral sensitivity of the eye (see chapter 2).

### 4.1.3 Camera

The camera is responsible for the image acquisition. Since most standard ccd cameras are still sensitive for light with this wavelength, a special infrared camera is not required. Cameras with standard ccir video output have a sufficient resolution of  $768 \times 576$  pixels. Devices with higher resolutions and smaller pixel dimensions are less sensitive and require special expensive image acquisition hardware. A critical parameter is the frame rate of standard cameras: A maximum number of 25 frames (50 half frames) can be taken in one second. Fast eye movements like micro saccades require much more frames per second, but for most situations the standard 25 frames are sufficient. The size of a camera with  $2/3''$ -chip ( $8.8 \text{ mm} \times 6.6 \text{ mm}$ ) perfectly fits to size of the pupil-limited wavefront.

## 4.2 Extensions of the wavefront sensors

### 4.2.1 Laser monitoring

Although the laser diode has an internal system for power monitoring, an additional external system is required for security reasons. The light intensity at the eye should not exceed a power of  $50 \mu\text{W}$ . If the laser output increases or decreases, the power is automatically turned off and requires a manual reset for restart.

### 4.2.2 Polarization elements

Some components used in the systems concern the polarization, that is required for the suppression of reflection. Although all optical surfaces have an anti-reflex coating, reflections are still present. Since only a small part of the incoming light is reflected by the eye, some reflection of surfaces in the system have a similar intensity. All reflections can be reduced using polarized light. The laser diode emits light that is almost linear polarized. The polarizing beam splitter B2 only reflects linear polarized light. All the light reflected by the surfaces between this beam splitter and the quarter wave plate in front of the eye have the same polarization. The polarizing beam splitters B2 and B3 reflect this light and

insure, that it doesn't reaches the camera C1. Light that passes the quarter wave plate is circular polarized and linear polarized orthogonal to the incoming light after the second pass. This light is transmitted by B2 and B3 and can be detected by the camera C1. The quarter wave plate is tilted to avoid reflections from its left surface.

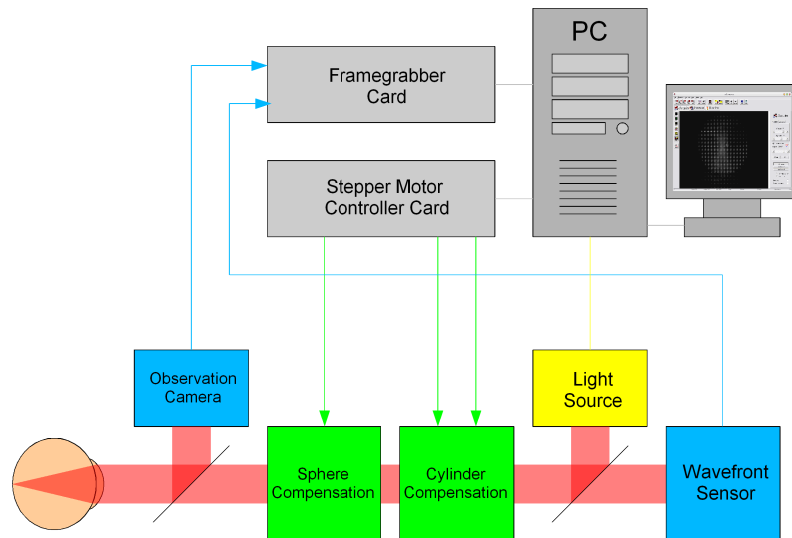


Figure 4.2: Complete schematic setup of the whole systems including mechanical components and data processing. The observation system is not present in the first system, the cylinder compensation is not present in the second system.

## 4.3 Optical setup of System 1

In the first system, the following extensions are implemented: the laser monitoring, the polarizing elements, a pinhole for spacial filtering, a sphere compensation and a pupil observation system (see fig. 4.4).

### 4.3.1 Pinhole

The pinhole PH removes most of the reflections from the cornea. An additional effect of the pinhole is that wavefronts with more than 0.75 dpt are blocked. This is not a problem because most of the sphere can be removed by the sphere compensation system.

### 4.3.2 Pupil observation system

Reproducible measurements at the human eye require a precise lateral and axial fixation of the pupil. Lateral translations of the eye cause lateral translations of the HSS pattern



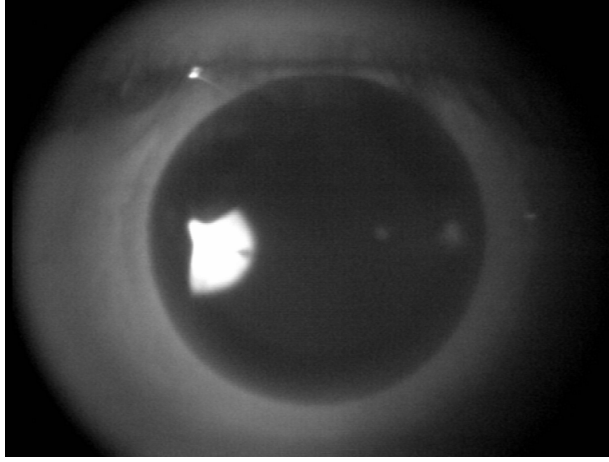


Figure 4.3: Picture taken with the observation camera

on the camera chip with the same amount. Since the camera chip has a size of  $6.6 \times 8.8$  mm it is necessary that a 6 mm-pupil has to be aligned with an accuracy of better than 0.6 mm to avoid loss of information. The focus plane of the lens L1 is conjugated to the plane of the wavefront sensor. Since L1 and L2 have an identical focal length, these wavefronts are identical. Axial translations away from these positions make it extremely difficult to determine the shape of the wavefront at the eye.

For these two issues an additional observation camera (see green beam in fig. 4.4) is implemented in the system. A picture taken with this camera is shown in fig. 4.3. The device is aligned, if the pupil is centered and the iris of the eye is sharp recognizable. Due to a small depth of focus of the observation camera system, axial translation smaller than 1 mm can be observed. The whole system can be moved in all directions by an operator using the joystick (see fig. 4.5a).

### 4.3.3 Sphere compensation

The sphere compensation is implemented as it is described in the previous chapter. The right part of the system showed in fig. 4.4 is movable by an motorized translation stage. It seems, that it could be easier to move the left part. Since a defined distance between the eye and the lens L1 is required, the patient would have to be moved too. The compensation  $D$  can be calculated using the focal length of 50 mm:

$$D = \frac{d}{(50 \text{ mm})^2} = \frac{d}{2.5 \text{ mm}} \text{ dpt} \quad (4.1)$$

The range is limited by the available space. A maximum translation range of 36.25 mm corresponds to a difference of 14.5 dpt that is used to compensate spheres with a power of  $-11.25$  dpt to  $+3.15$  dpt.

### 4.3.4 Optical setup

The optical setup of system 1 is shown in fig. 4.4. The whole device is put in a compact box and mounted movable on a chin rest (see fig. 4.5).

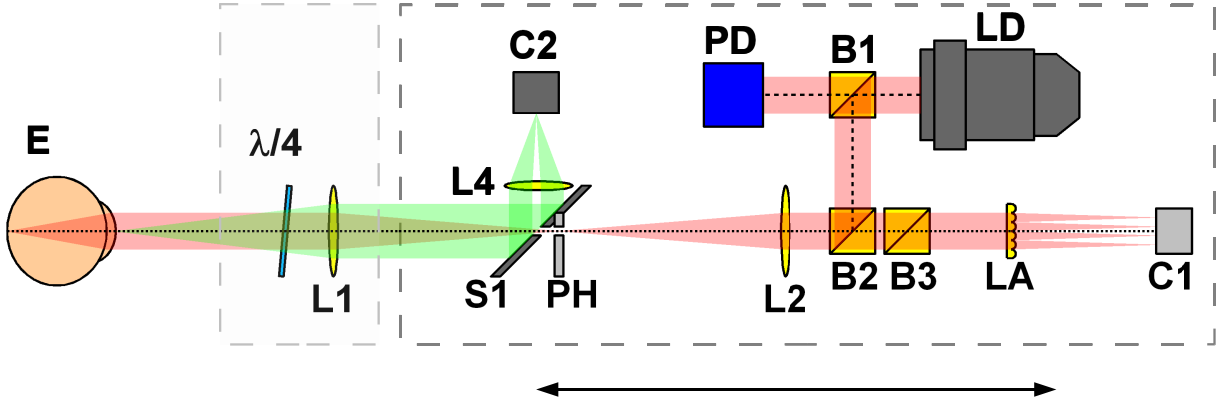


Figure 4.4: Optical setup of HSS system with sphere compensation. The light emitted by the laser diode **LD** is split by the polarizing beam splitter cube **B1**, that improves the polarization of the beam and that enables the photodiode **PD** to monitor the laser output. The second beam splitter cube **B2** reflects the laser beam into the optical axis of the system. The two 50 mm-achromats **L1** and **L2** build the telescope, that is responsible for the conjugation of the pupil plane with the sensor plane. The quarter wave plate  $\lambda/4$  converts the polarized light to circular polarized light. The eye **E** focusses the light on the retina where it is reflected. The reflected light is linear polarized after the second pass of the quarter wave plate  $\lambda/4$ . The pinhole **PH** filters reflections caused by the cornea. The polarizing beam splitter cubes **B2** and **B3** filter all reflections that haven't passed the quarter wave plate  $\lambda/4$ . The lens array **LA** and the camera **C1** form the wavefront sensor. The cmos camera **C2**, the 20 mm lens and the mirror **S1** are components of the pupil observation system. The right part of the system can be translated against the left part with a motorized translation stage.

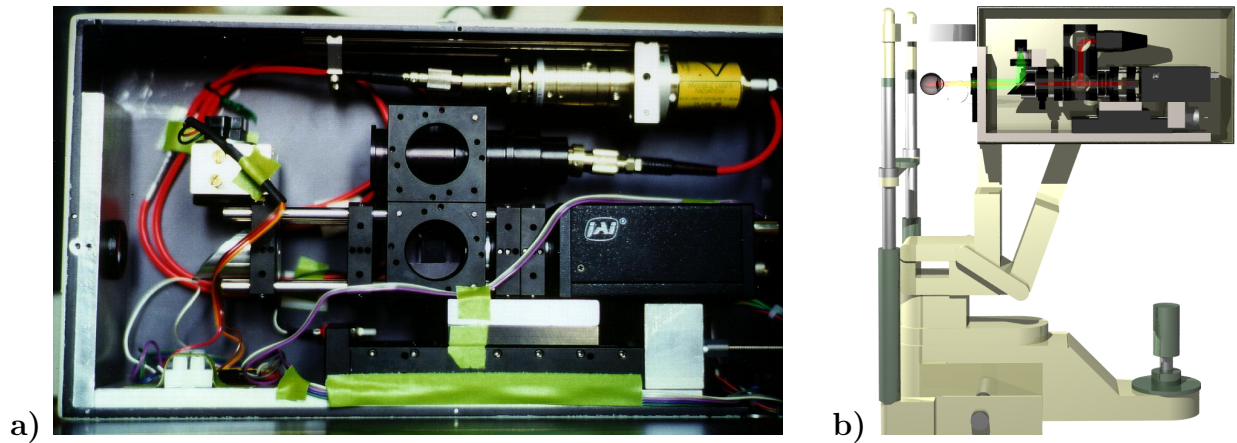


Figure 4.5: a) Photography of system 1 b) system 1 mounted on a chin rest

## 4.4 Optical setup of System 2

In the second system, the following extensions are implemented: the laser monitoring, the polarizing elements, a compact sphere compensation (fig. 4.6) and a cylinder compensation (see fig. 4.8).

### 4.4.1 Sphere compensation

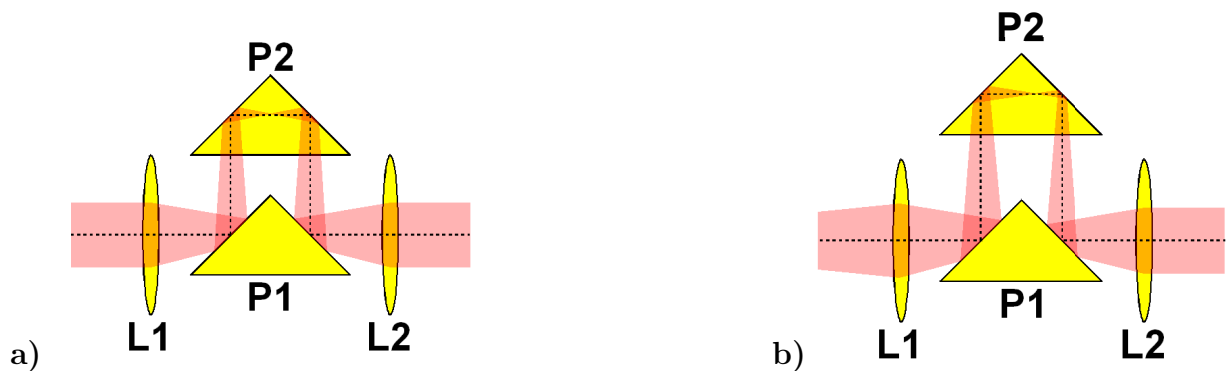


Figure 4.6: Sphere compensation module a) in home position b) in compensation position

The sphere compensation in system 2 is little different to the previous one. Instead of moving almost the whole system, only a prism is moved (see fig. 4.6). Every millimeter of translation  $d$  of the prism P2 causes a change of the telescope length of 2 millimeters.

With the 50 mm-lens L1 the resulting compensation  $D$  is:

$$D = 2, \frac{d}{(50 \text{ mm})^2} = \frac{d}{1.25 \text{ mm}} \text{ dpt} \quad (4.2)$$

#### 4.4.2 Cylinder compensation

The cylinder compensation used in system 2 is realized as mentioned in the previous chapter. Since the two telescopes have no magnification, the compensation at the eye, at the lens array and at the cylinder lenses are equal. The cylinder lenses have focal lengths  $f_{c1}, f_{c2}$  of +500 mm and -500 mm. The maximum astigmatism compensation  $D_a$  is:

$$D_a = 1 \frac{1}{f_{c1}} - \frac{1}{f_{c2}} = \frac{1}{500 \text{ mm}} + \frac{1}{500 \text{ mm}} = 4 \text{ dpt}. \quad (4.3)$$

The two lenses are individually mounted in motorized rotation stages. It is possible to rotate every cylinder lens with  $720^\circ/s$  with a precision of better than  $0.1^\circ$ . The required rotation for both cylinder lenses to change the compensation from 0 to 0.5 dpt is:

$$\alpha_1 = -\alpha_2 = \arcsin\left(\frac{0.5 \text{ dpt}}{4 \text{ dpt}}\right) 45^\circ = 5.61^\circ \quad (4.4)$$

A rotation of  $5.61^\circ$  of both cylinders takes less than 10 ms. The mechanical realization of the cylinder compensation is shown in fig. 4.7.

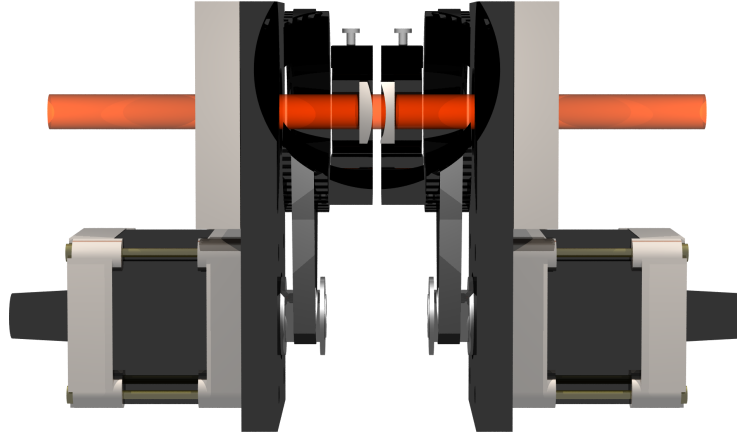


Figure 4.7: Cylinder compensation module

### 4.4.3 Optical setup

The optical setup of system 2 is shown in fig. 4.8. A picture of the mechanical setup is shown in fig. 4.9

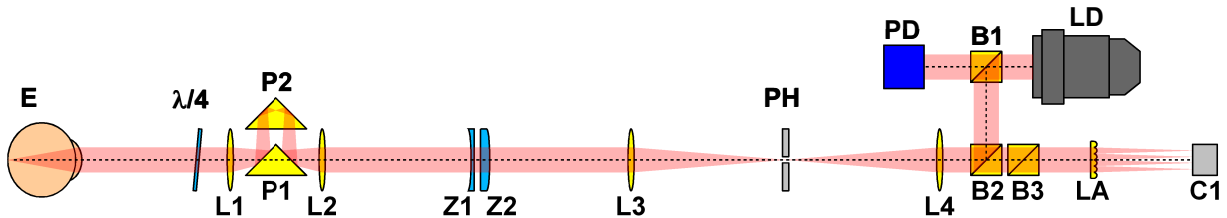


Figure 4.8: Optical setup of HSS system 2 with compensation of sphere and astigmatism. The light emitted by the laser diode **LD** is split by the polarizing beam splitter cube **B1**, that improves the polarization of the beam and that enables the photodiode **PD** to monitor the laser output. The second beam splitter cube **B2** reflects the laser beam into the optical axis of the system. The four 50 mm achromats **L1**, **L2**, **L3** and **L4** build two telescopes, that are responsible for the conjugation of the pupil plane with the sensor plane. The two cylinder lenses **Z1** and **Z2** with focal lengths of 500 mm and -500 mm are individual motorized 360° rotatable and build the astigmatism compensation system. The prism **P1** and movable prism **P2** build the sphere compensation system. The quarter wave plate  $\lambda/4$  converts the polarized light to circular polarized light. The eye **E** focusses the light on the retina where it is reflected. The reflected light is linear polarized after the second pass of the quarter wave plate  $\lambda/4$ . The pinhole **PH** filters reflections caused by the cornea. The polarizing beam splitter cubes **B2** and **B3** filter all reflections that haven't passed the quarter wave plate  $\lambda/4$ . The lens array **LA** and the camera **C1** form the wavefront sensor. The cmos camera **C2**, the 20 mm lens and the mirror **S1** are components of the pupil observation system.

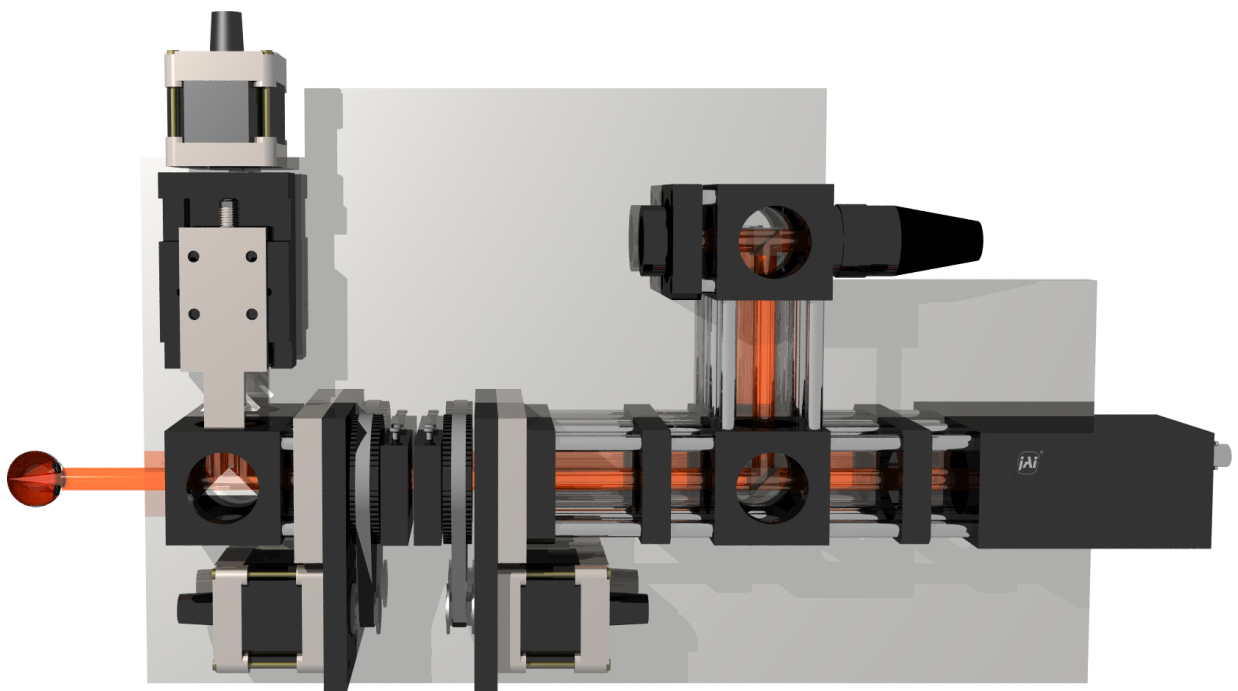


Figure 4.9: Mechanical setup of system 2

# Chapter 5

## Algorithms for the use with wavefront sensors

The topic of this chapter is the whole process starting from the data delivered by the framegrabber and ending with the presentation of the wavefront and refraction data. This process can be divided in several parts. The first part is the image processing with the image preprocessing and the spot finding algorithm. After a successful spot finding process the acquired data of the spot positions can be used for modal or zonal estimation of the wavefront. With this wavefront data numerous interesting parameters like the sphere, astigmatism or spherical aberration can be calculated easily.

### 5.1 Image preprocessing

The first task of the image processing is the analysis of the image quality. For best results in the following steps, it is necessary that the available 8 bits of the framegrabber are used optimally. The most problems can be recognized easily using the raw data.

A great number of pixels having the maximum available gray level (255) is a clear sign that the framegrabber achieved a level of *saturation*. This causes a loss of information for the following spot finding process because the pixels in the center of the spots with saturation won't help increasing the precision on the spot position. An example a spot pattern with obvious saturation is shown in fig. 5.1. There are three solutions to solve this problem for the next images that will be taken. The first possibility is to increase the white level of the framegrabber. This can be easily done using the software interface of the framegrabber. The next solution is to decrease the sensitivity of the ccd camera. This can also be done automatically by the software if the camera has a suitable interface to the computer. The last possibility is to decrease the laser power. Since the applicable laser light level used for diagnostics at the human eye is already extremely low, adjustments of the laser power in not useful in this case.

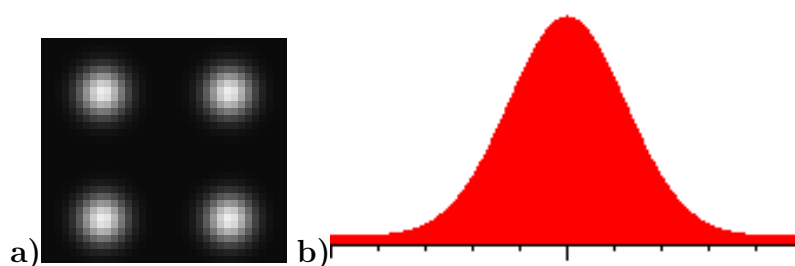


Figure 5.1: A spot pattern with perfect adjustment of framegrabber, camera sensitivity and laser power. The dynamic range is used optimally. **a)** part of spot pattern **b)** 2-d-plot of gray values

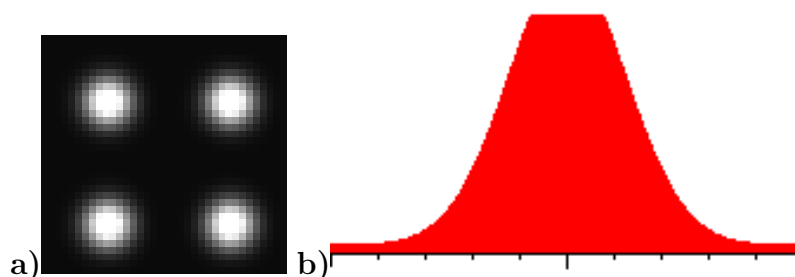


Figure 5.2: Part of a spot pattern with the framegrabber reaching a level of saturation **a)** Part of spot pattern **b)** 2-d-plot of gray values

The opposite problem is *low intensity* which means that the maximum gray level in the image is by far less than the maximum gray level available, which also causes less precision in the whole data. A solution can be found similar to the problem with the saturation (see fig. 5.2).

The third problem is a high minimum gray level, that is a obvious sign for a *high underground* level (see fig. 5.3 ). It can be caused by a low black level of the framegrabber or a high camera sensitivity. An adjustment of the framegrabber by the software is the preferred solution also for this problem but camera adjustment is also possible. If a high underground gray level is present, the spot finding algorithm will take much more time and it is possible that some spots can't be recognized correctly.

If most of the pixels in the image have a gray level of zero (*black*), parts of spots or whole spot could be missing (see fig. 5.4). The solution is a decreasing of the framegrabber black level or the increasing of the camera sensitivity.

These four problems mainly concerning the framegrabber sensitivity are summarized in table 5.1 with its identifying parameters.

Completely different to the previous four cases is a spot pattern like that in fig. 5.5. It shows saturation of the camera. It can easily recognized by numerous pixels with very



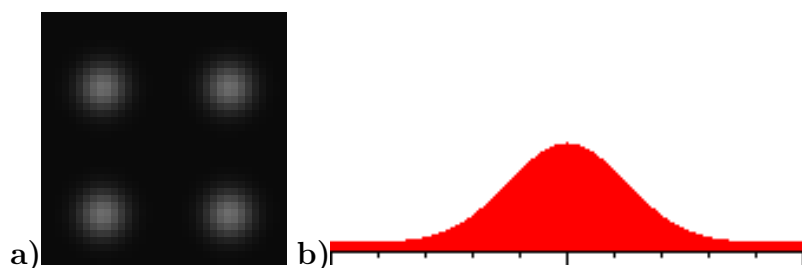


Figure 5.3: Part of a spot pattern with with low intensity. Only the lower range of the dynamic range of the framegrabber is used. Precision is lost **a)**Part of spot pattern **b)**2-d-plot of gray values

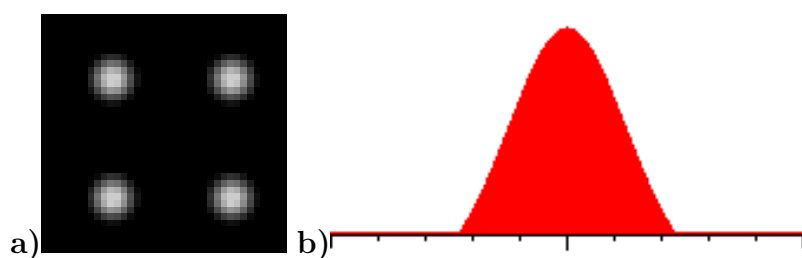


Figure 5.4: Part of a spot pattern with high black level of the framegrabber. The lower parts of the spots are missing. It is also possible, that darker spots are completely missing. **a)**Part of spot pattern **b)**2-d-plot of gray values

Case	max. gray level in image	% of pixels with max. gray value	min. gray level in image	% of pixels with zero gray level
perfect pattern	$\sim 255$	$<0.1$	0	0 – 50
saturation	255	$>0.1$	-	-
low light	$<200$	0	-	-
high underground	-	-	$>0$	0
black image	-	-	0	$>50$

Table 5.1: Summary of the parameters identifying the four cases of required adjustments of the black and white levels in the framegrabber responsible for the quality of the spot patterns. All values are the result of numerous tests with different conditions and could vary for different setups

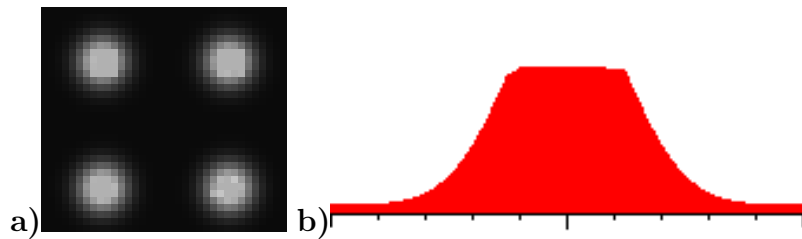


Figure 5.5: A spot pattern with saturation of the camera **a)**part of spot pattern **b)**2-d-plot of gray values

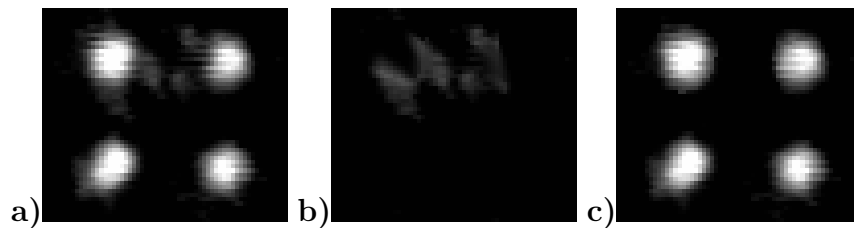


Figure 5.6: Example for removing stationary artifacts by subtracting images. **a)**detail of original image **b)**detail of original image without HSS pattern **c)**detail of image after difference

similar gray values in the center of each spot. This problem can't be solved by adjusting the parameters of the framegrabber. A decreasing of the incoming light level is necessary. This can be corrected by adjusting the laser power or by using a gray filter. With the optical setup used for all the measurements, spot patterns from human eyes will never produce light levels at the camera that are nearly that high.

In some optical setups additional reflections caused by optical components are unavoidable. If they are stationary and their intensity does not exceed the intensity of the real HSS spot pattern, it is possible to remove them by software. For this task an image without HSS pattern is required to build the difference (see fig. 5.6).

## 5.2 Spotfinding algorithms

The most important part of the image processing with HSS spot patterns is the spot finding algorithm. It consists of the recognition of the focus points, the determination of the position of the centers and the assignment of these points to the corresponding subapertures.

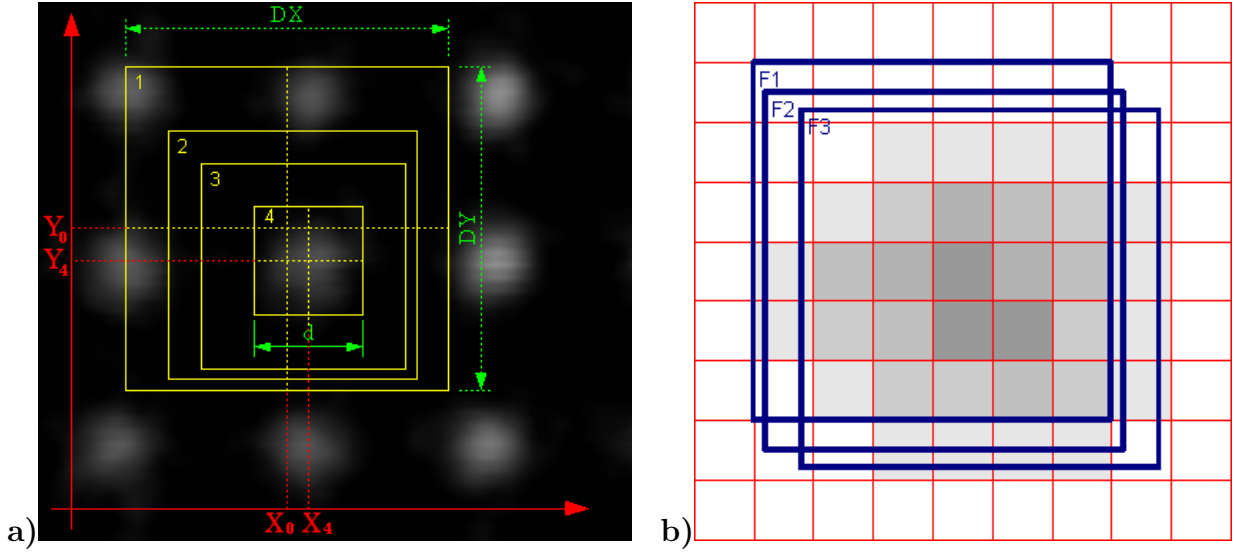


Figure 5.7: A spot pattern with perfect adjustment of framegrabber, camera and laser  
 a) part of spot pattern b) 2-d-plot of gray values

### 5.2.1 Spot centering

The spot centering algorithm is part of all the following strategies. After an area of the image is chosen where one spot is expected, this algorithm starts. The required parameters are the position of the expected spot  $(X, Y)$ , the size of the frame  $(DX, DY)$  that should be used for this centering procedure and the maximum diameter of the spots  $(D)$ . The centering procedure is based on a number of iterative calculations of the center of mass of the gray values  $(G_i)$  where the result of the previous step is used as starting point for the next step.

$$\bar{x} = \frac{1}{n} \sum_{i=1}^n G_i \cdot x_i; \quad \bar{y} = \frac{1}{n} \sum_{i=1}^n G_i \cdot y_i \quad (5.1)$$

The iteration consists of two phases. The first phase starts with a frame size of  $(DX, DY)$  and continues with smaller frames down to the expected size of the spots (see fig. 5.7a). After 3-10 iterations this phase can achieve an accuracy of about 1 pixel ( $\sim 10 \mu m$ ). For better results the second phase with constant frame size continues with another 10-50 iterations. Simulations with different images showed that the number of required iterations decreases with better image quality. Images with very much noise and a high underground level showed that even after 50 iterations the spot position could change a little bit with further iteration s.

For better results the centering process can be extended by using fragments of pixel [Mue01]. An example for this process with sub pixel accuracy is shown in fig. 5.7 b).

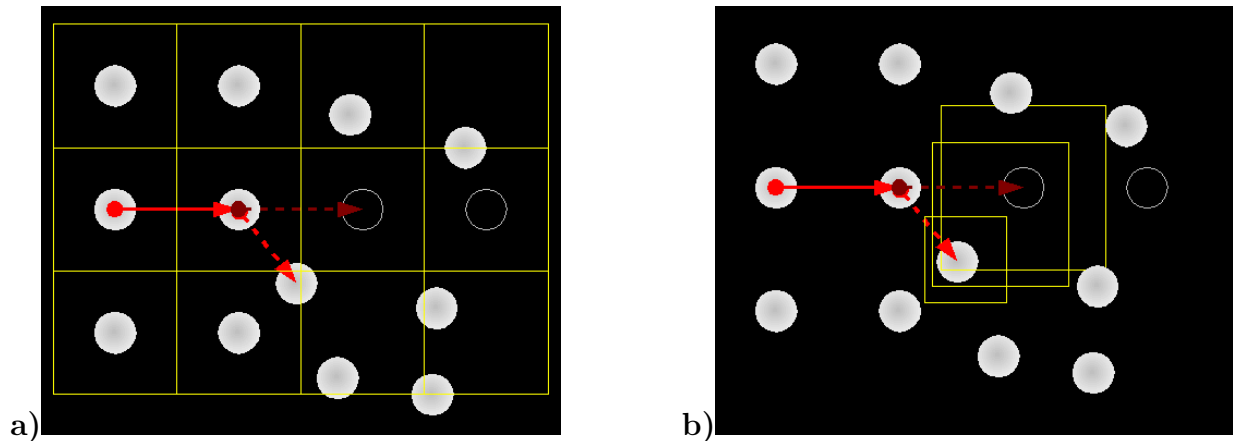


Figure 5.8: A spot pattern with perfect adjustment of framegrabber, camera and laser  
 a) part of spot pattern b) 2-d-plot of gray values

### 5.2.2 Static spotfinding

The first approach for the spotfinding strategy is to use a fixed grid to find the spots. This procedure requires the assumption that no spot can move as much as half the distance between two subapertures. Once started with one frame only a few iterations are required to find the spot because you can be sure that only pixels of one spot are within the frame and this frame is the correct one. This procedure fails if one spot has moved more than half the distance because a correct assignment is not still possible (fig. 5.8a). This means a strong limitation to the processable wavefronts. For an optical setup using an lens array with a distance between the subapertures of  $400\ \mu\text{m}$  and a focal length of  $53\ \text{mm}$  the maximum spot translation is  $200\ \mu\text{m}$  and the maximum local wavefront tilt is about  $0.2$  degree. Similar tilts appear in the external fields of an wavefront with a diameter of  $6\ \text{mm}$  and a sphere of about  $1\ \text{dpt}$ . Astigmatism and higher order aberrations as they are present in many human eyes are often responsible for additional tilts with the result that the dynamic range of the wavefront sensor is limited to wavefronts less than this  $1\ \text{dpt}$ . Measurements at human eyes using the static spotfinding algorithm require good alignment of the eye in addition with good precompensation of the main refractive errors.

### 5.2.3 Adaptive spotfinding

For spot patterns that don't look almost like a spot pattern generated by a plane wave a more intelligent spotfinding algorithm is required. It should allow the recognition and assignment of spots like those in fig. 5.9. Although these spot patterns doesn't match to any fixed grid, nobody should have a problem to assign all visible spots correctly. The approach of the adaptive spotfinding algorithm is to imitate the way a human would assign the spots. The easiest way is to look for something that looks like the expected pattern. This can be found most likely in the center of the whole pattern where the distance between

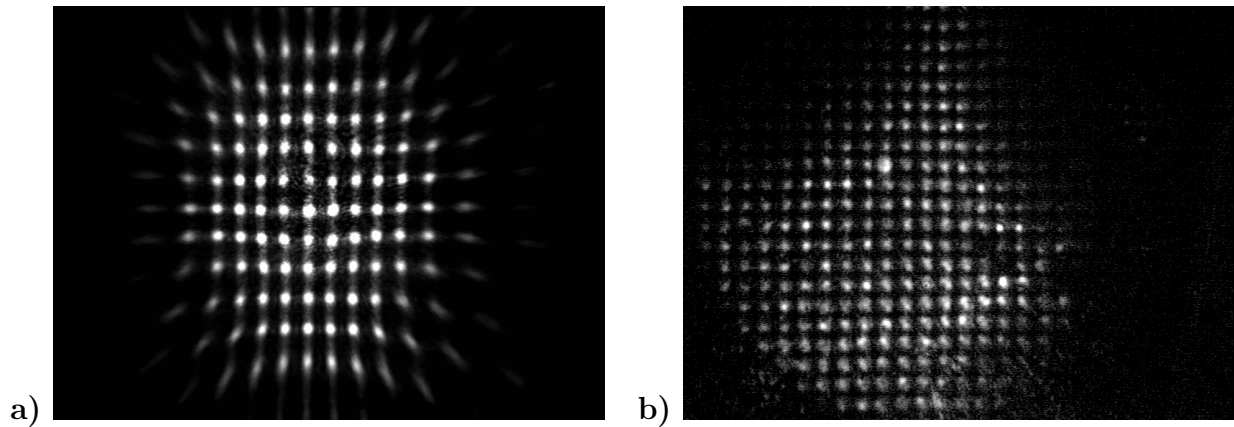


Figure 5.9: Spot patterns from distorted wavefronts that can't be processed by the static spotfinding algorithm **a)** High spherical aberration **b)** Human eye with strong aberrations

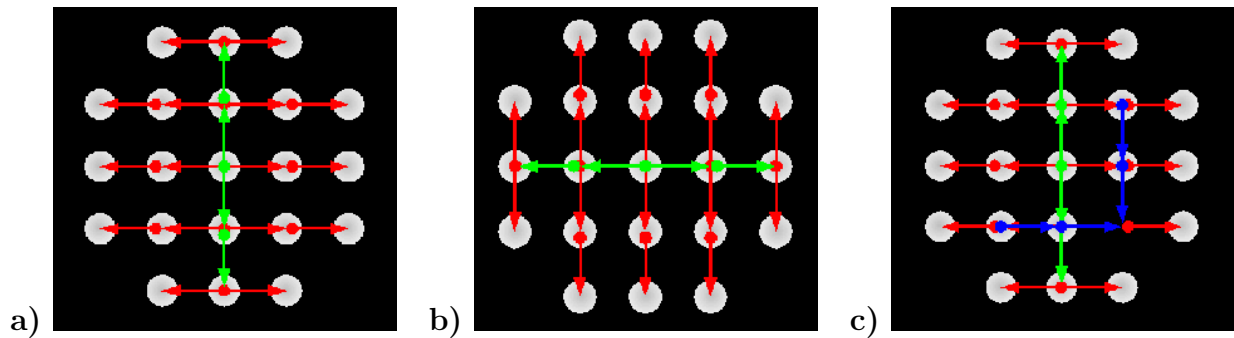


Figure 5.10: Different paths of the searching process. **a)** starting with vertical search, then horizontal **b)** starting with horizontal search, then vertical. The algorithm uses both and compares the results. If there are any differences, the search will be repeated with modified parameters. **c)** Interpolation of a missing spot

the spots can be determined easily. Starting with this distance you can exceed the field by interpolating the pattern subsequently to the external spots. At positions where nothing can be found, but a spot is expected, the search process can be intensified. If there is nothing at all, the surrounding spots can be used to determine the position of this spot. Later in this chapter it will be shown, that the position of one spot of a HSS pattern is completely determined by the position of the surrounding spots.

## 5.3 Modal wavefront estimation

A Hartmann-Shack wavefront sensor is suitable to detect local tilts of the wavefront in the plane of the lens array. With these information it is still a long way to get a function  $W^*(x, y)$  representing the wavefront. For a limitation of the amount of data, it is reasonable to develop the wavefront function  $W^*(x, y)$  in known functions  $f_i(x, y)$ . The wavefront is now determined by

$$z = W^*(x, y) = \sum_i c_i f_i(x, y) \quad (5.2)$$

where the  $c_i$  are a finite number of coefficients.

### 5.3.1 Estimation of wavefront deviations

The data acquired using the Hartmann-Shack sensor, is a set of mean deviations in x-direction  $P_n$  at the positions  $(x_n, y_n)$  of each lensarray and a set of deviations in y-direction at the same location. The values of  $x$  and  $y$  extend from  $-1$  to  $1$  and have no dimensions. The real dimensions can easily be calculated by a multiplication with the real dimensions of the lensarray. An example for a square  $4 \times 4$  lensarray is shown in figure 5.11.

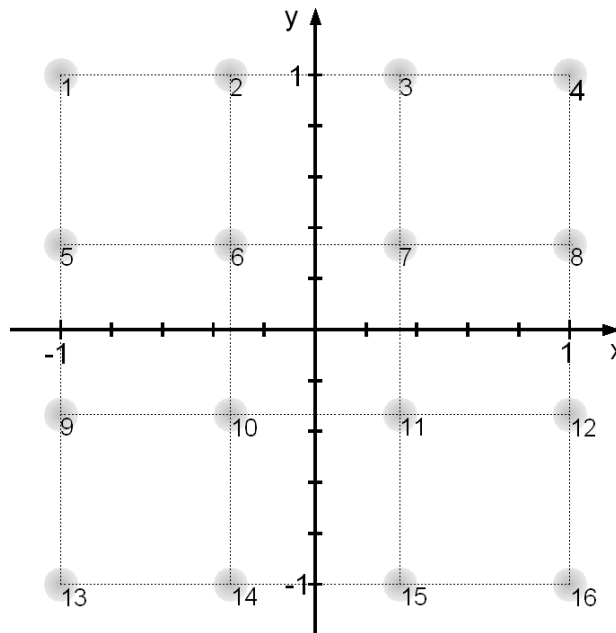


Figure 5.11: square  $4 \times 4$ -lensarray in coordinate system

In the  $4 \times 4$ -example we have  $N = 16$  values for the measured derivatives  $P_n$  and  $Q_n$ .

$$\begin{aligned} P_n &= \frac{d}{dx}W(x_n, y_n) \\ Q_n &= \frac{d}{dy}W(x_n, y_n) \end{aligned} \quad n = 0 \dots N \quad (5.3)$$

For both directions we want to find a function that fits best to the measured values. The estimated wavefront derivatives can be developed in functions  $L_i(x, y)$ :

$$\begin{aligned} \frac{d}{dx}W(x, y) &= \sum_i k_i L_i(x, y) \\ \frac{d}{dy}W(x, y) &= \sum_i l_i L_i(x, y) \end{aligned} \quad j = 0 \dots J \quad (5.4)$$

For the optimization of the estimation, a least-square-fit is used.

$$S_x = \sum_{n=1}^N \left( \frac{d}{dx}W^*(x_n, y_n) - P_n \right)^2 = \sum_{n=1}^N \left( \sum_i k_i L_i(x_n, y_n) - P_n \right)^2 \quad (5.5)$$

$$S_y = \sum_{n=1}^N \left( \frac{d}{dy}W^*(x_n, y_n) - Q_n \right)^2 = \sum_{n=1}^N \left( \sum_i l_i L_i(x_n, y_n) - Q_n \right)^2 \quad (5.6)$$

Minimization demands:

$$0 = \frac{dS}{dk_j} = 2 \sum_{n=1}^N \left( \sum_i k_i L_i(x_n, y_n) - P_n \right) L_j(x_n, y_n) \quad \forall j \quad (5.7)$$

$$0 = \frac{dS}{dl_j} = 2 \sum_{n=1}^N \left( \sum_i l_i L_i(x_n, y_n) - Q_n \right) L_j(x_n, y_n) \quad \forall j \quad (5.8)$$

Resolving the braces, we obtain:

$$\sum_{n=1}^N P_n L_j(x_n, y_n) = \sum_i k_i \sum_{n=1}^N L_i(x_n, y_n) L_j(x_n, y_n) \quad (5.9)$$

$$\sum_{n=1}^N Q_n L_j(x_n, y_n) = \sum_i l_i \sum_{n=1}^N L_i(x_n, y_n) L_j(x_n, y_n) \quad (5.10)$$

For both directions we have a set of  $J$  equations which should be solved simultaneously. These calculations can be simplified by using orthogonal functions  $L_i(x, y)$ . Orthogonality demands:

$$\sum_{n=1}^N L_i(x_n, y_n) L_j(x_n, y_n) = 0 \quad ; \quad \forall i \neq j \quad (5.11)$$

Now we have two sets of  $J$  independent equations.

$$k_j = \frac{\sum_{n=1}^N P_n L_j(x_n, y_n)}{\sum_{n=1}^N L_j^2(x_n, y_n)} \quad (5.12)$$

$$l_j = \frac{\sum_{n=1}^N Q_n L_j(x_n, y_n)}{\sum_{n=1}^N L_j^2(x_n, y_n)} \quad (5.13)$$

The set of orthogonal functions  $L_i$  used for the following calculations is:

### 1. Order

$$L_0 = 1 \quad (5.14)$$

### 2. Order

$$\begin{aligned} L_1 &= x \\ L_2 &= y \end{aligned} \quad (5.15)$$

### 3. Order

$$\begin{aligned} L_3 &= 2xy \\ L_4 &= c_1 x^2 + c_1 y^2 - 1 \\ L_5 &= -x^2 + y^2 \end{aligned} \quad (5.16)$$

### 3. Order

$$\begin{aligned} L_6 &= c_2 x y^2 - x^3 \\ L_7 &= c_3 x^3 + c_4 x y^2 - 2x \\ L_8 &= c_3 y^3 + c_4 y x^2 - 2y \\ L_9 &= y^3 - c_2 y x^2 \end{aligned} \quad (5.17)$$



**4. Order**

$$\begin{aligned}
L_{10} &= -4x^3y + 4xy^3 \\
L_{11} &= c_5x^3y + c_5xy^3 - 6xy \\
L_{12} &= c_6x^4 + c_7x^2y^2 + c_6y^4 - c_8x^2 - c_8y^2 + 1 \\
L_{13} &= -c_9x^4 + c_9y^4 + 3x^2 - 3y^2 \\
L_{14} &= x^4 + c_{11}x^2 - c_{10}x^2y^2 + c_{11}y^2 + y^4
\end{aligned} \tag{5.18}$$

**5. Order**

$$\begin{aligned}
L_{15} &= c_{12}xy^4 - c_{13}x^3y^2 + c_{14}x^3 + x^5 \\
L_{16} &= c_{15}x^3y^2 - c_{16}x^5 + c_{17}xy^4 - c_{18}xy^2 + 4x^3 \\
L_{17} &= c_{19}x^5 + c_{20}x^3y^2 + c_{21}xy^4 - c_{22}x^3 - c_{23}xy^2 + 3x \\
L_{18} &= c_{21}yx^4 + c_{20}x^2y^3 + c_{19}y^5 - c_{23}yx^2 - c_{22}y^3 + 3y \\
L_{19} &= -c_{15}x^2y^3 - c_{17}yx^4 + c_{16}y^5 - 4y^3 + c_{18}yx^2 \\
L_{20} &= y^5 - c_{13}x^2y^3 + c_{14}yx^4 + c_{14}x^3
\end{aligned} \tag{5.19}$$

**6. Order**

$$\begin{aligned}
L_{21} &= c_{24}x^5y - 20x^3y^3 + c_{24}xy^5 \\
L_{22} &= -c_{25}x^5y + c_{25}xy^5 + 20x^3y - 20xy^3 \\
L_{23} &= c_{26}x^5y + c_{27}x^3y^3 + c_{26}xy^5 - c_{28}x^3y - c_{28}xy^3 + 12xy \\
L_{24} &= c_{29}x^6 + c_{30}x^4y^2 + c_{30}x^2y^4 + c_{29}y^6 - c_{31}x^4 - c_{32}x^2y^2 - c_{31}y^4 \\
&\quad + c_{33}x^2 + c_{33}y^2 - 1 \\
L_{25} &= -c_{34}x^6 - c_{35}x^4y^2 + c_{35}x^2y^4 + c_{34}y^6 + c_{36}x^4 - c_{36}y^4 - 6x^2 + 6y^2 \\
L_{26} &= c_{37}x^6 - c_{38}x^4y^2 - c_{38}x^2y^4 + c_{37}y^6 - c_{39}x^4 + 30x^2y^2 - c_{39}y^4 \\
L_{27} &= -x^6 + c_{40}x^4y^2 - c_{40}x^2y^4 + y^6
\end{aligned} \tag{5.20}$$

The coefficients  $c_i$  can be obtained with equation 5.11. Since there are several symmetries, it is not necessary to multiply every combination of these 28 polynomials. The system of 40 variables can be divided in 6 subsystems, that are independent of each other. Products of polynomials of different subsystems are always zero. The subsystems with their symmetries are shown in table 5.2.

subsystem	polynomials	symmetries			
		$L_i(x, y) = L_i(-x, y)$	$L_i(x, y) = L_i(x, -y)$	$L_i(x, y) = L_i(y, x)$	$L_i(x, y) = -L_i(y, x)$
A	$L_0, L_4, L_{12}, L_{14}, L_{24}, L_{26}$	✓	✓	✓	
B	$L_5, L_{13}, L_{25}, L_{27}$	✓	✓		
C	$L_3, L_{11}, L_{21}, L_{23}$			✓	
D	$L_{10}, L_{22}$				✓
E	$L_2, L_8, L_9, L_{18}, L_{19}, L_{20}$	✓			
F	$L_1, L_6, L_7, L_{15}, L_{16}, L_{17}$		✓		

Table 5.2: Subsystems of the orthogonal polynomials with symmetries

For an increasing number of sublenses in a circular pattern, the polynomials  $L_j$  approximate the Zernike Polynomials (see next section). This fact can be seen in fig. 5.12 for the first two coefficients  $c_1$  and  $c_2$  with the polynomials  $L_4, L_6$  and  $L_9$ .

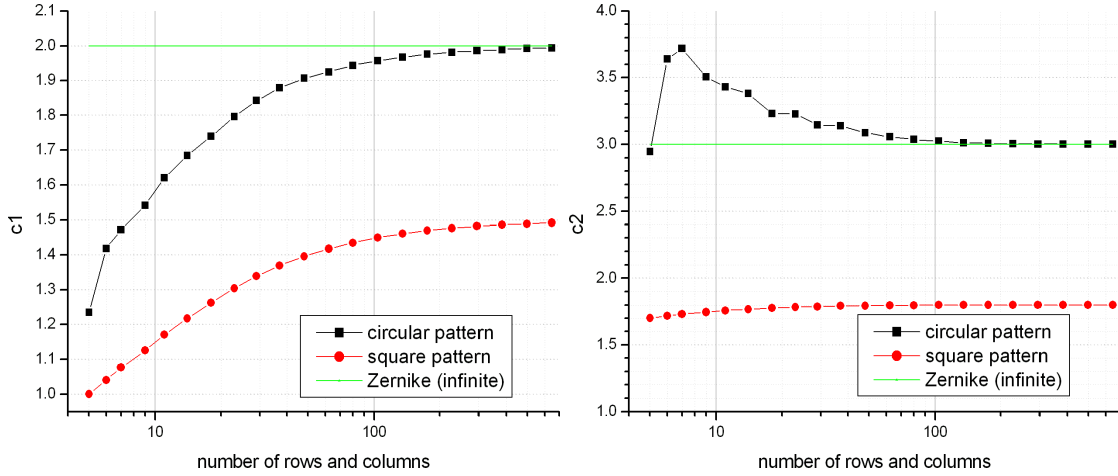


Figure 5.12: Comparison of the coefficients  $c_1$  and  $c_2$  in the orthogonal polynomials and the corresponding values in the Zernike Polynomials

### 5.3.2 Development of the wavefront in Taylor Polynomials

The easiest representation of the wavefront is development in a Taylor Polynomials.

$$\begin{aligned}
W^*(x, y) = & a_0 + a_1x + a_2y + a_3x^2 + a_4xy + a_5y^2 + a_6x^3 \\
& + a_7xy^2 + a_8x^2y + a_9y^3 + a_{10}x^4 + a_{11}xy^3 \\
& + a_{12}x^2y^2 + a_{13}x^3y + a_{14}y^4 \dots
\end{aligned} \tag{5.21}$$

The derivation in both directions should now be equal to the derivations calculated in the previous section:

$$\begin{aligned}
\frac{d}{dx}(a_1x + a_2y + a_3x^2 \dots) &= \sum_i k_i L_i \\
\frac{d}{dy}(a_1x + a_2y + a_3x^2 \dots) &= \sum_i l_i L_i
\end{aligned} \tag{5.22}$$

With this set of 20 equations we can determine the coefficients in equation 5.21. The coefficients which can be calculated using both  $k_i$ - and  $l_i$ -coefficients are calculated using the mean of these values.

$$\begin{aligned}
a_0 &= 0 \\
a_1 &= -k_4 + k_{12} + k_0 \\
a_2 &= -l_4 + l_0 + l_{12} \\
a_3 &= \frac{3}{2}k_{17} + \frac{1}{2}k_1 - k_7 \\
a_4 &= k_2 - 2k_8 + 3k_{18} - 2l_7 + 3l_{17} + l_1 \\
a_5 &= \frac{1}{2}l_2 - l_8 + \frac{3}{2}l_{18} \\
a_6 &= -\frac{1}{3}k_5 + k_{13} - \frac{1}{3}k_{12}c_8 + \frac{1}{3}k_4c_1 + \frac{1}{3}k_{14}c_{11} \\
a_7 &= -3k_{11} + k_3 + l_4c_1 - l_5 + 3l_{13} - l_{12}c_8 + l_{14}c_{11} \\
a_8 &= -k_{12}c_8 + k_5 + k_{14}c_{11} + k_4c_1 - 3k_{13} - 3l_{11} + l_3 \\
a_9 &= -\frac{1}{3}l_{12}c_8 + \frac{1}{3}l_4c_1 - l_{13} + \frac{1}{3}l_{14}c_{11} + \frac{1}{3}l_5 \\
a_{10} &= \frac{1}{4}k_{15}c_{14} - \frac{1}{4}k_{17}c_{22} + k_{16} - \frac{1}{4}k_6 + \frac{1}{4}k_7c_3 \\
a_{11} &= \frac{1}{3}k_8c_4 - \frac{1}{3}k_9c_2 - \frac{1}{3}k_{18}c_{23} + \frac{1}{3}k_{19}c_{18} - l_{17}c_{22} + l_{15}c_{14} + l_7c_3 - l_6 + 4l_{16} \\
a_{12} &= -\frac{1}{2}k_{16}c_{18} - \frac{1}{2}k_{17}c_{23} + \frac{1}{2}k_6c_2 + \frac{1}{2}k_7c_4 - \frac{1}{2}l_9c_2 + \frac{1}{2}l_{19}c_{18} - \frac{1}{2}l_{18}c_{23} + \frac{1}{2}l_8c_4 \\
a_{13} &= k_9 - 4k_{19} + k_8c_3 + k_{20}c_{14} - k_{18}c_{22} + \frac{1}{3}l_6c_2 + \frac{1}{3}l_7c_4 - \frac{1}{3}l_{17}c_{23} - \frac{1}{3}l_{16}c_{18} \\
a_{14} &= -\frac{1}{4}l_{18}c_{22} - l_{19} + \frac{1}{4}l_8c_3 + \frac{1}{4}l_9 + \frac{1}{4}l_{20}c_{14}
\end{aligned}$$

$$\begin{aligned}
a_{15} &= \frac{1}{5}k_{12}c_6 + \frac{1}{5}k_{14} - \frac{1}{5}k_{13}c_9 \\
a_{16} &= -k_{10} + \frac{1}{4}k_{11}c_5 + l_{14} + l_{12}c_6 - l_{13}c_9 \\
a_{17} &= \frac{1}{3}k_{12}c_7 - \frac{1}{3}k_{14}c_{10} + \frac{1}{2}l_{11}c_5 - 2l_{10} \\
a_{18} &= 2k_{10} + \frac{1}{2}k_{11}c_5 + \frac{1}{3}l_{12}c_7 - \frac{1}{3}l_{14}c_{10} \\
a_{19} &= k_{14} + k_{12}c_6 + k_{13}c_9 + \frac{1}{4}l_{11}c_5 + l_{10} \\
a_{20} &= \frac{1}{5}l_{12}c_6 + \frac{1}{5}l_{13}c_9 + \frac{1}{5}l_{14} \\
a_{21} &= \frac{1}{6}k_{17}c_{19} + \frac{1}{6}k_{15} - \frac{1}{6}k_{16}c_{16} \\
a_{22} &= \frac{1}{5}k_{18}c_{21} - \frac{1}{5}k_{19}c_{17} + \frac{1}{5}k_{20}c_{12} + l_{17}c_{19} - l_{16}c_{16} + l_{15} \\
a_{23} &= \frac{1}{4}k_{16}c_{15} - \frac{1}{4}k_{15}c_{13} + \frac{1}{4}k_{17}c_{20} - \frac{1}{2}l_{19}c_{17} + \frac{1}{2}l_{18}c_{21} + \frac{1}{2}l_{20}c_{12} \\
a_{24} &= -\frac{1}{3}k_{19}c_{15} - \frac{1}{3}k_{20}c_{13} + \frac{1}{3}k_{18}c_{20} - \frac{1}{3}l_{15}c_{13} + \frac{1}{3}l_{17}c_{20} + \frac{1}{3}l_{16}c_{15} \\
a_{25} &= \frac{1}{2}k_{16}c_{17} + \frac{1}{2}k_{15}c_{12} + \frac{1}{2}k_{17}c_{21} + \frac{1}{4}l_{18}c_{20} - \frac{1}{4}l_{19}c_{15} - \frac{1}{4}l_{20}c_{13} \\
a_{26} &= k_{19}c_{16} + k_{18}c_{19} + k_{20} + \frac{1}{5}l_{16}c_{17} + \frac{1}{5}l_{15}c_{12} + \frac{1}{5}l_{17}c_{21} \\
a_{27} &= \frac{1}{6}l_{19}c_{16} + \frac{1}{6}l_{20} + \frac{1}{6}l_{18}c_{19}
\end{aligned}$$

### 5.3.3 Development of the wavefront in Zernike Polynomials

The most suitable polynomials for optical applications are the Zernike Polynomials[Zer34]. The first 28 polynomials are listed below. The visualization of these polynomials is shown in fig. 5.13. More about calculation and higher orders of Zernike Polynomials can be found in appendix A.

$$\begin{aligned}
Z_0 &= 1 \\
Z_1 &= x \\
Z_2 &= y \\
Z_3 &= 2xy && \text{(astigmatism } \pm 45^\circ) \\
Z_4 &= 2x^2 + 2y^2 - 1 && \text{(defocus)} \\
Z_5 &= -x^2 + y^2 && \text{(astigmatism) } 0^\circ / 90^\circ \\
Z_6 &= 3xy^2 - x^3 \\
Z_7 &= 3x^3 + 3xy^2 - 2x && \text{(x - coma)} \\
Z_8 &= 3yx^2 + 3y^3 - 2y && \text{(y - coma)} \\
Z_9 &= y^3 - 3yx^2 \\
Z_{10} &= -4x^3y + 4xy^3 \\
Z_{11} &= 8x^3y + 8xy^3 - 6xy \\
Z_{12} &= 6x^4 + 12x^2y^2 + 6y^4 - 6x^2 - 6y^2 + 1 && \text{(3. order sph. aberration)} \\
Z_{13} &= -4x^4 + 4y^4 + 3x^2 - 3y^2 \\
Z_{14} &= x^4 - 6x^2y^2 + y^4 \\
Z_{15} &= 5xy^4 - 10x^3y^2 + x^5 \\
Z_{16} &= 10x^3y^2 - 5x^5 + 15xy^4 - 12xy^2 + 4x^3 \\
Z_{17} &= 10x^5 + 20x^3y^2 + 10xy^4 - 12x^3 - 12xy^2 + 3x \\
Z_{18} &= 10yx^4 + 20x^2y^3 + 10y^5 - 12yx^2 - 12y^3 + 3y \\
Z_{19} &= -10x^2y^3 - 15yx^4 + 5y^5 - 4y^3 + 12yx^2 \\
Z_{20} &= y^5 - 10x^2y^3 + 5yx^4 \\
Z_{21} &= 6x^5y - 20x^3y^3 + 6xy^5 \\
Z_{22} &= -24x^5y + 24xy^5 + 20x^3y - 20xy^3 \\
Z_{23} &= 30x^5y + 60x^3y^3 + 30xy^5 - 40x^3y - 40xy^3 + 12xy \\
Z_{24} &= 20x^6 + 60x^4y^2 + 60x^2y^4 + 20y^6 - 30x^4 - 60x^2y^2 - 30y^4 \\
&\quad + 12x^2 + 12y^2 - 1 && \text{(4. order sph. aberration)} \\
Z_{25} &= -15x^6 - 15x^4y^2 + 15x^2y^4 + 15y^6 + 20x^4 - 20y^4 - 6x^2 + 6y^2 \\
Z_{26} &= 6x^6 - 30x^4y^2 - 30x^2y^4 + 6y^6 - 5x^4 + 30x^2y^2 - 5y^4 \\
Z_{27} &= -x^6 + 15x^4y^2 - 15x^2y^4 + y^6
\end{aligned}$$

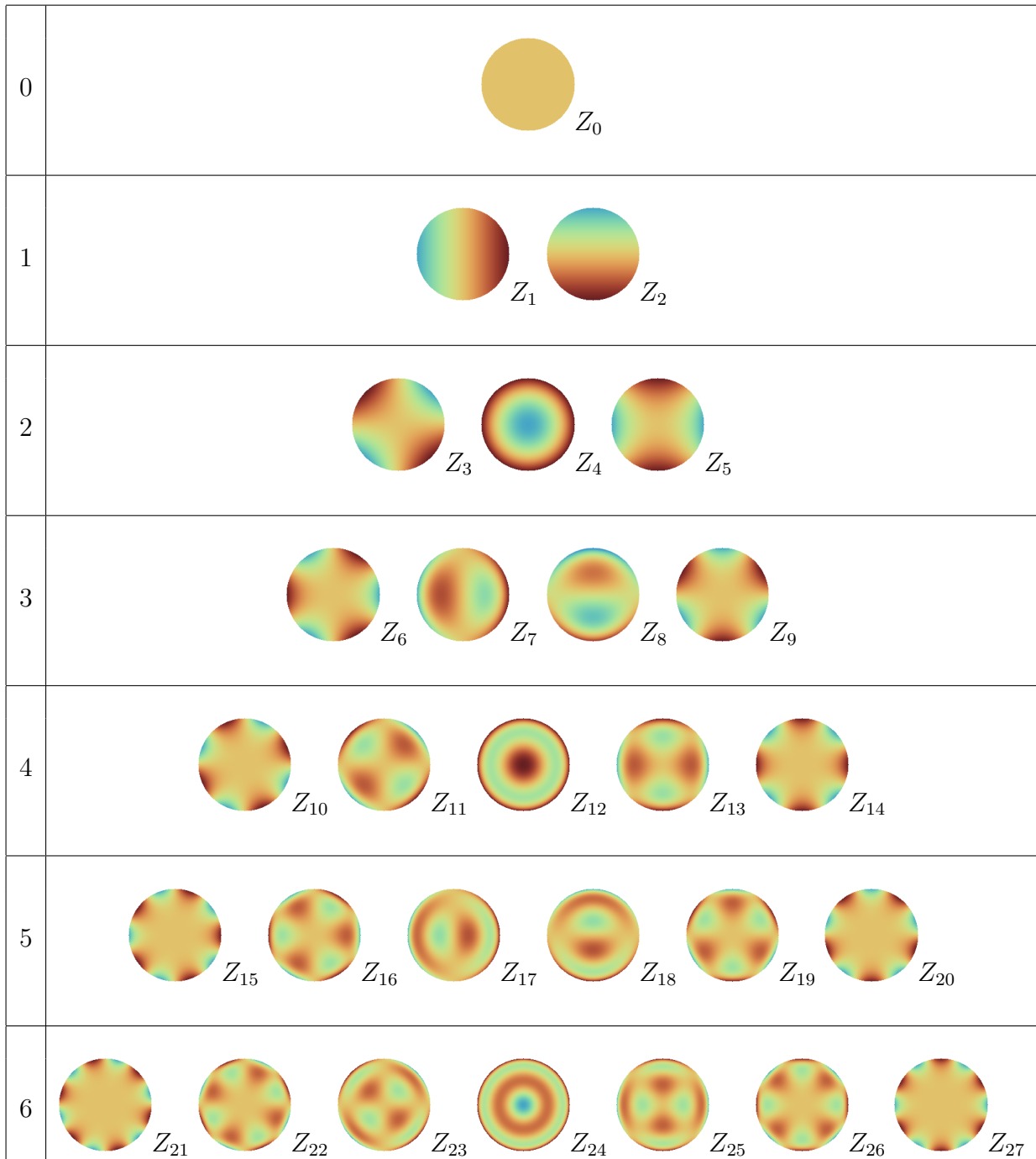


Figure 5.13: Visualization of Zernike Polynomials up to 6. order

The representation of the wavefront  $W(x, y)$  with Zernike Polynomials is:

$$W(x, y) = \sum_i z_i Z_i(x, y) \quad (5.23)$$

The coefficients  $z_i$  can be calculated from the Taylor coefficients  $a_i$ .

$$\begin{aligned}
z_1 &= a_1 + \frac{1}{6} a_8 + \frac{1}{2} a_6 + \frac{1}{16} a_{17} + \frac{5}{16} a_{15} + \frac{1}{16} a_{19} \\
z_2 &= a_2 + \frac{1}{6} a_7 + \frac{1}{2} a_9 + \frac{5}{16} a_{20} + \frac{1}{16} a_{18} + \frac{1}{16} a_{16} \\
z_3 &= \frac{1}{2} a_4 + \frac{3}{16} a_{11} + \frac{3}{16} a_{13} + \frac{3}{32} a_{22} + \frac{9}{160} a_{24} + \frac{3}{32} a_{26} \\
z_4 &= \frac{1}{4} a_5 + \frac{1}{4} a_3 + \frac{3}{16} a_{14} + \frac{3}{16} a_{10} + \frac{1}{16} a_{12} + \frac{67}{2560} a_{25} + \frac{77}{2560} a_{23} + \frac{87}{512} a_{21} + \frac{57}{512} a_{27} \\
z_5 &= -\frac{1}{2} a_3 + \frac{1}{2} a_5 - \frac{3}{8} a_{10} + \frac{3}{8} a_{14} - \frac{9}{32} a_{21} - \frac{3}{160} a_{23} + \frac{3}{160} a_{25} + \frac{9}{32} a_{27} \\
z_6 &= -\frac{1}{4} a_6 + \frac{1}{4} a_8 + \frac{1}{20} a_{17} - \frac{1}{4} a_{15} + \frac{3}{20} a_{19} \\
z_7 &= \frac{1}{12} a_8 + \frac{1}{4} a_6 + \frac{1}{20} a_{17} + \frac{1}{4} a_{15} + \frac{1}{20} a_{19} \\
z_8 &= \frac{1}{12} a_7 + \frac{1}{4} a_9 + \frac{1}{4} a_{20} + \frac{1}{20} a_{18} + \frac{1}{20} a_{16} \\
z_9 &= \frac{1}{4} a_9 - \frac{1}{4} a_7 + \frac{1}{4} a_{20} - \frac{1}{20} a_{18} - \frac{3}{20} a_{16} \\
z_{10} &= \frac{1}{8} a_{13} - \frac{1}{8} a_{11} - \frac{5}{48} a_{22} + \frac{5}{48} a_{26} \\
z_{11} &= \frac{1}{16} a_{11} + \frac{1}{16} a_{13} + \frac{5}{96} a_{22} + \frac{1}{32} a_{24} + \frac{5}{96} a_{26} \\
z_{12} &= \frac{1}{16} a_{14} + \frac{1}{16} a_{10} + \frac{1}{48} a_{12} + \frac{23}{1536} a_{25} + \frac{25}{1536} a_{23} + \frac{45}{512} a_{21} + \frac{35}{512} a_{27} \\
z_{13} &= -\frac{1}{8} a_{10} + \frac{1}{8} a_{14} - \frac{5}{32} a_{21} - \frac{1}{96} a_{23} + \frac{1}{96} a_{25} + \frac{5}{32} a_{27} \\
z_{14} &= -\frac{1}{8} a_{12} + \frac{1}{8} a_{14} + \frac{1}{8} a_{10} - \frac{37}{768} a_{25} - \frac{43}{768} a_{23} + \frac{25}{256} a_{21} + \frac{55}{256} a_{27} \\
z_{15} &= \frac{1}{16} a_{15} + \frac{1}{16} a_{19} - \frac{1}{16} a_{17} \\
z_{16} &= \frac{3}{80} a_{19} - \frac{1}{16} a_{15} + \frac{1}{80} a_{17} \\
z_{17} &= \left. \frac{1}{80} a_{17} + \frac{1}{16} a_{15} + \frac{1}{80} a_{19} \right\} \\
z_{18} &= \frac{1}{16} a_{20} + \frac{1}{80} a_{18} + \frac{1}{80} a_{16} \\
z_{19} &= -\frac{1}{80} a_{18} + \frac{1}{16} a_{20} - \frac{3}{80} a_{16} \\
z_{20} &= \frac{1}{16} a_{16} + \frac{1}{16} a_{20} - \frac{1}{16} a_{18} \\
z_{21} &= -\frac{1}{32} a_{24} + \frac{1}{32} a_{22} + \frac{1}{32} a_{26} \\
z_{22} &= \frac{1}{48} a_{26} - \frac{1}{48} a_{22} \\
z_{23} &= \frac{1}{96} a_{22} + \frac{1}{160} a_{24} + \frac{1}{96} a_{26} \\
z_{24} &= \frac{1}{320} a_{25} + \frac{1}{320} a_{23} + \frac{1}{64} a_{21} + \frac{1}{64} a_{27} \\
z_{25} &= -\frac{1}{480} a_{23} + \frac{1}{480} a_{25} - \frac{1}{32} a_{21} + \frac{1}{32} a_{27} \\
z_{26} &= \frac{1}{32} a_{21} - \frac{1}{96} a_{25} - \frac{1}{96} a_{23} + \frac{1}{32} a_{27} \\
z_{27} &= \frac{1}{32} a_{27} - \frac{1}{32} a_{25} + \frac{1}{32} a_{23} - \frac{1}{32} a_{21}
\end{aligned} \quad (5.24)$$

## 5.4 Zonal estimation

A completely different approach of wavefront estimation is the integration of the individual wavefront gradients. As it is shown in the previous section, the shift of a focus spot corresponds to a local tilt of the wavefront. If you assume, that the tilts are constant within a subaperture, they can be integrated in the direction of  $x$  and  $y$  to determine the  $z$ -value of the wavefront (see fig. 5.14). The differences in level  $\Delta z_x$  and  $\Delta z_y$  are

$$z_x = d \sin(\beta); \quad z_y = d \sin(\alpha), \quad (5.25)$$

where  $d$  is the diameter of a subaperture and  $\alpha$  and  $\beta$  are the tilts of the wavefront in the direction of  $x$  and  $y$ .

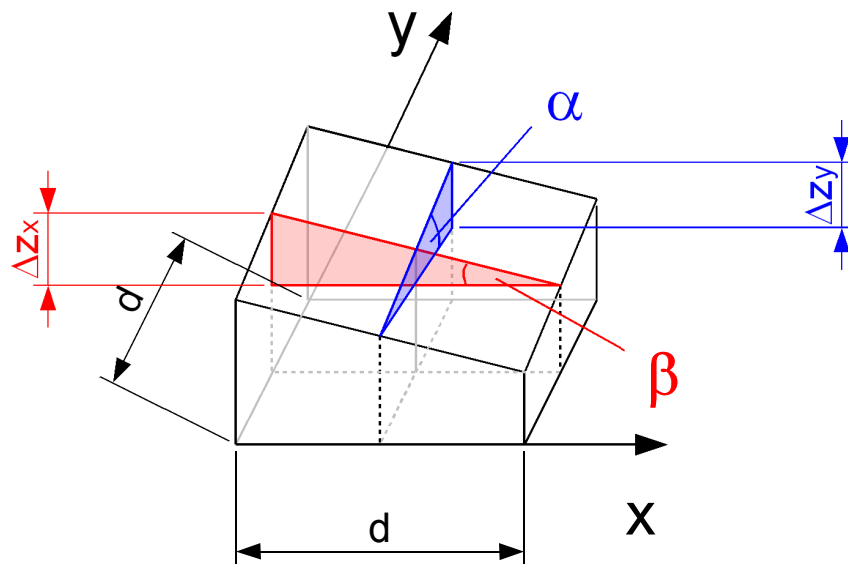


Figure 5.14: Differences in  $z$ -level within one subaperture. The distance  $d$  is the size of one subaperture, the angles  $\alpha$  and  $\beta$  are equal to the local tilts of the wavefront  $\frac{d}{dx}W(x, y)$  and  $\frac{d}{dy}W(x, y)$ .



The z-level at the position of every subaperture can be determined by adding the  $\Delta z_x$  and  $\Delta z_y$  along a path (see fig. 5.15). Since the vector field of the measured tilts is a gradient field, the path doesn't affect the result. A result of this fact is, that the position of one missing spot can be determine by the positions of the surrounding spots. An example is shown in fig. 5.15. The tilt in x-direction within the square with the number 7, that corresponds to one subaperture, can be calculated by using the tilts of the squares with the numbers 6,2,3,4 and 8.

$$\begin{aligned} \frac{d}{dx} W_7 = & -0.5 \frac{d}{dx} W_6 + 0.5 \frac{d}{dy} W_6 + 0.5 \frac{d}{dy} W_2 + 0.5 \frac{d}{dx} W_2 + \frac{d}{dx} W_3 \\ & + 0.5 \frac{d}{dx} W_4 - 0.5 \frac{d}{dy} W_4 - 0.5 \frac{d}{dy} W_8 - 0.5 \frac{d}{dx} W_8 \end{aligned} \quad (5.26)$$

You should get the same result with the squares with numbers 6,10,11,12 and 8. Similar solutions exist for the determination of the tilt in y-direction.

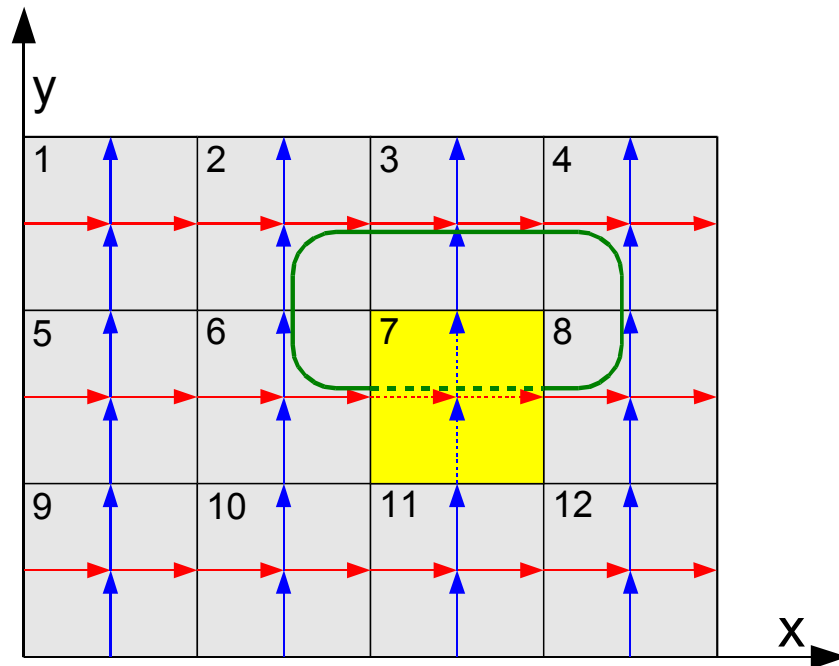


Figure 5.15: Path of integration. For more details, see text

A square grid of the whole wavefront can be calculated this way, even if some intrinsic spots are missing. It is possible to integrate the wavefront along different pathes and to take the mean as more reliable value.

## 5.5 Mixed estimation

Another approach in analyzing wavefronts with Hartmann-Shack wavefront sensors is to take every set of 4 sublenses as a single wavefront sensor. These sensors are only suitable to measure first and second order aberrations. For the following considerations only the second order aberrations ( $Z_3, Z_4, Z_5$ ) are relevant.

$$\begin{aligned} Z_3(2, -2) &= 2xy \\ Z_4(2, 0) &= 2x^2 + 2y^2 - 1 \\ Z_5(2, -2) &= -x^2 + y^2 \end{aligned}$$

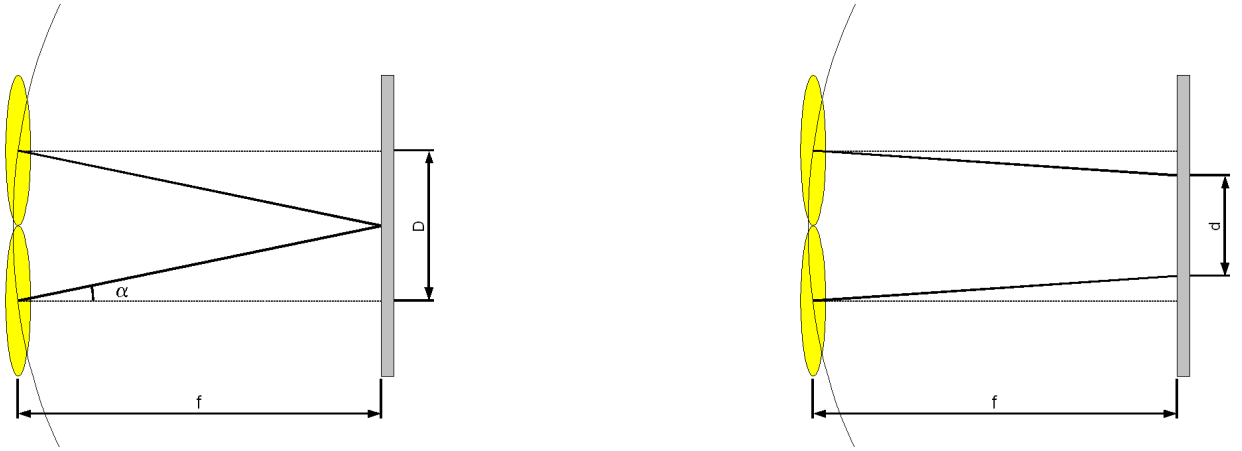


Figure 5.16: Wavefront sensor consisting of only 2 lenses

If the distance  $d$  between two spots (see figure 5.16) is 0, it is obviously, that the defocus of the incoming wavefront is determined by:

$$d = 0 \Rightarrow Z_{sphere}[dpt] = \frac{1}{f} \quad (5.27)$$

Assuming that the diameter  $D$  of the sublenses is small compared with its focal length, it is possible to interpolate equation 5.27 linearly to other distances  $d$ :

$$Z_{sphere}[dpt] = \frac{d - D}{D} \cdot \frac{1}{f} \quad (5.28)$$

This method can be extended to all four sublenses (see figure 5.17). The value of  $d$  now can be substituted by the mean of  $(x_2 - x_1), (x_3 - x_4), (y_4 - y_1)$  and  $(y_3 - y_2)$ . Using these values, equation 5.28 extends to:

$$Z_{sphere}[dpt] = \frac{\frac{1}{4}((x_2 - x_1) + (x_3 - x_4) + (y_4 - y_1) + (y_3 - y_2)) - D}{D} \cdot \frac{1}{f} \quad (5.29)$$

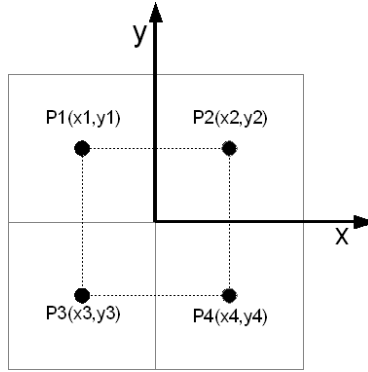


Figure 5.17: Positions of the spots of a 4-lens Hartmann-Shack wavefront sensor

Similar considerations lead to equations for the astigmatism:

$$Z_{\text{astigm}_{0^\circ/90^\circ}} = \frac{d_x - d_y}{D} \cdot \frac{1}{f} = \frac{\frac{1}{2}(x_2 - x_1 + x_4 - x_3) - \frac{1}{2}(y_3 - y_1 + y_4 - y_2)}{D} \cdot \frac{1}{f} \quad (5.30)$$

$$Z_{\text{astigm}_{45^\circ}} = \frac{\sqrt{(x_4 - x_1)^2 + (y_4 - y_1)^2} - \sqrt{(x_2 - x_3)^2 + (y_3 - y_2)^2}}{\sqrt{2} D} \cdot \frac{1}{f} \quad (5.31)$$

The overall astigmatism is:

$$Z_{\text{astig.}} = \sqrt{Z_{\text{astigm}_{45^\circ}}^2 + Z_{\text{astigm}_{0^\circ/90^\circ}}^2} \quad (5.32)$$

The axis is:

$$\alpha = \frac{1}{2} \cdot \arctan \left( \frac{Z_{\text{astigm}_{45^\circ}}}{Z_{\text{astigm}_{0^\circ/90^\circ}}} \right) \quad (5.33)$$

Now we have results for sphere, astigmatism and the corresponding angle for every group of 4 lenses. Examples for complete grids are shown in fig. 5.18.

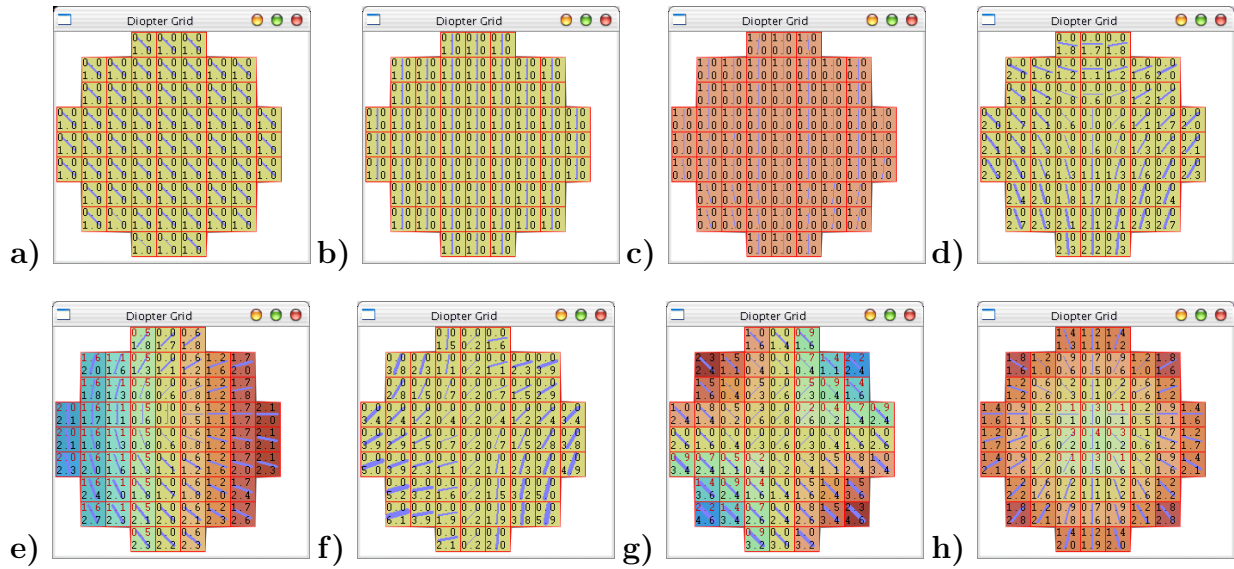


Figure 5.18: Visualization of some Zernike Polynomials as power map. The upper values are the sphere, the lower values, the astigmatism and the lines correspond to the axes of the astigmatism. The color represents the sphere, too. More details about this visualization are given in chapter 6. **a)**  $Z_3$ : Astigmatism at  $45^\circ$  **b)**  $Z_5$ : Astigmatism at  $0^\circ/90^\circ$  **c)**  $Z_4$ : Defocus **d)**  $Z_6$  **e)**  $Z_7$ : Coma **f)**  $Z_{10}$  **g)**  $Z_{11}$  **h)**  $Z_{12}$

### Spherical Aberration

In this paragraph we want to assume that the optical power of the object has radial symmetry. That means, that we can describe the optical power as:

$$D(r) = b_0 + b_1 r^2 + b_2 r^4 + b_3 r^6 + b_4 r^8 + \dots \quad (5.34)$$

In the previous subsection we calculated a set of  $n$  values  $d_i$  for the the center of each pair of four spots. Using the distance from the center of the pupil, we have  $n$  values  $d_i(x_i)$  for the estimation of  $D(x)$ .

# Chapter 6

## Wavefront analysis software

Within the framework of this thesis, four different programs have been written. The first and most complex software is **HSS Analysis 2.x** that is a further development of the software written in [Sch97]. Most of the algorithms mentioned in the previous chapter are implemented in this program.

After the evolution of new software development technologies, a new software development environment was chosen for the further programming of software. Since many parts of this software had to be rewritten, a new program with a completely new user interface was written. This software is called **HSS Analysis 3.x** and has most of the functionality of the previous version and some new additionally features. For the real-time measurements the complex HSS Analysis software was not suitable, so another software had to be developed: The **HSS Real 1.x** software that allows up to 50 measurements in a second. The last software is a simulation software that allows to generate all kinds of spot patterns with the possibility to vary a great number of parameters.

### 6.1 HSS Analysis 2.x

The first and most complex software developed for this thesis is HSS Analysis 2.x. It is an improved and extended version of the software developed at the University of Heidelberg 1997[Sch97]. The software development environment used for this process was Borland C++ 5.0 for Windows. The final program consists of three parts. The first part is the acquisition module. Capturing is possible using framegrabbers produced by Matrox Electronix Systems Ltd.[Mil98] and IDS Imaging Development Systems GmbH[Ids02]. An integrated stepper motor interface allows to change the sphere compensation while capturing a series of images (see figure 6.2).

The second part of HSS Analysis is the processing module. HSS spot patterns can be analyzed automatically or manually with a variety of parameters. In special cases, when spots are missing or if there are extremal higher order aberrations, it could be necessary

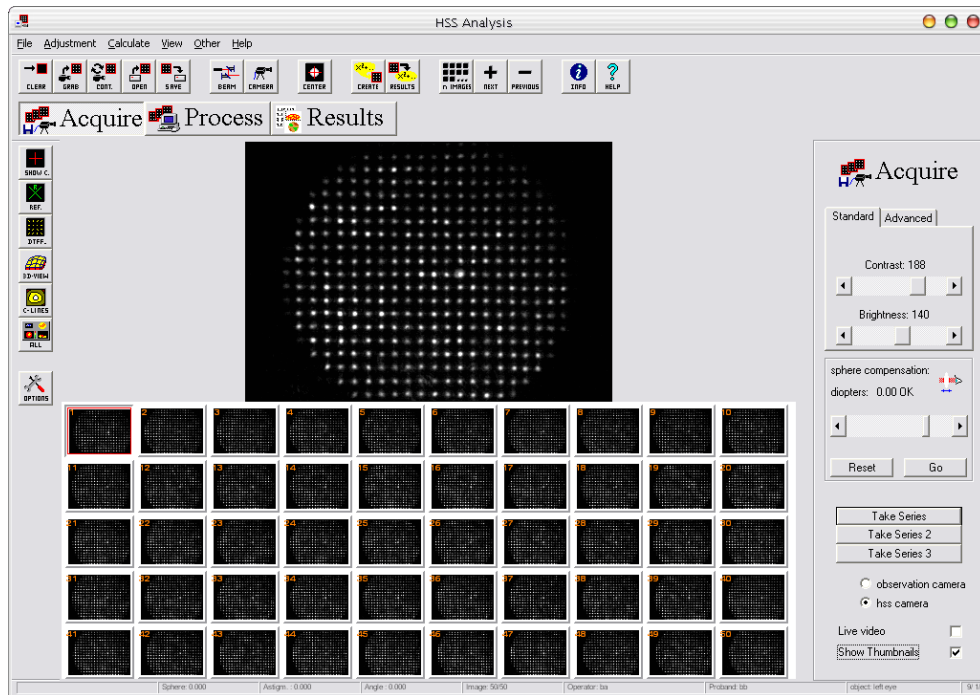


Figure 6.1: All

to adjust some spots manually. An example for a spot pattern, where manual work is required, is shown in fig. 6.3. On the left side of **a)** you can see some blue marks where the algorithm found no spot and tried to interpolate. In the upper part of **a)** you see some double marks. Both are indications for manual post-treatment. Manual adjustment is simply possible by drag and drop with the computer mouse. Two variants are possible. In the case of existing but not recognized spots, it is recommended to use the "soft" adjustment with working sub pixel multistage centering algorithm discussed in chapter 5. While trying to move the mark with the left button of the computer mouse, you can simultaneously see where algorithm wants to place the mark when you will drop it. In some cases one spot is completely missing. Here it is necessary to use the "hard" adjustment, by using the left mouse button to place the mark where you think the spot should be. Although this adjustment is very subjective, this procedure is suitable to make spot patterns with bad quality processable.

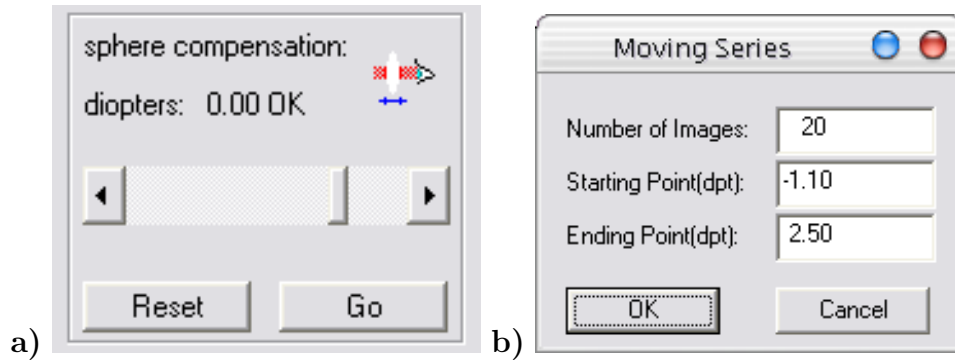


Figure 6.2: a) Sphere compensation module b) Dialog window for series with activated sphere compensation

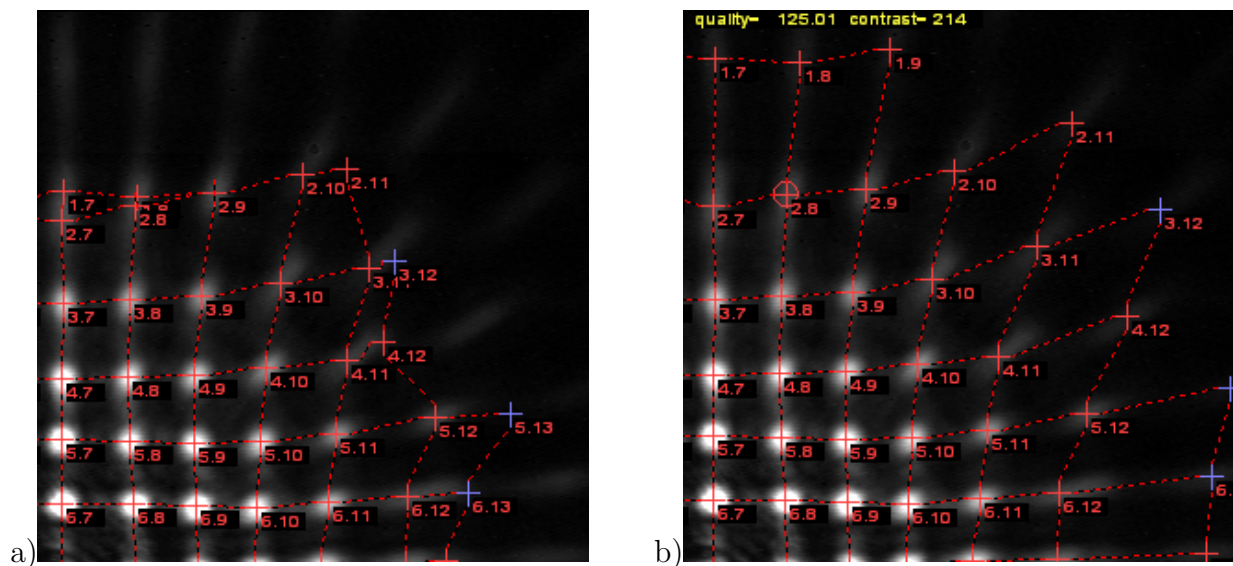


Figure 6.3: Example for a part of a spot pattern with high spherical aberration, where manual spot adjustment is necessary in HSS Analysis 2.x. For more detailed description see text.

After all spots were recognized, their positions are used to derive the wavefront parameters like Zernike coefficient using the algorithms described in chapter 5. The hardware parameters required for these calculations can be determined in the options dialog (see fig. 6.4).

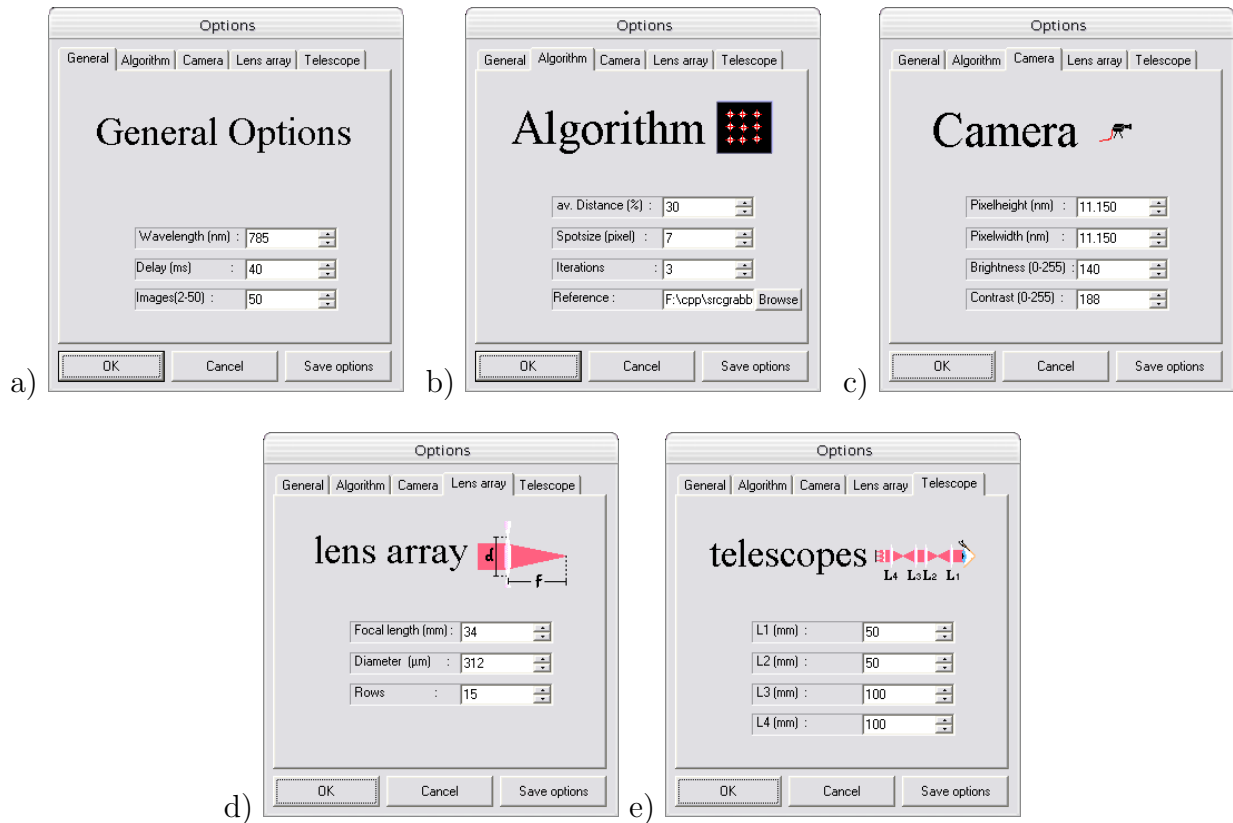


Figure 6.4: The options dialog of HSS Analysis 2.x

The third part of HSS Analysis is the result-module. Numerous representations of the results are possible. In the main result window (see fig. 6.5) the basic refraction numbers, a diopter map, a wavefront map and a 3d-view of the wavefront are displayed. The results of the mixed estimation of wave aberration discussed in chapter 5 can be displayed in the diopter grid window (see fig. 6.6). Furthermore, all the results taken from a single image or a complete series with 50 or more images can be exported to a file.



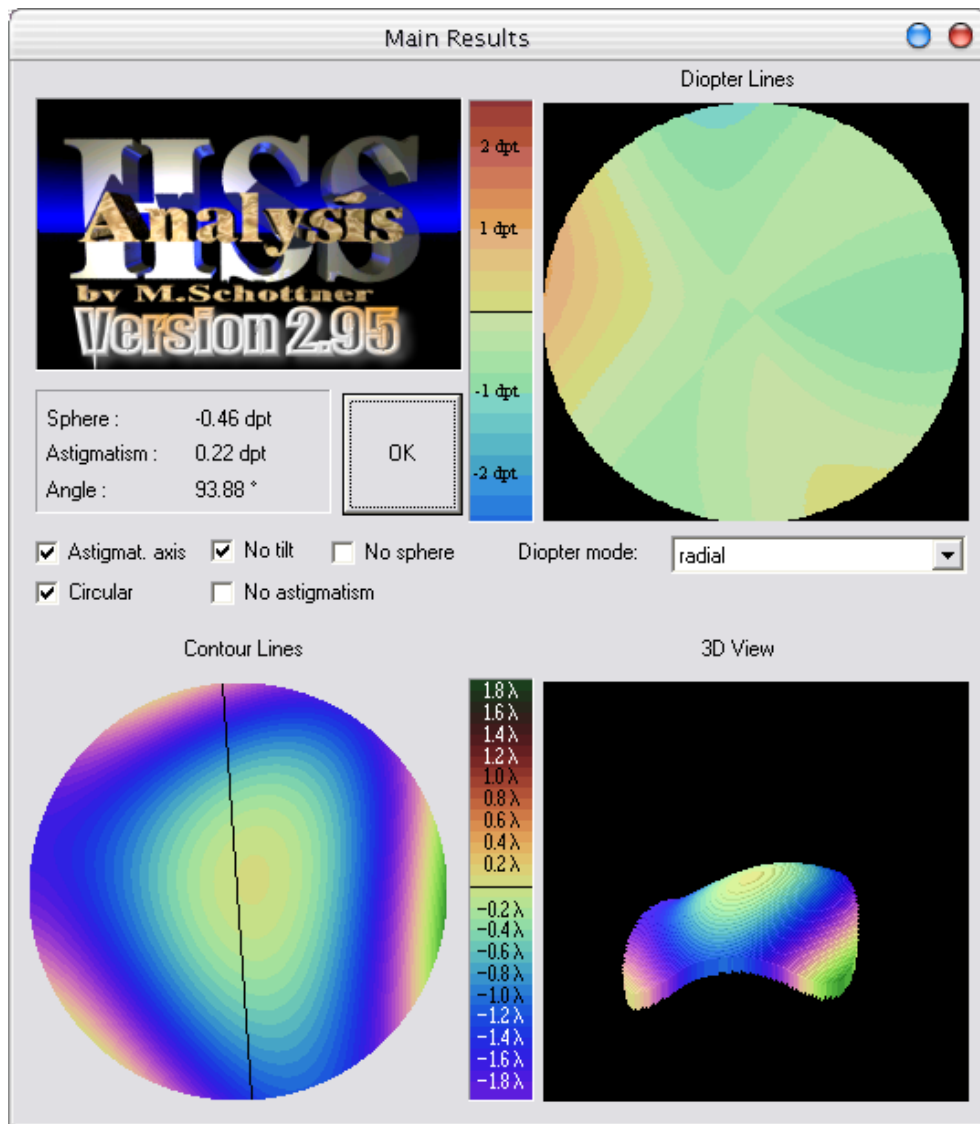


Figure 6.5: The main result window of HSS Analysis 2.x

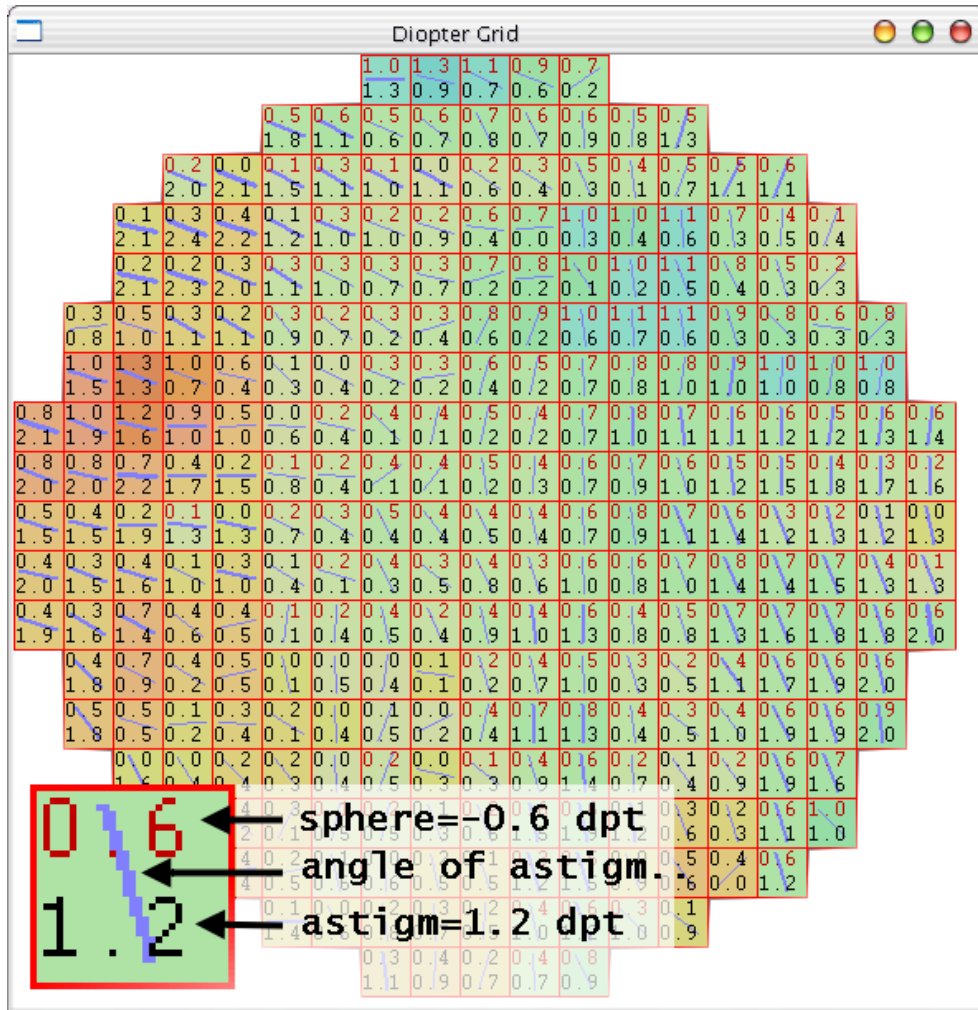


Figure 6.6: Diopter grid window used in HSS Analysis 2.x to display the results of the mixed estimation described in chapter 5. Every square represents the area of four subapertures. The upper number is the defocus within the square in diopter. Negative values are marked in red color. The lower number is the value of the astigmatism in diopters. The line in the center of each square represents the axis of the astigmatism within this square.

## 6.2 HSS Analysis 3.x

The latest versions of HSS Analysis are written with Borland C++ Builder 5.0 Professional. Since the older versions written with an incompatible development environment (Borland C++ Compiler 5.0), the whole user interface was developed again. Some new functions were added:

- The temporal evolution of every coefficient is shown in a table and a graph.
- Integration of support for Vfw (Video for Windows) enables the system to use almost every framegrabber, tv card or webcam to capture video data.
- Customized results can be exported to Excel.
- Limitations to the number of frames grabbed within a series are removed.

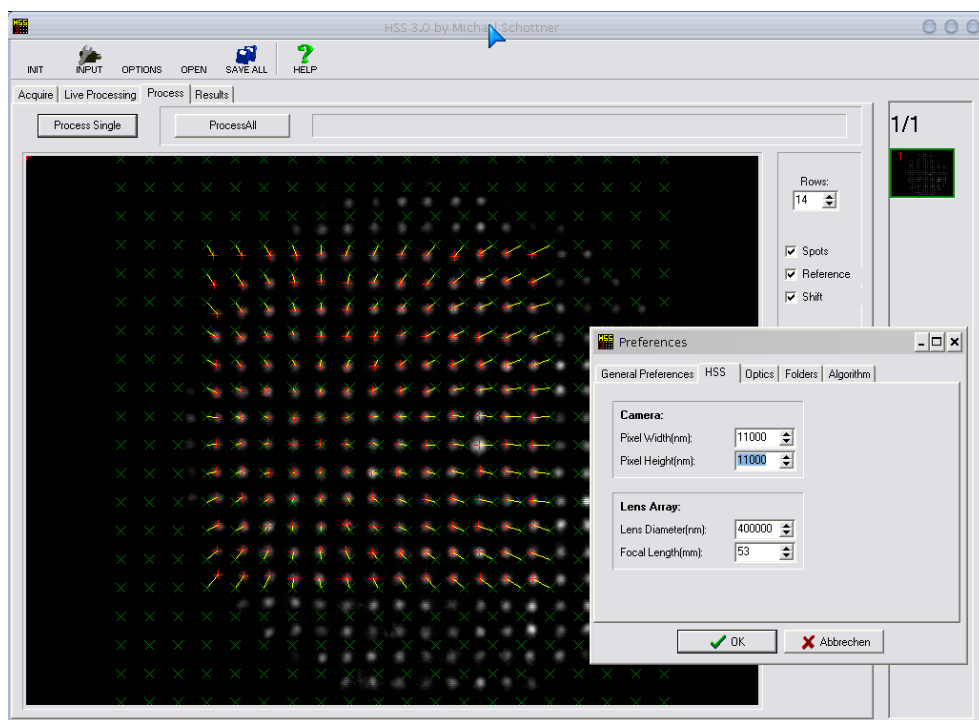


Figure 6.7: The main window of HSS Analysis 3.x

## 6.3 HSS Real 1.x

The program HSS Real 1.x is a version of HSS Analysis 3.x, that has been optimized for real time processing. Running on a 500 MHz pentium computer a maximum of 25 frames or 50 half frames can be captured and analyzed automatically. Complete analysis of spot patterns is not possible. The main application of this software is the real time display of histogram, spot shape, tilt, astigmatism and sphere. With this abilities, the program serves as a suitable tool for all kinds of alignment processes. Simultaneously the sphere and cylinder compensation can be controlled easily by scrollbars.

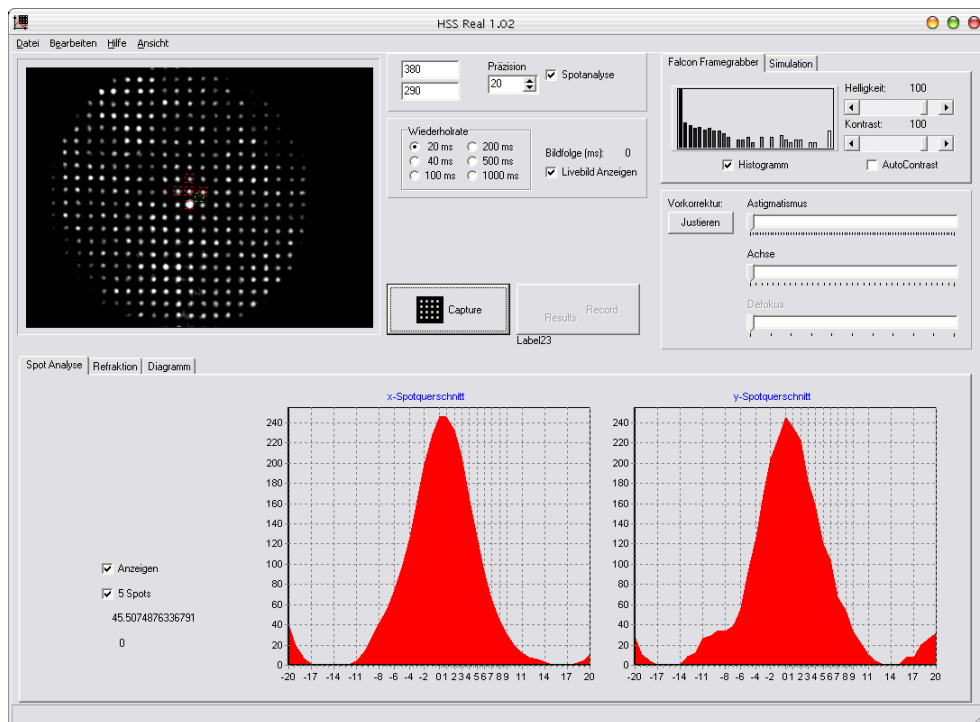


Figure 6.8: The main window of HSS Real 1.x. The lower diagrams show sectional views of a spot in x and y-direction. You can see that the lateral resolution in y-direction is only the resolution in x-direction. This is caused by the video signal that contains only the odd or the even line within 20 ms.

## 6.4 HSS Simulator 1.x

For the optimization of a program processing hss spot patterns, it is very useful to have a tool to prove the algorithms with all imaginable spot patterns. A program that generates hss spot patterns with the ability to simulate different wavefronts and sensor setups is not yet available. For this reason it was necessary to develop a new software system during this thesis.

As development tool Borland C++ Builder 5.0 Professional under Microsoft Windows was chosen. A screen shot of the final software is displayed in fig. 6.9. The main function of the software is the generation of bitmap files with spot patterns. A great number of parameters can be accessed. These parameters and their usage will be described in the following sections. Some important functions of this software are listed in appendix A.

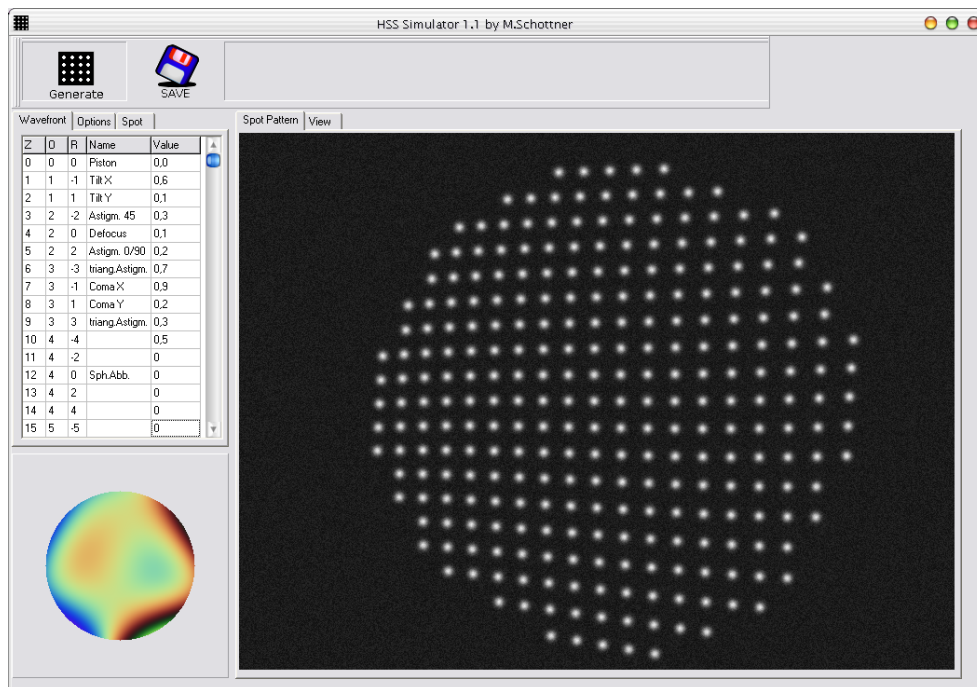


Figure 6.9: The user interface of the software HSS Simulator 1.x

### 6.4.1 General parameters

The main options dialog (see fig. 6.10a) enables the user to modify the fundamental hardware parameters. The first parameter is the size of the *diameter* of the subapertures of the lens array. It is equal to the distance between the centers of the subapertures. Different lens diameters directly cause different distances between the spots. The second value in the dialog is the *focal length* of the lens array. The result of a greater focal length

is an increasing magnification of wavefront distortions. In this simulation the focal length and the diameter of the sublenses have no influence on the spot size.

The third parameter is the *pixel size* of the ccd ship. Only square pixels are allowed. The number of the pixels is determined by the maximum size of the standard video signal (CCIR- 768×576) that is used by ccd camera and framegrabber and can't be changed. The pixel size is needed for the conversions from computer pixel distances into real distances that are calculated in micrometers. These three parameters should not be changed after a specific hardware design has been chosen.

Additional parameters are the *shape* of the beam, that could be circular or square, and the *number of rows* and columns of the used subapertures. This number is also responsible for the size of the unit circle, that is used for generating distorted wavefronts with Zernike coefficient as it is shown in the next section.

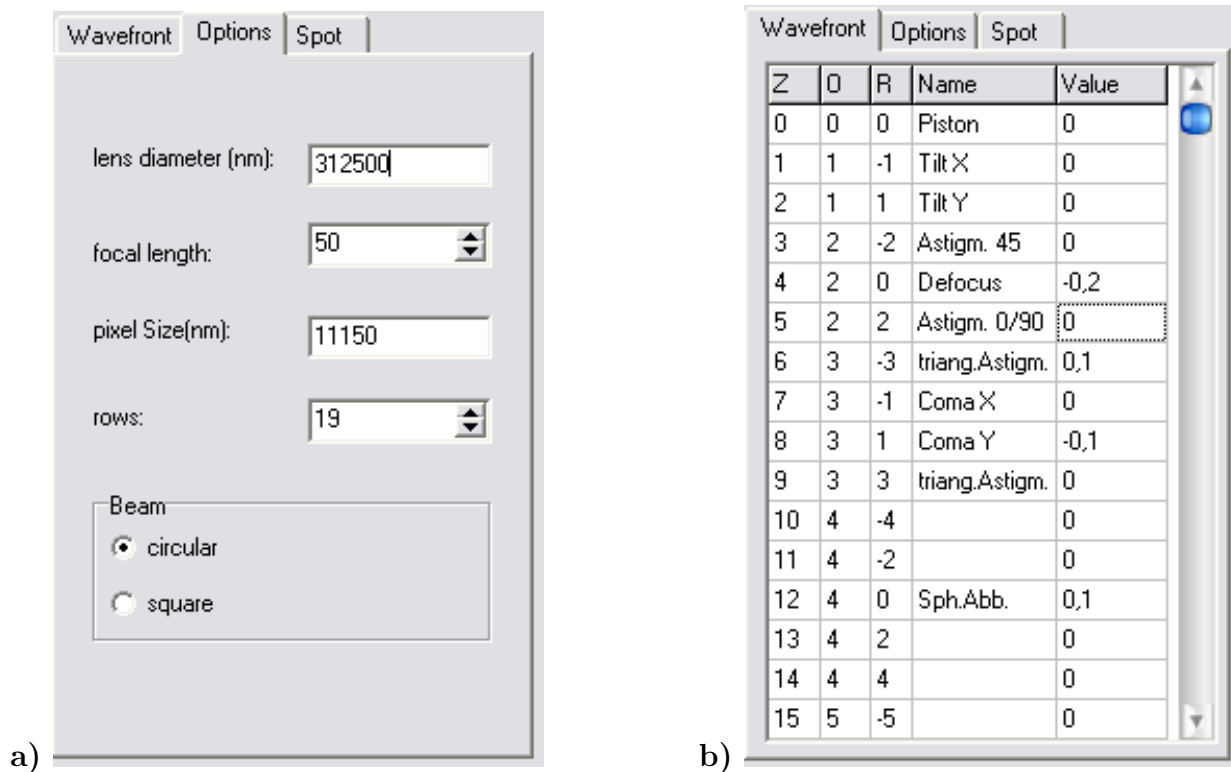


Figure 6.10: a) General Parameters of HSS Simulator 1.x b) Table with the Zernike coefficients up to 10th order ( $Z_{65}$ ) that are used for the spot pattern generation in HSS Simulator 1.x

## 6.4.2 Generating wavefronts

The most interesting opportunity of the HSS Simulator is the possibility to simulate spot patterns which correspond to any wavefront (see fig. 6.10b). Opticians usually describe wavefronts with Zernike polynomials (see previous chapter and appendix). This software allows to use Zernike polynomials up to 10th order ( $Z_{65}$ ). All polynomials are normalized to the unit circle. Since the coefficients are very small, the values in the 5th column are multiplied with  $\frac{1}{1000}$ . The algorithm for the calculation of the spot positions is based on simple differentiation and is completely listed in the appendix.

## 6.4.3 Spot shapes

For individual situations, different spot shapes were needed, so there is the possibility to generate spots with all kind of shapes.

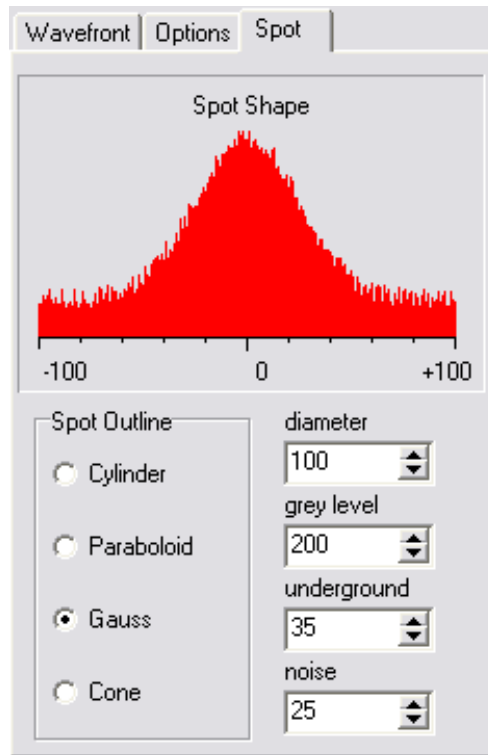


Figure 6.11: Spot shape dialog in HSS Simulator 1.x

### Cylinder-shape spots

The simplest shape is the cylinder shape. It can be recognized by a gray level of zero outside of a circle and an equal maximum gray level inside. An example of simulated

cylinder shape spots are shown in fig. 6.12. A similar kind of spot shape will appear if the

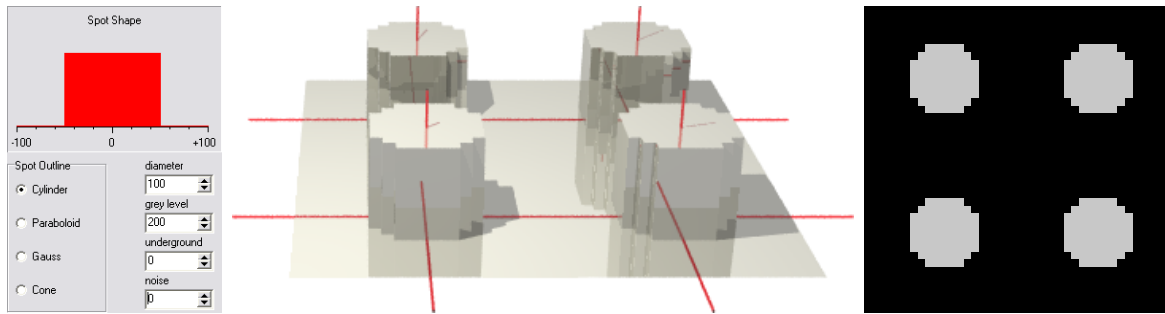


Figure 6.12: Simulated cylinder shape spot pattern

ccd camera or the framegrabber achieves a level of saturation.

### Parabolic-shape spots

The second possible shape is the parabolic shape. It can be recognized by a gray level that decreases with  $r_{max}^2 - r^2$  to zero at an radius of  $r_{max}$ . An example of this kind of spot shape is shown in fig. 6.13 Similar spot shapes will appear if the black level of the camera

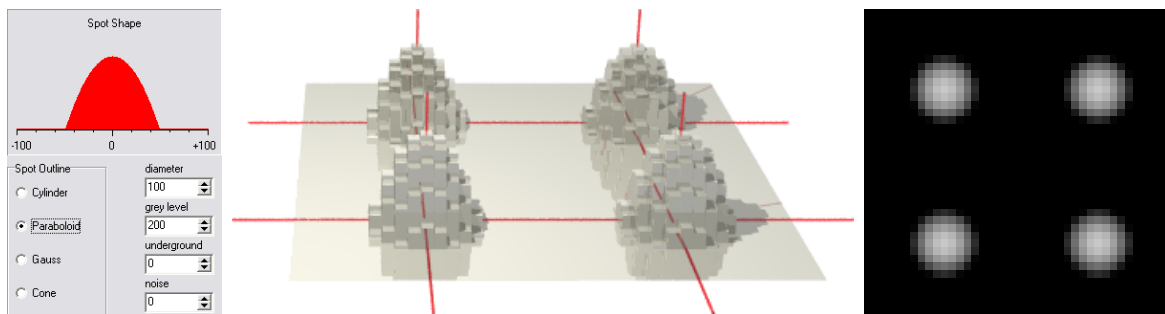


Figure 6.13: Simulated parabel shape spot pattern

or the framegrabber is very high.

### Gauss shape

The third and most important shape is the Gauss shape. In this case the gray value decreases with a function like:

$$G = G_{max} * \exp\left(\frac{1}{r_{spot}^2}\right) \quad (6.1)$$

An example of this kind of spot shape is shown in fig. 6.14. If everything in the optical setup is well adjusted, all measured spot patterns should have spots with a Gauss shape.



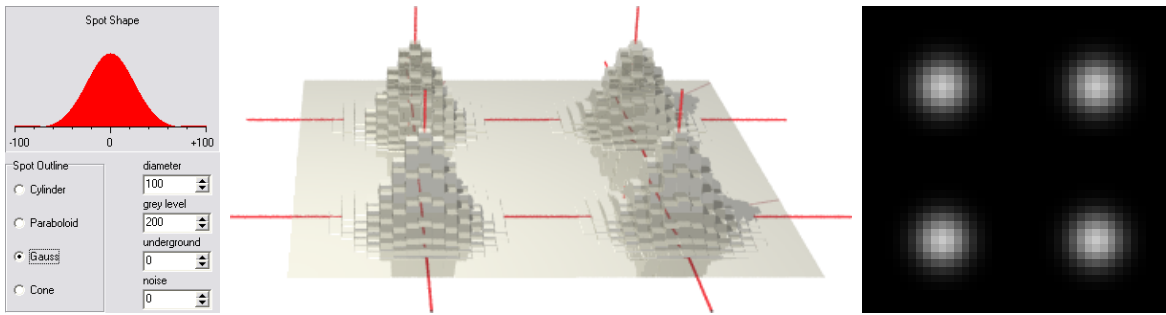


Figure 6.14: Simulated gauss shape spot pattern

### Cone shape

The last shape is the cone shape. An example of this shape can be seen in fig. 6.15. This spot shape is included in the software only for test purposes. There is no analogy in real spot patterns.

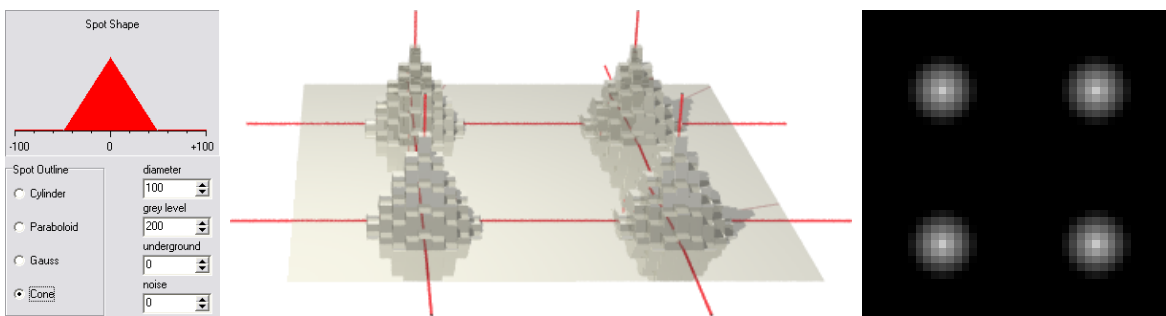


Figure 6.15: Simulated cone shape spot pattern

### 6.4.4 Additional pattern modifications

Two additional modifications can be done with the simulated spot patterns. The first possibility is the addition of a *constant underground*. Its level can be positive or negative. The second modification is a variable *noise*.

### 6.4.5 Output

The output of all calculations is a grayscale bitmap. This bitmap can be saved as an uncompressed bmp-file (Windows BitMap, about 400 kB) or as a loss-free compressed png-file (Portable Network Graphic, about 10-200 kB).

Two additional visualizations of the wavefront are possible: a color coded map of the path differences (see fig. 6.16a) and a color coded 3d-view (see fig. 6.16b).

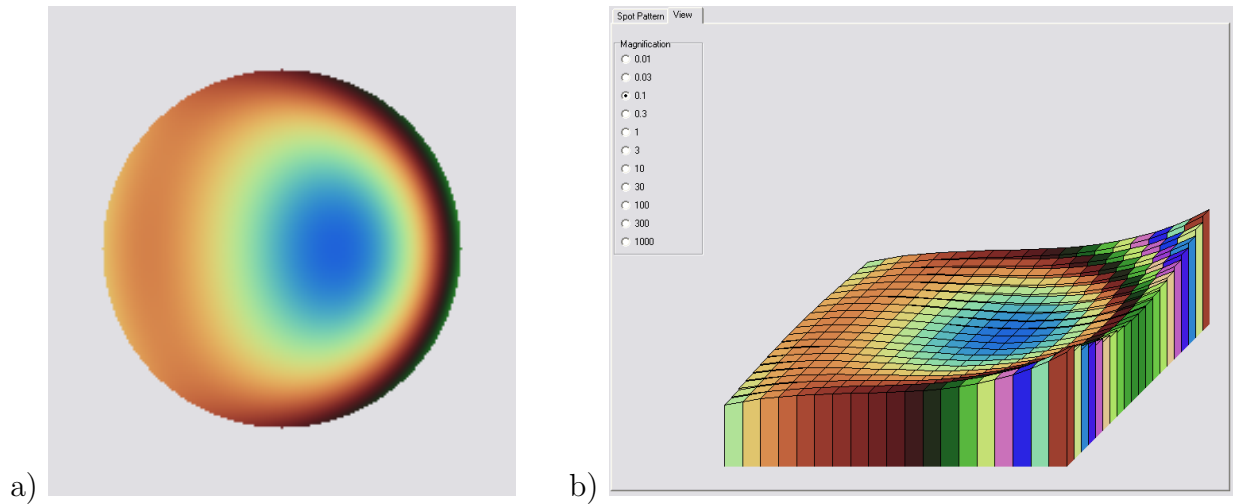


Figure 6.16: Wavefront output in HSS Simulator a) color coded map of optical path differences b) color coded 3d-view of the wavefront

### 6.4.6 Effects of wavefront distortions

This software tool can be used to simulate effects of Zernike-based wavefront distortions on different wavefronts by the modification of some parameters. Some examples of possible applications of this feature are shown in figures 6.17. All examples use the same parameters shown in table 6.1.

lens diameter	20000 nm	spot shape	Gauss
pixel size	10000 nm	spot diameter	200 $\mu m$
rows	40	gray level	5
focal length	98	underground	0
beam shape	circular	noise	0

Table 6.1: General parameters used for the examples in fig. 6.17

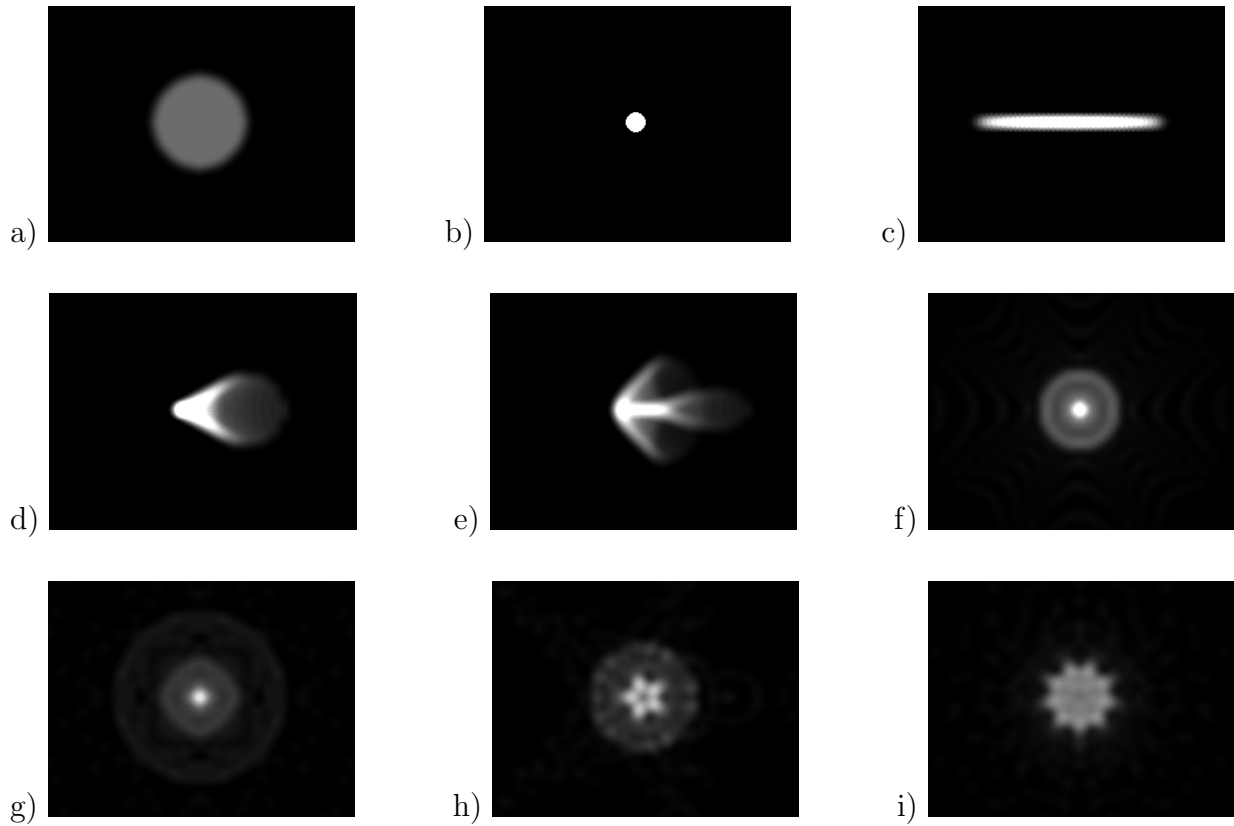


Figure 6.17: **a)** All Zernike coefficients are zero: a plain wavefront **b)** Negative defocus ( $Z_4=-1$ ): a sharp focus point **c)** Astigmatism ( $Z_5=-2$ ): sharp image in one axis and divergent in the other axis **d)** Negative defocus ( $Z_4=-1$ ) with coma ( $Z_7=1$ ): simple coma **e)** Coma ( $Z_7=1$ ) with astigmatism ( $Z_5=1$ ): a comet **f)** Spherical aberration ( $Z_{12}$ ) **g)** Higher order spherical aberration ( $Z_{24}$ ) **h)** 7th-order distortion with azimuthal frequency of 5 ( $Z_{29}$ ) **i)** 9th-order distortion ( $Z_{45}$ )

# Chapter 7

## Simulations with the algorithms

For the optimization of the spot pattern analysis, numerous simulations have been done. The quality of an algorithm can be described by the reliability, the limitations and the speed. Incidentally, these examination are suitable to gather information about the look of perfect processable spot patterns.

### 7.1 Spot finding algorithm

The reliability of the spot finding algorithm depends on the ability to manage difficult situations with noise, underground and different spot shapes and sizes.

The procedure for the simulations in this section is always the same: A spot pattern with a defocus of 1/1000 is created with HSS Simulator and analyzed with HSS Analysis. In the ideal case, the result should be a defocus of exact 1/1000. The basic parameters used for all simulations in the following sections are shown in table 7.1. The influence of the additional parameters on the result was observed.

$Z_0 - Z_3$	0
$Z_4$ (defocus)	0.001
$Z_5 - Z_{65}$	0
sub lens diameter	312 $\mu\text{m}$
pixel size	11.15 $\mu\text{m}$
rows	10
focal length	34 mm
beam shape	circular

Table 7.1: Parameters of HSS Simulator used for the following simulations

### 7.1.1 Underground

The first examination was the influence of the underground level on the result. In fig. 7.1 you can see, that the amount of underground intensity doesn't affect the precision of the algorithm but affect the required number of iterations of the spot centering. If the underground level is zero, the maximum accuracy is achieved after the first iteration. This shows, that a low underground level is necessary for a fast processing.

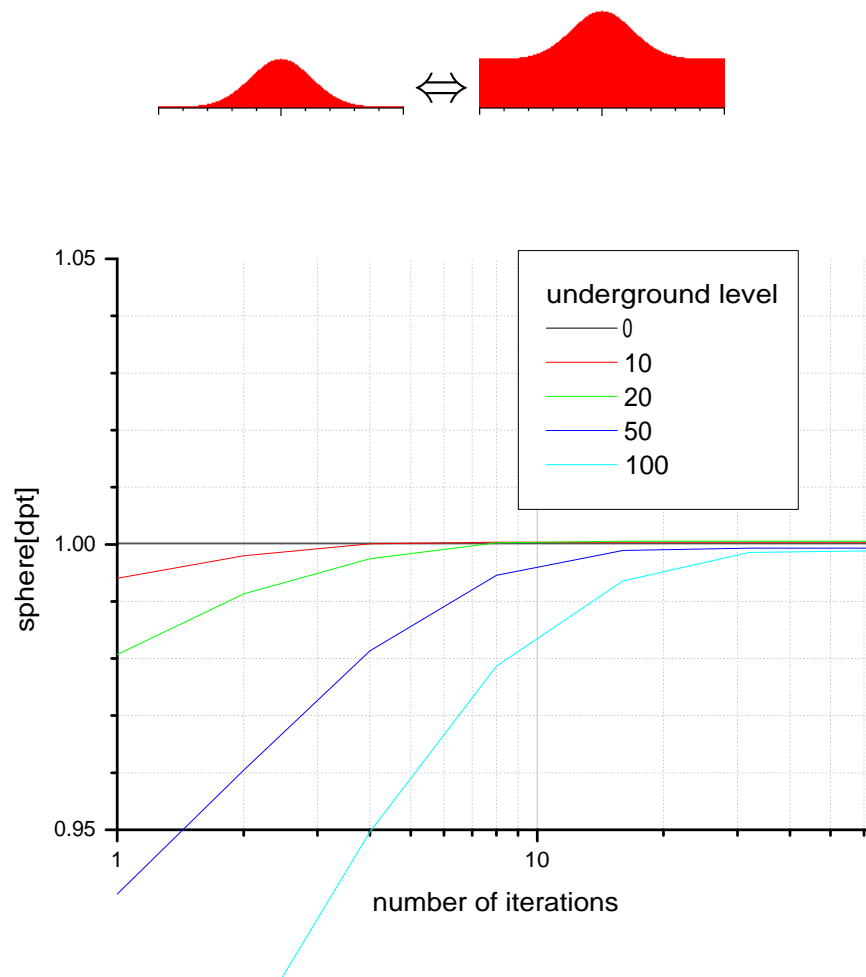


Figure 7.1: Effect of the underground level on the spot finding process. The different curves correspond to different underground gray values relative to the intensity of the spot signal

### 7.1.2 Noise

All spot patterns created by real measurements contain a certain level of noise. It is obvious, that the results will get worse when the noise level is increasing. In figure 7.2 you can see that a noise level greater than 20% strongly affects the accuracy of the algorithm. Similar as in the previous section, the required number of iterations increases with noise level, too. In non-simulated spot patterns the effect of noise can be much greater, if the intensity of the spots varies.

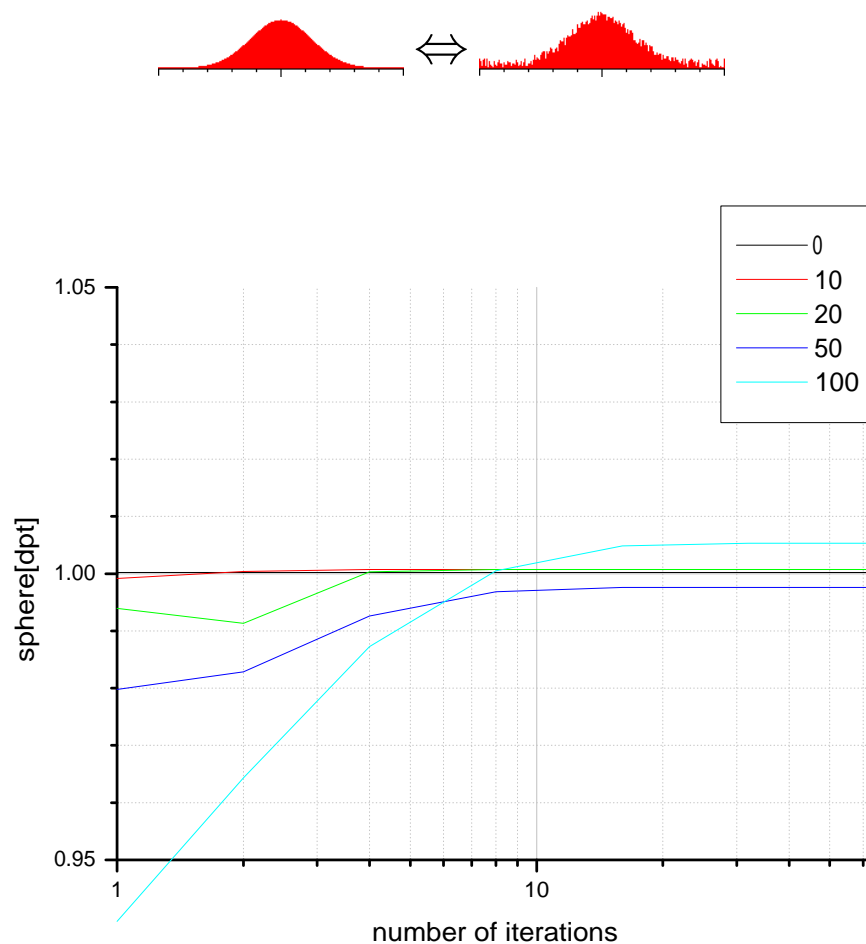


Figure 7.2: Effect of the noise level on the spot finding process. The different curves correspond to different noise gray levels relative to the intensity of the spot signal

### 7.1.3 Spot size

The size of the spots is another parameter with effect on the spot finding process. An aberrated wavefront will produce spots, that are bigger than a plain wavefront will do. In figure 7.3 you can see, that more usable pixels in every spot will lead to faster and better results. This effect is more important for noisy patterns, but since bigger spots contain more information, the effect also exists in noiseless patterns. Nevertheless, big spots are not preferred, if their intensity decreases strongly.

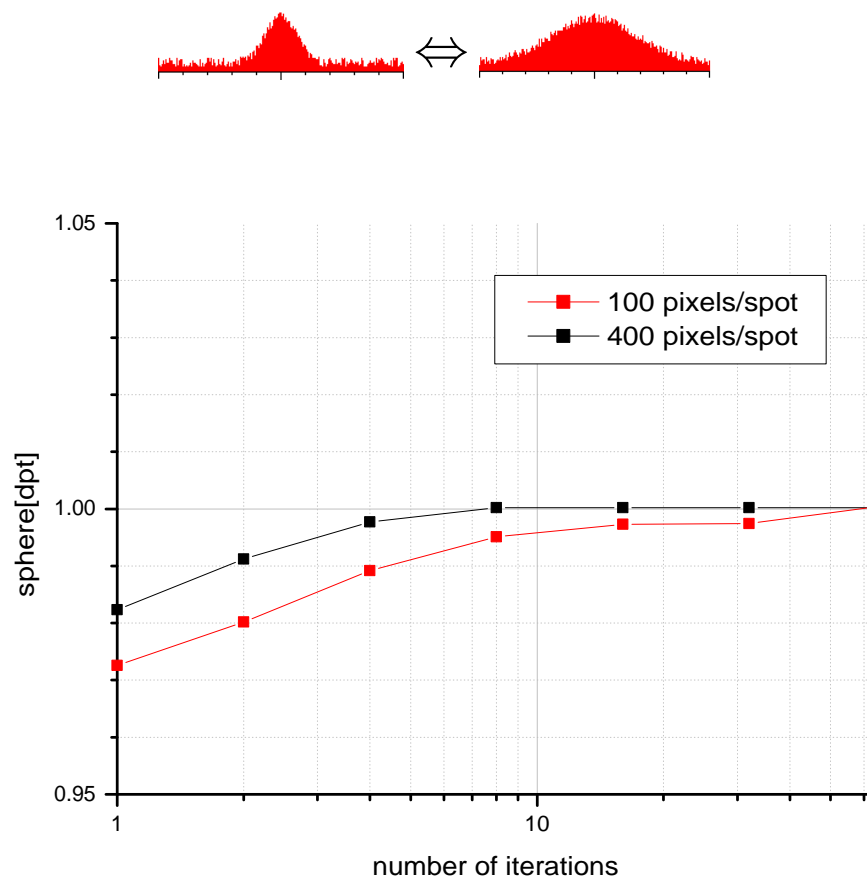


Figure 7.3: Effect of different spot sizes on the spot finding process.

### 7.1.4 Spot shape

Different spot shapes can appear, if the sensitivity of the camera is not well adjusted (see chapter 5). The desired shape is a gauss shape, that is the result of diffraction limitation at the sub lenses. Saturation modifies this shape to a cylinder-like shape, low sensitivity to a parabola-like shape. The effect of this shape modifications and a cone-like shape is shown in fig. 7.4. A cylinder shape accelerates the process, but leads to bad results because of the loss of information in the middle of the spots. A pattern with cone-shaped spots requires more iterations and is processable with a similar accuracy, because only a view pixel have a high intensity. The Gauss shape and the parabola shape lead both to similar, good results. The Gauss shape has a little advantage because of a the extra information in the external field.

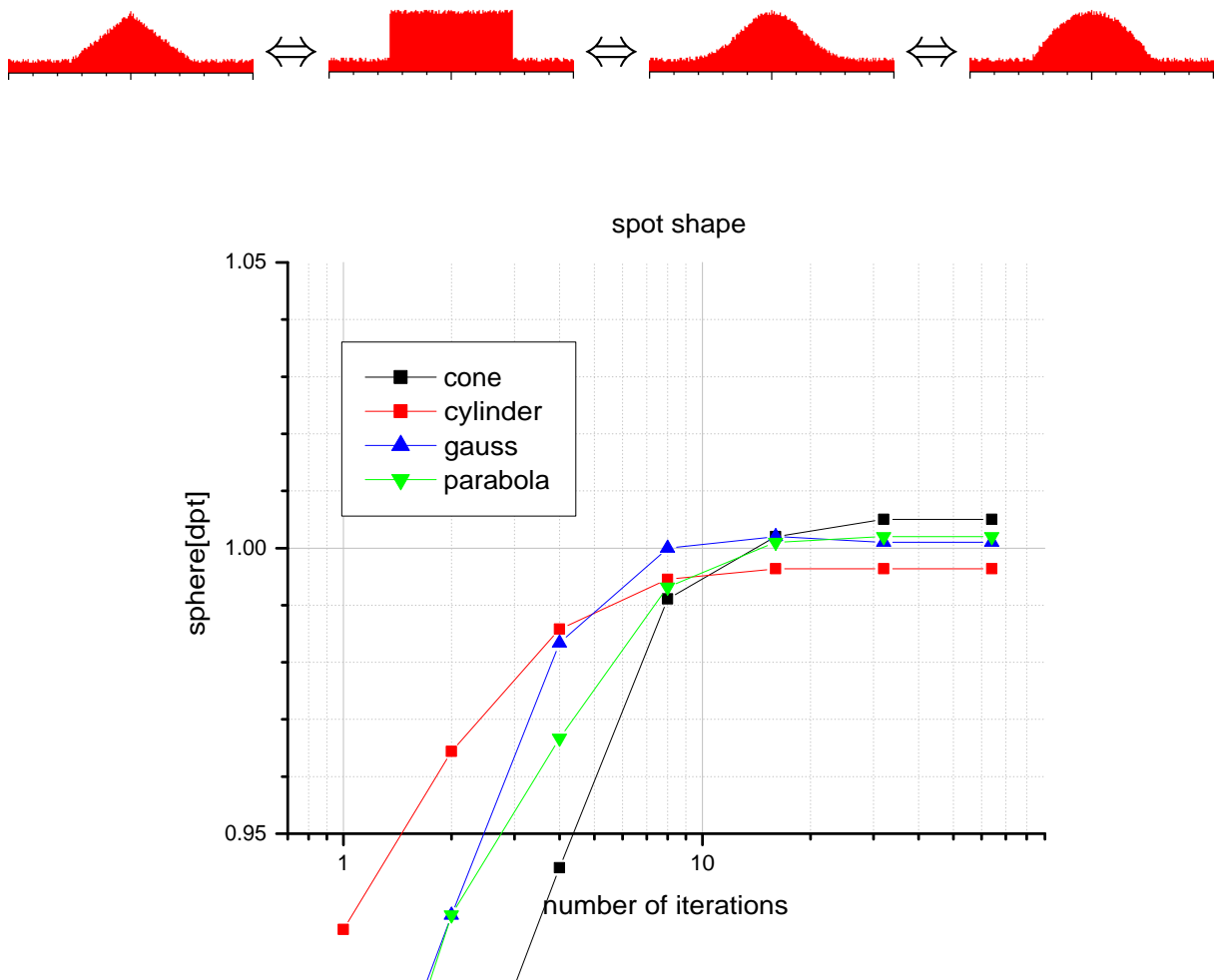


Figure 7.4: Effect of different spot shapes on the spot finding process.



## 7.2 Limits

The automatic analysis of spot patterns is limited even if the spots have the best quality. Patterns with extremely high aberrations represent great problems to the algorithm. The optimizations of the spot finding process described in chapter 5 have strongly extended the limits of the algorithm. The maximum aberrations have been determined by increasing of the corresponding parameters until the automatic spot finding algorithm had problems with the correct assignment. These maximum values are a sphere of  $-2.5 \cdot 10^{-3}$  to  $7.5 \cdot 10^{-3}$  (-7 dpt to 21 dpt), an astigmatism at  $0^\circ/90^\circ$  of  $2.5 \cdot 10^{-3}$  (-7 dpt), an astigmatism at  $45^\circ$  of  $5 \cdot 10^{-3}$  (14 dpt), a coma of  $0.8 \cdot 10^{-3}$  (11 dpt) and a spherical aberration of  $-0.2 \cdot 10^{-3}$  to  $0.65 \cdot 10^{-3}$  (-8 to 27 dpt). The spot patterns corresponding to these values are shown in fig. 7.5. If the aberrations exceed these limits, manual spot assignment with use of the software centering algorithm is still possible as long as spots are recognizable by the eye.

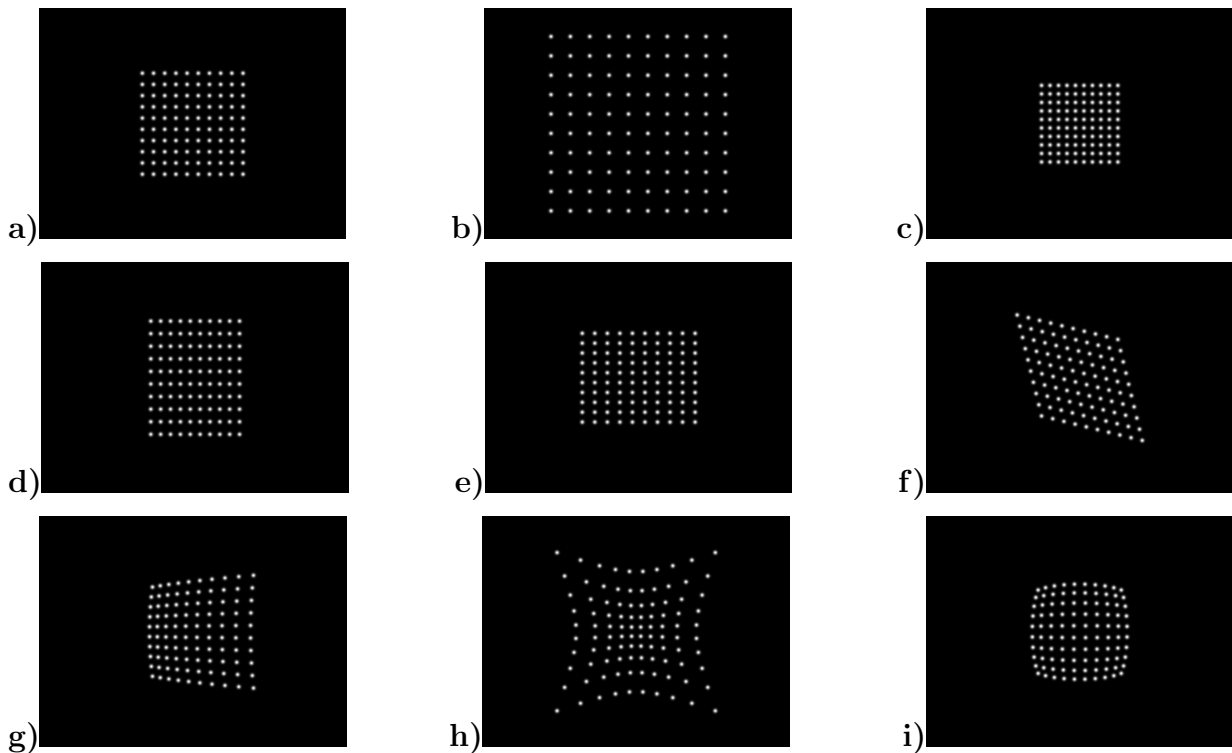


Figure 7.5: Processable spot patterns with maximum aberrations: **a)** original wavefront **b)** positive sphere **c)** negative sphere **d)e)f)** astigmatism with  $0^\circ/90^\circ/45^\circ$  **g)** coma **h)** negative sph. aberration **i)** positive sph. aberration

## 7.3 Speed optimization

Especially for real-time applications, but also for post-processing of long time series, a fast analysis is desired. The following considerations concern the influence of internal and external parameters on the time, that is required for the whole analyzing process.

If you want to find the time-critical part, a closer look to the things, that happens during the process is necessary. The first thing that happens is the initialization of the processing module. After this, the image data can be taken from the system memory or the frame grabber memory. The following steps are the spot finding, the calculation of the gradients and the wavefront estimation. The duration of every step for a typical analyzing process is shown in fig. 7.6.

It is obvious, that the only time-critical process is the spot finding algorithm. The duration of the calculations of the gradients (0.04 ms) and the wavefront estimation (0.05 ms) can be neglected. The 2 ms image acquisition time depends on the speed of the hardware and can't be reduced by software. Therefore, the following considerations concentrate on the spot finding algorithm.

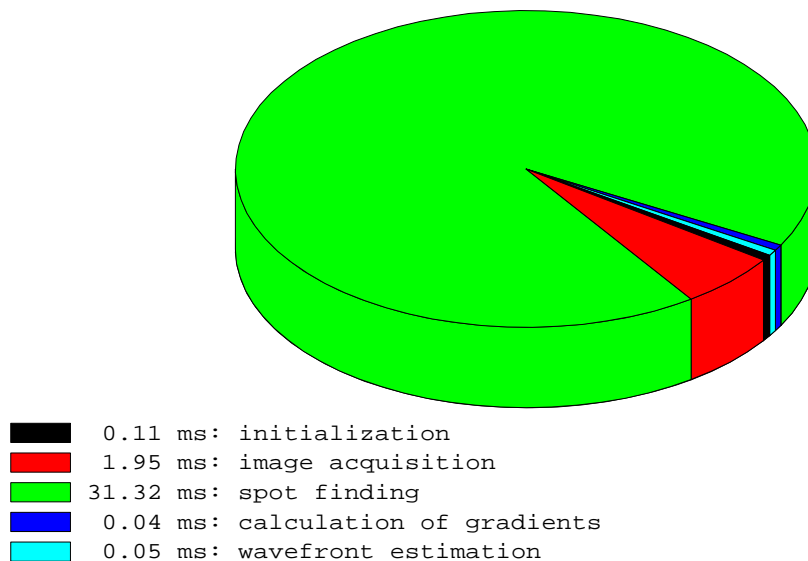


Figure 7.6: Duration of the single modules of the analyzing process with HSS Analysis software running on a 1200 MHz AMD Athlon with Windows XP Professional.

The first and most obvious thing when trying to decrease the time required for the spot finding, is to reduce the number of spots to process. The effect of an decreasing number of processed rows is shown in fig. 7.7. The curve looks like a parabola with an offset of about 4 ms. Since reducing the number of spots lead to a loss of information, it is only advisable if only a part of the wavefront should be analyzed and no high precision is required.

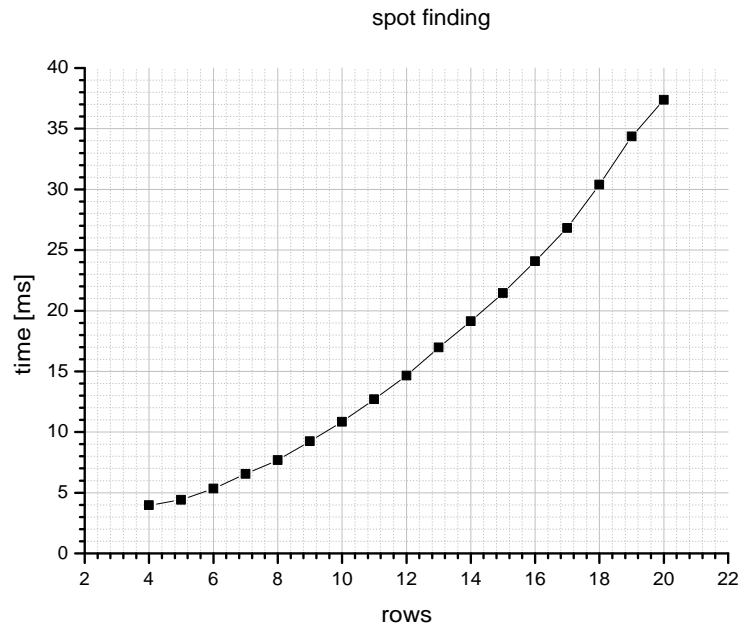


Figure 7.7: Effect of the number of processed images on the time that is required for the spot finding process.

The second possibility to accelerate the spot finding process, is to decrease the number of pixels used for the centering of each spot and the number of iterations. The influence of these two parameters is shown in fig. 7.8. If the size of the spots is smaller in any case, decreasing the number of pixels used for the spot centering is possible without loss of information. Further decreasing in small steps is only advisable, if the quality of the spots is good. A smaller number of iterations doesn't affect the result, if the noise and underground level is small (see previous section). A pattern with almost no underground can be still processed optimally with down to 5 iterations.

The time required for the wavefront estimation depends on the number of rows and columns of used spots, too. Although the duration of this process is very small, an influence of the number of spots is visible in fig. 7.9. It is particularly the effect of the orthogonalization of the polynomials (see chapter 5). Since these calculations are required only once for each number of spots, it would be possible to store the results of the orthogonalization and reuse them later.

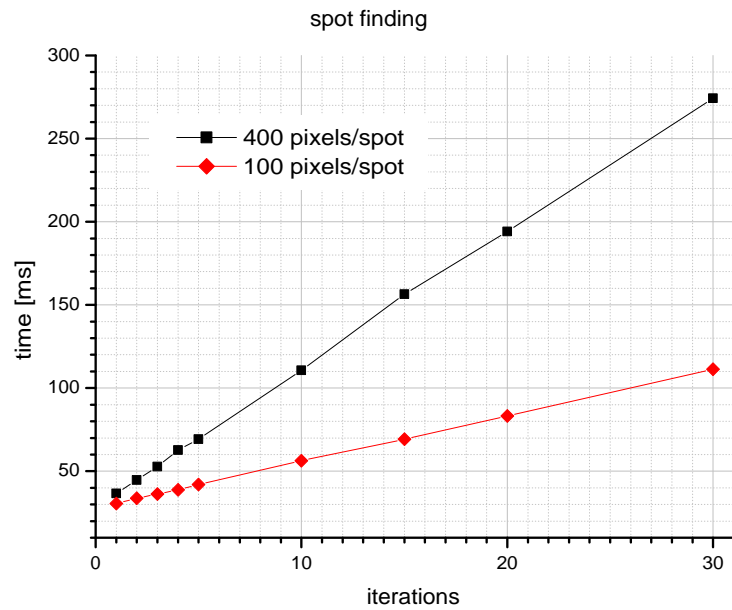


Figure 7.8: Influence of the number of iterations on the spot finding time for two different numbers of pixels per spot

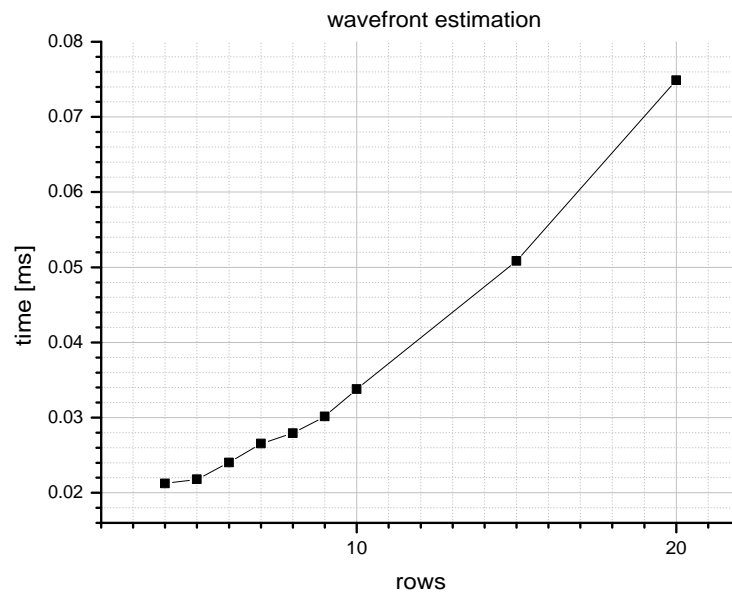


Figure 7.9: Time required for the modal estimation of the wavefront

# Chapter 8

## Experiments with the wavefront sensor

### 8.1 Artificial eye

Since every real system still has small aberrations, the wavefront sensor requires a method to measure these aberrations. The wavefront from a ‘perfect’ artificial eye is suitable to deliver this information. Once you have this information, it is possible to subtract the aberrations of the system from all future measurements. An example for results from an artificial eye is shown in fig. 8.1. The wavefront is almost plain, only a very small spherical aberration can be seen in fig. 8.1b.

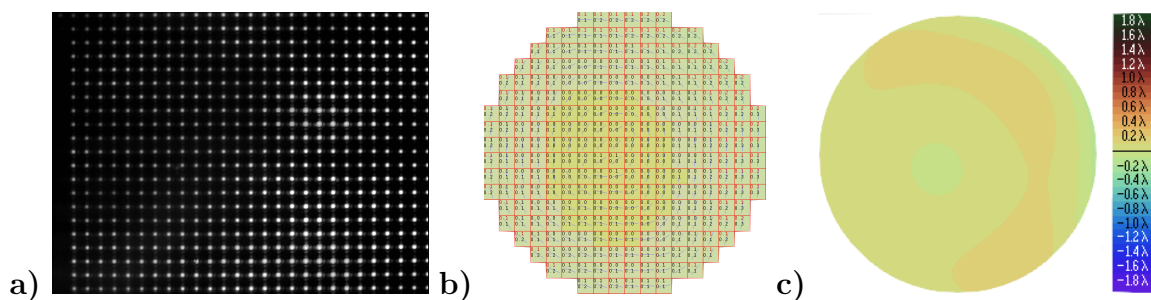


Figure 8.1: a) Reference pattern b) diopter grid c) height map

## 8.2 Selected patients

In this section the results of measurements at four characteristic eyes from four patients are introduced. Except for the first example, there are special properties of the eyes, that mean difficulties for the measurement and analysis.

### 8.2.1 Example 1

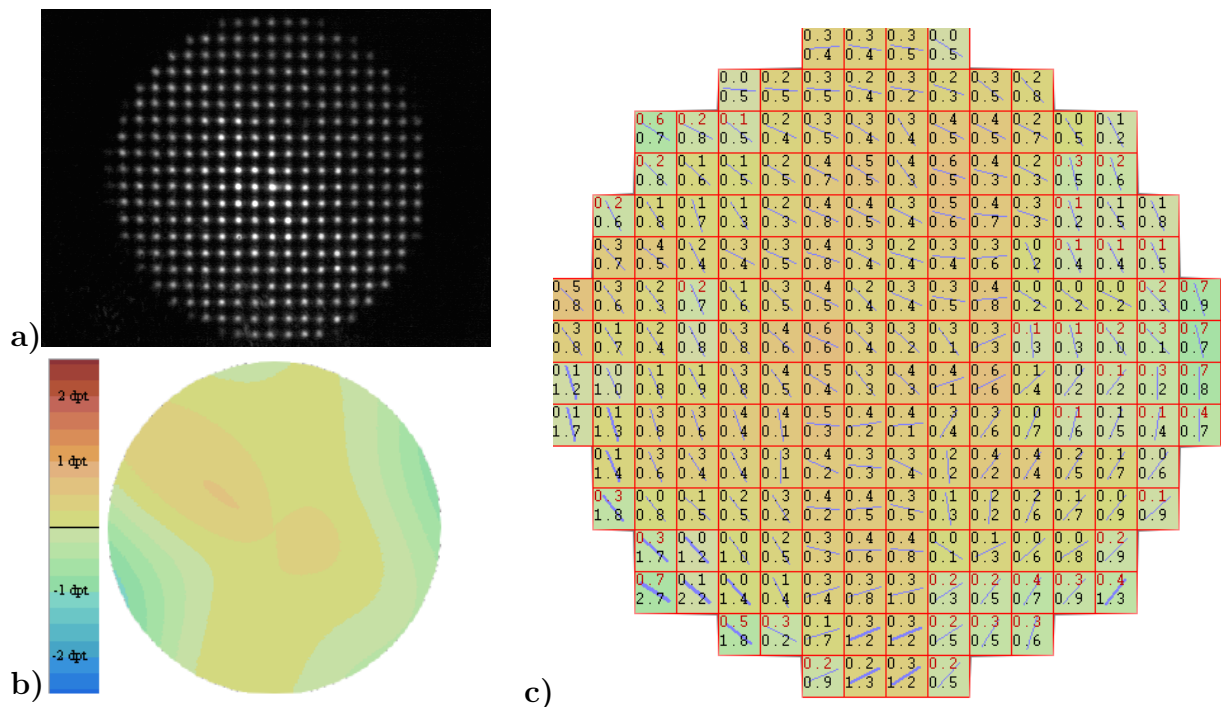


Figure 8.2: Patient 1: a) spot pattern b) modal diopter map c) diopter grid

The first eye is an almost perfect eye (patient bs, left eye). No precompensation is needed. The pupil diameter is 6.5 mm. All spots are visible (fig. 8.2a). Eyes like this one doesn't mean any problem to the system. The measured sphere is 0.2dpt, the astigmatism 0.2dpt and its angle is  $142^\circ$ . In fig. 8.2c you can see, that the power decreases in the periphery. This means, that the small farsightedness decreases for larger pupils. The measured spherical aberration is  $0.02 \cdot 10^{-3}$  ( $\approx 60$  nm). The results from the modal wavefront estimation (see fig. 8.2b) are very similar to the diopter grid in fig. 8.2c, that is the result of the interpretation of every 4 neighboring lenses of the lens array as a single wavefront sensor (see chapter 5).

## 8.2.2 Example 2

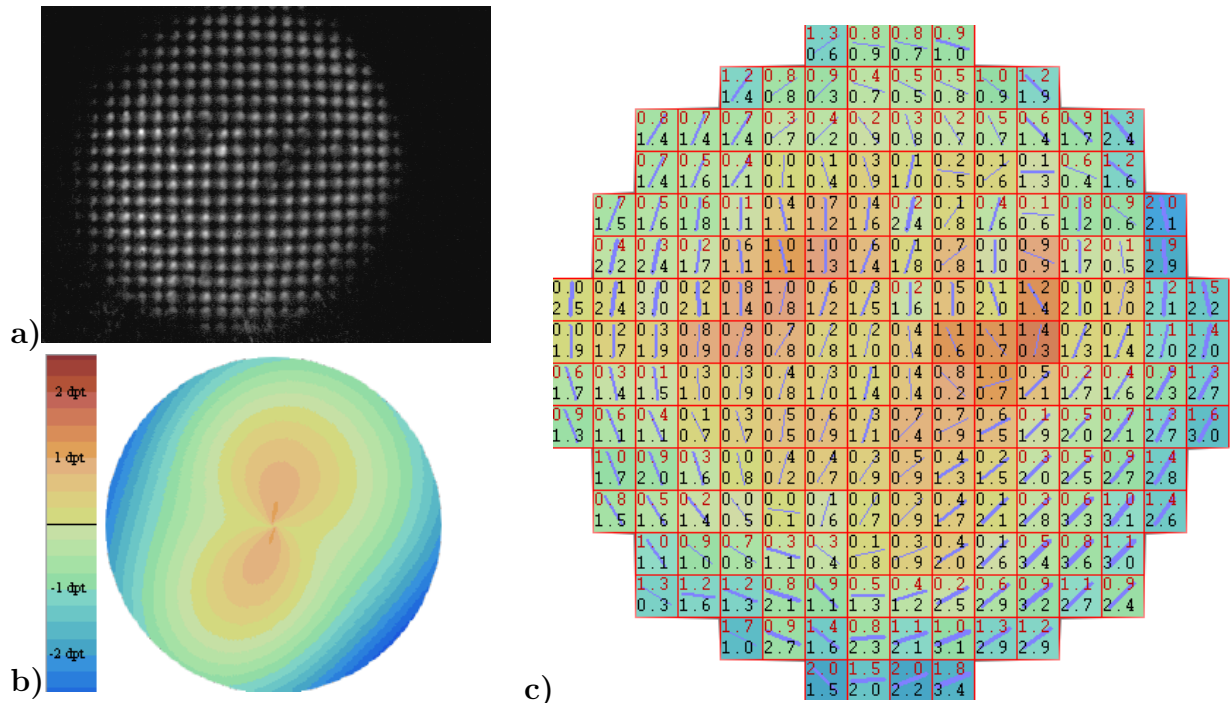


Figure 8.3: Patient 2: a) spot pattern b) modal diopter map c) diopter grid

The second example shows a post-lasik eye (patient nn, left eye). The pupil diameter is 6.5 mm. The spot quality is not as good as in the previous example, but this does not affect the accuracy of the results (see chapter 7). The two dark areas in the center might be the result of something on the cornea (fig. 8.3a) and can be seen in the diopter grid, too (fig. 8.3c). The modal estimation in fig. 8.3 is not suitable to show these elements, since the modal wavefront estimation only uses polynomials up to 6. order. Both figures show a strong spherical aberration. The measured value is  $0.15 \cdot 10^{-3}$  ( $\approx 450$  nm).





## 8.2.4 Example 4

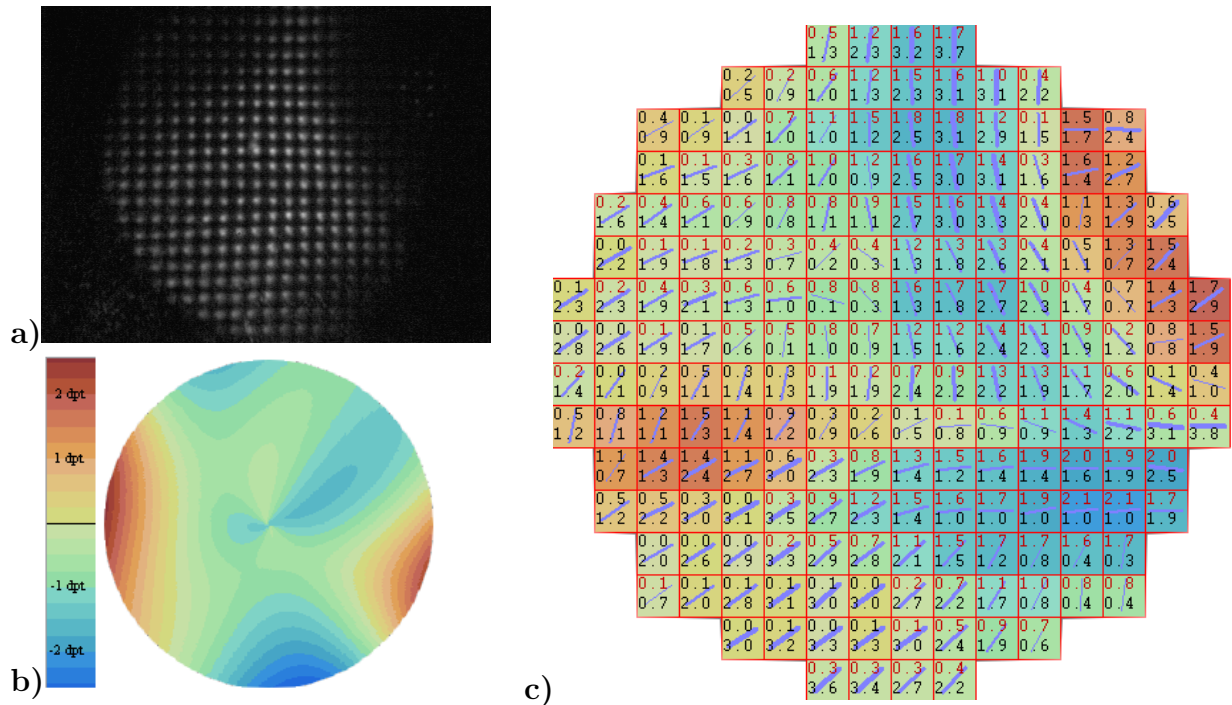


Figure 8.5: Patient 1: a) spot pattern b) modal diopter map c) diopter grid

The last example is an eye with a large scar on the cornea (patient rf, left eye). In the spot pattern in fig. 8.5, the spots in the upper right area seem to be missing, but they are only darker. This is a result of an accident, that leaved a large scar on the cornea. The structure of the scar can be seen well in fig. 8.5c. The left part of the eye is almost aberration-free. A small red area in the left could be another defect. The modal diopter map in fig. 8.5 shows, that the algorithm of the modal estimation has problems with this eye. Strong asymmetric aberrations, as they exist in this eye, are not suitable to be described with 6.order-polynomials.

## 8.3 Time series

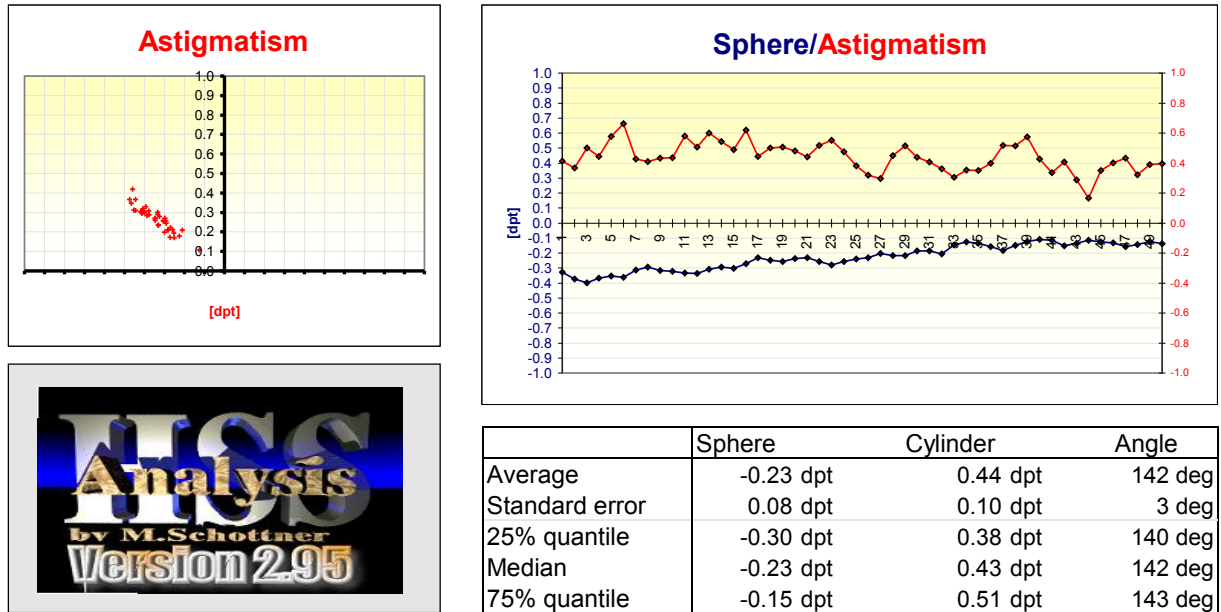


Figure 8.6: Example for a time series with 50 measurements within 5 seconds

Since a measurement with the wavefront sensor only takes as long as the camera needs to take an image, time series are possible. An example for a series consisting of 50 measurements is shown in fig. 8.6. The time delay between two measurements is 100 ms. The overall time 5 seconds. Apart from a small drift of the accommodation (about 0.2 dpt), the sphere is almost constant. The astigmatism has more variation, its standard error is 0.1 dpt. Although the size of the astigmatism changes, its angle is almost constant and has a value of  $142^\circ \pm 3^\circ$ .

The software is able to take up to 25 images a second. With a reduction of the vertical resolution, 50 images are possible. The duration of on series is only limited by the available space on the computers harddrive. Full real-time processing of the image data is not possible with current computers, but a basic analysis is possible in real-time.

## 8.4 Spherical aberration

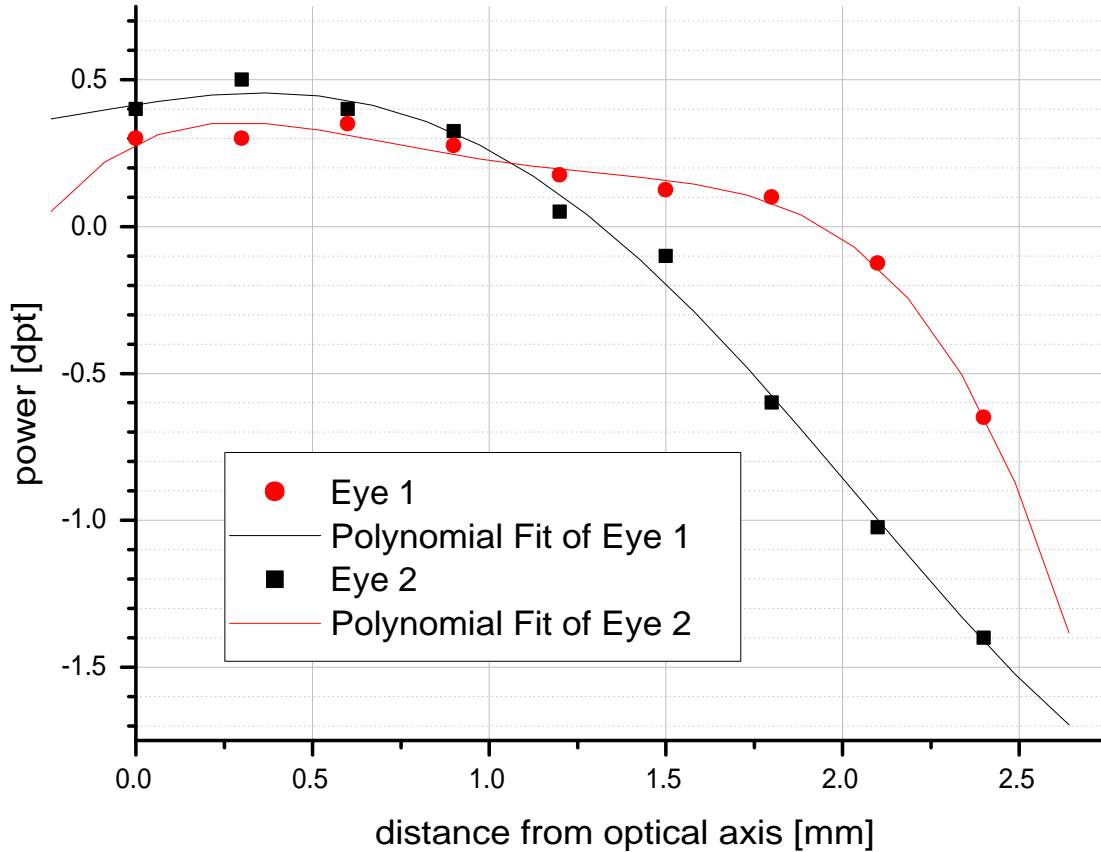


Figure 8.7: Influence of the distance from the optical axis to the optical power of an two eyes

The data from the diopter grid (see chapter 5: mixed estimation), can be used to show the influence of the distance from the optical axis to the optical power. The two examples in fig. 8.7 are from the previously mentioned eyes. Eye 1 has an almost constant power for distances from the optical axis up to 2 mm. In the periphery, the power of the eye increases (the displayed values correspond to the required correction). The power of the second eye is constant only for distances less than 1 mm.

## 8.5 Comparison with VISX WaveScan™

VISX WaveScan™ is one of the first commercial wavefront sensors for the measurements at the human eye. Numerous clinical studies have been done with this device in the last few years[Bil02]. A comparison of this device with the system, that has been developed for this thesis, is interesting.

In fig. 8.8a, the result of a measurement with WaveScan™ is shown. Figure 8.8b shows the result of a measurement at the same eye (patient ms, left eye ) with the other device. The difference between the values for the sphere of -2.85 dpt and -3.17 and the astigmatism of 0.79 and 0.60 could be the result of different pupil sizes. The angles of the astigmatism of 168° and 162° are almost equal. Apart from the colors, the "Bille Aberration Map" on the left side is very similar to the "Contour Lines" on the right side.

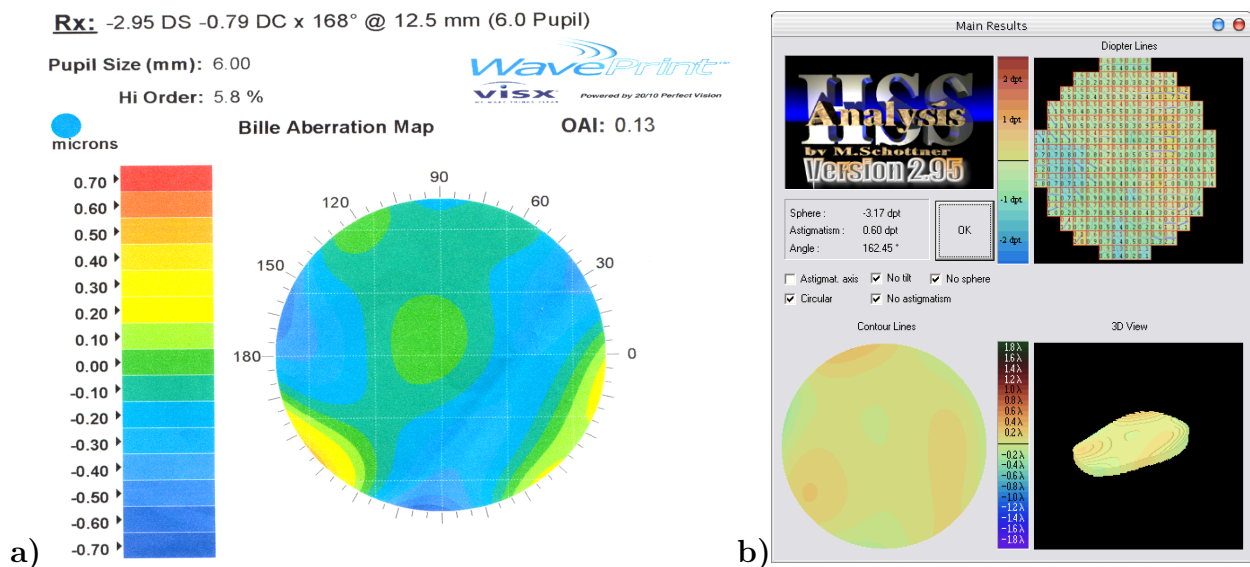


Figure 8.8: Comparison: a) WaveScan™ - b) HSS Analysis

# Chapter 9

## Summary and discussion

The two experimental systems developed in this thesis are suitable to measure complex aberrations of the human eye. The first system was used for international clinical studies. Three copies of this device have been built to do further measurements. The second device with the integrated cylinder compensation allows to measure patients with strong astigmatism.

Several improvements of the optical setup are possible. The reliability could be improved by using an internal reference. This could be realized with a removable mirror. A fixation target with a variable wavelength is suitable to extend the abilities of the system to chromatic aberrations. A small computer display, that allows to show symbols at different positions, could be used as target to get information about off axis aberrations. The light with a wavelength of 785 nm is still visible and for some people it is also disturbing. Since the sensitivity of the camera is limited, the intensity of light can't be reduced significantly. From this fact, a wavelength of about 800 nm could be a better choice, since the sensitivity of the human eye decreases faster with an increasing wavelength than those of the camera, and the optical properties of the eye for these two wavelengths are almost the same. The accuracy of the system could be enhanced by using a high resolution camera. The small sensitivity of these cameras can be enhanced by a longer integration time. A step in the other direction is the use of a high speed camera. Higher temporal resolution would allow to analyze dynamic processes in the optical system of the eye. For repetition rates of 1000 Hz or more, the combination of camera, framegrabber and image processing could be replaced by one single ASIC chip. First experiments with this kind of wavefront analysis have already been done at the Kirchhoff-Institute in Heidelberg.

The spot finding algorithm is able to recognize all kind of strong aberrations. Even missing spots and spots which doesn't correspond to a subpixel are no problem. Extreme patterns still require manual post-processing. Future efforts concerning the spot finding algorithm could concentrate on an automatization of the analysis of these patterns. For some kinds of aberrations, a modal estimation of the wavefront using 6.-order Zernike Polynomials, is not suitable. Especially for eyes with defects at the cornea higher orders of

Zernike Polynomials up to 10. order or higher are recommended. The mathematical effort for this enhancement is very high. Integration of the gradients within the subapertures is an approach, that hasn't the limitations of the modal estimation. A recommended solution would be a combined estimation with both components. A completely different approach is to use every set of 4 neighboring subapertures as a individual wavefront sensor. This is an very simple, but vivid kind of a representation of the optical properties within the pupil of the eye. This procedure is not affected by the limitations of modal estimations, since every single mini wavefront sensor is almost independent of distortions in other areas of the wavefront.

The computer programs, that have been developed in the framework of this thesis showed, that they are flexible tools for numerous applications. Future computers will be able to use this software for real-time processing of the entire data. Other possible improvements could be a user interface, that can be used by everyone, the use of higher order polynomials or the automatic analysis of time series.

# Appendix A

## Calculation of Zernike polynomials

### A.1 Calculation

The odd and even Zernike polynomials are given by

$${}^oU_n^m(\rho, \theta) = R_n^m(\rho) \sin(m\theta)$$

$${}^eU_n^m(\rho, \theta) = R_n^m(\rho) \cos(m\theta)$$

with radial function

$$R_n^m(\rho) = \sum_{s=0}^{(n-m)/2} \frac{(-1)^s (n-s)!}{s! [\frac{1}{2}(n+m)-s]! [\frac{1}{2}(n-m)-s]!} \rho^{n-2s}$$

The variables  $n$  and  $m$  are integers with  $n \geq m \geq 0$  and  $n-m$  even. Otherwise,  $R_n^m(\rho) = 0$ . Here,  $\theta$  is the azimuthal angle with  $0 \leq \theta < 2\pi$  and  $\rho$  is the radial distance with  $0 \leq \rho \leq 1$ . The radial function satisfy the orthogonality relation

$$\int_0^1 R_n^m(\rho) R_{n'}^m(\rho) d\rho = \frac{1}{2(n+1)} \delta_{nn'},$$

where  $\delta_{ij}$  is the Kronecker delta.

## A.2 Polar coordinates

```
[> restart;
> zfolge:= ( (-1)^s*(n-s)! )/(s!*((n+m)/2-s)!*((n-m)/2-s)!)*rho^(n-2*s);

      (n-2s)
      (-1)^s (n-s)! rho
zfolge := -----
      s! (1/2 n + 1/2 m - s)! (1/2 n - 1/2 m - s)!

> zsum:=sum(zfolge,s=0..(n-m)/2);

      n! rho^n hypergeom( [ -1/2 n - 1/2 m, -1/2 n + 1/2 m ], [-n], 1/2 )
zsum := -----
      (1/2 n + 1/2 m)! (1/2 n - 1/2 m)!

> i:=0;
      i:=0

> for n from 0 to 6 by 1 do
  for m from -n to n by 2 do
    if(m = 0) then
      zernike:=expand(simplify(zsum)) fi;
    if(m > 0) then
      zernike:=expand(simplify(zsum))*cos(m*theta) fi;
    if(m < 0) then
      zernike:=expand(simplify(zsum))*sin(-m*theta) fi;
    lprint(i,n,m);
    print(zernike);
    i:=i+1;
  od;
od;
```

Figure A.1: Maple script generating polar Zernike polynomials

The following Zernike polynomials in polar coordinates are calculated by a math software called Maple using the script in fig.A.1. The polynomials are represented by  $Z_i(n, m)$  where  $i$  is the number of the polynomial,  $n$  the order and  $m$  the azimuthal order.

$$Z_0(0,0) = 1$$

$$Z_1(1,-1) = \rho \sin(\theta)$$

$$Z_2(1,1) = \rho \cos(\theta)$$

$$Z_3(2,-2) = \rho^2 \sin(2\theta)$$

$$Z_4(2,0) = 2\rho^2 - 1$$

$$Z_5(2,2) = \rho^2 \cos(2\theta)$$

$$Z_6(3,-3) = \rho^3 \sin(3\theta)$$

$$Z_7(3,-1) = (3\rho^3 - 2\rho) \sin(\theta)$$

$$Z_8(3,1) = (3\rho^3 - 2\rho) \cos(\theta)$$

$$Z_9(3,3) = \rho^3 \cos(3\theta)$$



$$\begin{aligned}
Z_{10}(4, -4) &= \rho^4 \sin(4\theta) \\
Z_{11}(4, -2) &= (4\rho^4 - 3\rho^2) \sin(2\theta) \\
Z_{12}(4, 0) &= 6\rho^4 - 6\rho^2 + 1 \\
Z_{13}(4, 2) &= (4\rho^4 - 3\rho^2) \cos(2\theta) \\
Z_{14}(4, 4) &= \rho^4 \cos(4\theta)
\end{aligned}$$

$$\begin{aligned}
Z_{15}(5, -5) &= \rho^5 \sin(5\theta) \\
Z_{16}(5, -3) &= (5\rho^5 - 4\rho^3) \sin(3\theta) \\
Z_{17}(5, -1) &= (10\rho^5 - 12\rho^3 + 3\rho) \sin(\theta) \\
Z_{18}(5, 1) &= (10\rho^5 - 12\rho^3 + 3\rho) \cos(\theta) \\
Z_{19}(5, 3) &= (5\rho^5 - 4\rho^3) \cos(3\theta) \\
Z_{20}(5, 5) &= \rho^5 \cos(5\theta)
\end{aligned}$$

$$\begin{aligned}
Z_{21}(6, -6) &= \rho^6 \sin(6\theta) \\
Z_{22}(6, -4) &= (6\rho^6 - 5\rho^4) \sin(4\theta) \\
Z_{23}(6, -2) &= (15\rho^6 - 20\rho^4 + 6\rho^2) \sin(2\theta) \\
Z_{24}(6, 0) &= 20\rho^6 - 30\rho^4 + 12\rho^2 - 1 \\
Z_{25}(6, 2) &= (15\rho^6 - 20\rho^4 + 6\rho^2) \cos(2\theta) \\
Z_{26}(6, 4) &= (6\rho^6 - 5\rho^4) \cos(4\theta) \\
Z_{27}(6, 6) &= \rho^6 \cos(6\theta)
\end{aligned}$$

$$\begin{aligned}
Z_{28}(7, -7) &= \rho^7 \sin(7\theta) \\
Z_{29}(7, -5) &= (7\rho^7 - 6\rho^5) \sin(5\theta) \\
Z_{30}(7, -3) &= (21\rho^7 - 30\rho^5 + 10\rho^3) \sin(3\theta) \\
Z_{31}(7, -1) &= (35\rho^7 - 60\rho^5 + 30\rho^3 - 4\rho) \sin(\theta) \\
Z_{32}(7, 1) &= (35\rho^7 - 60\rho^5 + 30\rho^3 - 4\rho) \cos(\theta) \\
Z_{33}(7, 3) &= (21\rho^7 - 30\rho^5 + 10\rho^3) \cos(3\theta) \\
Z_{34}(7, 5) &= (7\rho^7 - 6\rho^5) \cos(5\theta) \\
Z_{35}(7, 7) &= \rho^7 \cos(7\theta)
\end{aligned}$$

$$\begin{aligned}
Z_{36}(8, -8) &= \rho^8 \sin(8\theta) \\
Z_{37}(8, -6) &= (8\rho^8 - 7\rho^6) \sin(6\theta) \\
Z_{38}(8, -4) &= (28\rho^8 - 42\rho^6 + 15\rho^4) \sin(4\theta) \\
Z_{39}(8, -2) &= (56\rho^8 - 105\rho^6 + 60\rho^4 - 10\rho^2) \sin(2\theta) \\
Z_{40}(8, 0) &= 70\rho^8 - 140\rho^6 + 90\rho^4 - 20\rho^2 + 1 \\
Z_{41}(8, 2) &= (56\rho^8 - 105\rho^6 + 60\rho^4 - 10\rho^2) \cos(2\theta) \\
Z_{42}(8, 4) &= (28\rho^8 - 42\rho^6 + 15\rho^4) \cos(4\theta) \\
Z_{43}(8, 6) &= (8\rho^8 - 7\rho^6) \cos(6\theta) \\
Z_{44}(8, 8) &= \rho^8 \cos(8\theta)
\end{aligned}$$

$$\begin{aligned}
Z_{45}(9, -9) &= \rho^9 \sin(9\theta) \\
Z_{46}(9, -7) &= (9\rho^9 - 8\rho^7) \sin(7\theta) \\
Z_{47}(9, -5) &= (36\rho^9 - 56\rho^7 + 21\rho^5) \sin(5\theta) \\
Z_{48}(9, -3) &= (84\rho^9 - 168\rho^7 + 105\rho^5 - 20\rho^3) \sin(3\theta) \\
Z_{49}(9, -1) &= (126\rho^9 - 280\rho^7 + 210\rho^5 - 60\rho^3 + 5\rho) \sin(\theta) \\
Z_{50}(9, 1) &= (126\rho^9 - 280\rho^7 + 210\rho^5 - 60\rho^3 + 5\rho) \cos(\theta) \\
Z_{51}(9, 3) &= (84\rho^9 - 168\rho^7 + 105\rho^5 - 20\rho^3) \cos(3\theta) \\
Z_{52}(9, 5) &= (36\rho^9 - 56\rho^7 + 21\rho^5) \cos(5\theta) \\
Z_{53}(9, 7) &= (9\rho^9 - 8\rho^7) \cos(7\theta) \\
Z_{54}(9, 9) &= \rho^9 \cos(9\theta)
\end{aligned}$$

---

$$\begin{aligned}Z_{55}(10, -10) &= \rho^{10} \sin(10\theta) \\Z_{56}(10, -8) &= (10\rho^{10} - 9\rho^8) \sin(8\theta) \\Z_{57}(10, -6) &= (45\rho^{10} - 72\rho^8 + 28\rho^6) \sin(6\theta) \\Z_{58}(10, -4) &= (120\rho^{10} - 252\rho^8 + 168\rho^6 - 35\rho^4) \sin(4\theta) \\Z_{59}(10, -2) &= (210\rho^{10} - 504\rho^8 + 420\rho^6 - 140\rho^4 + 15\rho^2) \sin(2\theta) \\Z_{60}(10, 0) &= 252\rho^{10} - 630\rho^8 + 560\rho^6 - 210\rho^4 + 30\rho^2 - 1 \\Z_{61}(10, 2) &= (210\rho^{10} - 504\rho^8 + 420\rho^6 - 140\rho^4 + 15\rho^2) \cos(2\theta) \\Z_{62}(10, 4) &= (120\rho^{10} - 252\rho^8 + 168\rho^6 - 35\rho^4) \cos(4\theta) \\Z_{63}(10, 6) &= (45\rho^{10} - 72\rho^8 + 28\rho^6) \cos(6\theta) \\Z_{64}(10, 8) &= (10\rho^{10} - 9\rho^8) \cos(8\theta) \\Z_{65}(10, 10) &= \rho^{10} \cos(10\theta)\end{aligned}$$

## A.3 Cartesian coordinates

The following Zernike polynomials in cartesian coordinates are calculated by a math software called Maple, using the script in fig.A.2. The polynomials are represented by  $Z_i(n, m)$  where  $i$  is the number of the polynomial,  $n$  the order and  $m$  the azimuthal order.

$$Z_0(0, 0) = 1$$

$$Z_1(1, -1) = x$$

$$Z_2(1, 1) = y$$

$$Z_3(2, -2) = 2xy$$

$$Z_4(2, 0) = 2x^2 + 2y^2 - 1$$

$$Z_5(2, 2) = -x^2 + y^2$$

$$Z_6(3, -3) = 3xy^2 - x^3$$

$$Z_7(3, -1) = 3x^3 + 3xy^2 - 2x$$

$$Z_8(3, 1) = 3yx^2 + 3y^3 - 2y$$

$$Z_9(3, 3) = y^3 - 3yx^2$$

$$Z_{10}(4, -4) = -4x^3y + 4xy^3$$

$$Z_{11}(4, -2) = 8x^3y + 8xy^3 - 6xy$$

$$Z_{12}(4, 0) = 6x^4 + 12x^2y^2 + 6y^4 - 6x^2 - 6y^2 + 1$$

$$Z_{13}(4, 2) = -4x^4 + 4y^4 + 3x^2 - 3y^2$$

$$Z_{14}(4, 4) = x^4 - 6x^2y^2 + y^4$$

$$Z_{15}(5, -5) = 5xy^4 - 10x^3y^2 + x^5$$

$$Z_{16}(5, -3) = 10x^3y^2 - 5x^5 + 15xy^4 - 12xy^2 + 4x^3$$

$$Z_{17}(5, -1) = 10x^5 + 20x^3y^2 + 10xy^4 - 12x^3 - 12xy^2 + 3x$$

$$Z_{18}(5, 1) = 10yx^4 + 20x^2y^3 + 10y^5 - 12yx^2 - 12y^3 + 3y$$

$$Z_{19}(5, 3) = -10x^2y^3 - 15yx^4 + 5y^5 - 4y^3 + 12yx^2$$

$$Z_{20}(5, 5) = y^5 - 10x^2y^3 + 5yx^4$$

```

[> restart;
[> ord:=10;
                                ord := 10
[> zrow:= ( (-1)^s*(n-s)! )/(s!*((n+m)/2-s)!*((n-m)/2-s)!)*rho^(n-2*s);
                                zrow := \frac{(-1)^s (n-s)! \rho^{(n-2s)}}{s! \left(\frac{1}{2}n + \frac{1}{2}m - s\right)! \left(\frac{1}{2}n - \frac{1}{2}m - s\right)!}
[> zsum:=sum(zrow,s=0..(n-m)/2);
                                zsum := \frac{n! \rho^n \operatorname{hypergeom}\left(\left[-\frac{1}{2}n + \frac{1}{2}m, -\frac{1}{2}n - \frac{1}{2}m\right], [-n], \frac{1}{\rho^2}\right)}{\left(\frac{1}{2}n + \frac{1}{2}m\right)! \left(\frac{1}{2}n - \frac{1}{2}m\right)!}
[> rho:=sqrt(x^2+y^2);
                                \rho := \sqrt{x^2 + y^2}
[> theta:=arctan(x/y);;
                                \theta := \arctan\left(\frac{x}{y}\right)
[> i:=0;
                                i := 0
[> for n from 0 to ord by 1 do
  for m from -n to n by 2 do
    if(m = 0) then
      zernike:=expand(simplify(zsum)) fi;
    if(m > 0) then
      zernike:=expand(radsimp(simplify(expand(cos(m*theta)*zsum)))
)fi;
    if(m < 0) then
      zernike:=expand(radsimp(simplify(expand(zsum*sin(-m*theta))))
)fi;
    lprint(i,n,m);
    print(zernike);
    i:=i+1;
  od;
od;

```

Figure A.2: Maple script generating cartesian Zernike polynomials

$$\begin{aligned}
Z_{21}(6, -6) &= 6x^5y - 20x^3y^3 + 6xy^5 \\
Z_{22}(6, -4) &= -24x^5y + 24xy^5 + 20x^3y - 20xy^3 \\
Z_{23}(6, -2) &= 30x^5y + 60x^3y^3 + 30xy^5 - 40x^3y - 40xy^3 + 12xy \\
Z_{24}(6, 0) &= 20x^6 + 60x^4y^2 + 60x^2y^4 + 20y^6 - 30x^4 - 60x^2y^2 - 30y^4 + 12x^2 \\
&\quad + 12y^2 - 1 \\
Z_{25}(6, 2) &= -15x^6 - 15x^4y^2 + 15x^2y^4 + 15y^6 + 20x^4 - 20y^4 - 6x^2 + 6y^2 \\
Z_{26}(6, 4) &= 6x^6 - 30x^4y^2 - 30x^2y^4 + 6y^6 - 5x^4 + 30x^2y^2 - 5y^4 \\
Z_{27}(6, 6) &= -x^6 + 15x^4y^2 - 15x^2y^4 + y^6
\end{aligned}$$

$$\begin{aligned}
Z_{28}(7, -7) &= 7xy^6 - 35x^3y^4 + 21x^5y^2 - x^7 \\
Z_{29}(7, -5) &= -35x^3y^4 - 63x^5y^2 + 7x^7 + 35xy^6 - 30xy^4 + 60x^3y^2 - 6x^5 \\
Z_{30}(7, -3) &= 21x^5y^2 - 21x^7 + 105x^3y^4 + 63xy^6 - 60x^3y^2 + 30x^5 - 90xy^4 \\
&\quad + 30xy^2 - 10x^3 \\
Z_{31}(7, -1) &= 35x^7 + 105x^5y^2 + 105x^3y^4 + 35xy^6 - 60x^5 - 120x^3y^2 - 60xy^4 \\
&\quad + 30x^3 + 30xy^2 - 4x \\
Z_{32}(7, 1) &= 35xy^6 + 105x^4y^3 + 105x^2y^5 + 35y^7 - 60yx^4 - 120x^2y^3 - 60y^5 \\
&\quad + 30x^2y + 30y^3 - 4y \\
Z_{33}(7, 3) &= -105x^4y^3 - 63yx^6 - 21x^2y^5 + 21y^7 + 60x^2y^3 + 90yx^4 - 30y^5 \\
&\quad + 10y^3 - 30x^2y \\
Z_{34}(7, 5) &= -63x^2y^5 - 35x^4y^3 + 35yx^6 + 7y^7 - 6y^5 + 60x^2y^3 - 30yx^4 \\
Z_{35}(7, 7) &= y^7 - 21x^2y^5 + 35x^4y^3 - 7yx^6
\end{aligned}$$

$$\begin{aligned}
Z_{36}(8, -8) &= -8x^7y + 56x^5y^3 - 56x^3y^5 + 8xy^7 \\
Z_{37}(8, -6) &= 48x^7y - 112x^5y^3 - 112x^3y^5 + 48xy^7 - 42x^5y + 140x^3y^3 \\
&\quad - 42xy^5 \\
Z_{38}(8, -4) &= -112x^7y - 112x^5y^3 + 112x^3y^5 + 112xy^7 + 168x^5y - 168xy^5 \\
&\quad - 60x^3y + 60xy^3 \\
Z_{39}(8, -2) &= 112x^7y + 336x^5y^3 + 336x^3y^5 + 112xy^7 - 210x^5y - 420x^3y^3 \\
&\quad - 210xy^5 + 120x^3y + 120xy^3 - 20xy \\
Z_{40}(8, 0) &= 70x^8 + 280x^6y^2 + 420x^4y^4 + 280x^2y^6 + 70y^8 - 140x^6 - 420x^4y^2 \\
&\quad - 420x^2y^4 - 140y^6 + 90x^4 + 180x^2y^2 + 90y^4 - 20x^2 - 20y^2 + 1 \\
Z_{41}(8, 2) &= -56x^8 - 112x^6y^2 + 112x^2y^6 + 56y^8 + 105x^6 + 105x^4y^2 \\
&\quad - 105x^2y^4 - 105y^6 - 60x^4y^4 + 10x^2 - 10y^2 \\
Z_{42}(8, 4) &= 28x^8 - 112x^6y^2 - 280x^4y^4 - 112x^2y^6 + 28y^8 - 42x^6 + 210x^4y^2 \\
&\quad + 210x^2y^4 - 42y^6 - 15x^4 - 90x^2y^2 + 15y^4 \\
Z_{43}(8, 6) &= -8x^8 + 112x^6y^2 - 112x^2y^6 + 8y^8 + 7x^6 - 105x^4y^2 + 105x^2y^4 \\
&\quad - 7y^6 \\
Z_{44}(8, 8) &= x^8 - 28x^6y^2 + 70x^4y^4 - 28x^2y^6 + y^8
\end{aligned}$$

$$\begin{aligned}
Z_{45}(9, -9) &= 9xy^8 - 84x^3y^6 + 126x^5y^4 - 36x^7y^2 + x^9 \\
Z_{46}(9, -7) &= -252x^3y^6 - 126x^5y^4 + 180x^7y^2 - 9x^9 + 63xy^8 - 56xy^6 \\
&\quad + 280x^3y^4 - 168x^5y^2 + 8x^7 \\
Z_{47}(9, -5) &= -504x^5y^4 - 288x^7y^2 + 36x^9 + 180xy^8 + 280x^3y^4 + 504x^5y^2 \\
&\quad - 56x^7 - 280xy^6 + 105xy^4 - 210x^3y^2 + 21x^5 \\
Z_{48}(9, -3) &= -84x^9 + 504x^5y^4 + 672x^3y^6 + 252xy^8 - 168x^5y^2 + 168x^7 \\
&\quad - 840x^3y^4 - 504xy^6 + 210x^3y^2 - 105x^5 + 315xy^4 - 60xy^2 \\
&\quad + 20x^3 \\
Z_{49}(9, -1) &= 126x^9 + 504x^7y^2 + 756x^5y^4 + 504x^3y^6 + 126xy^8 - 280x^7 \\
&\quad - 840x^5y^2 - 840x^3y^4 - 280xy^6 + 210x^5 + 420x^3y^2 + 210xy^4 \\
&\quad - 60x^3 - 60xy^2 + 5x \\
Z_{50}(9, 1) &= 126y^8 + 504x^6y^3 + 756x^4y^5 + 504x^2y^7 + 126y^9 - 280yx^6 \\
&\quad - 840x^4y^3 - 840x^2y^5 - 280y^7 + 210yx^4 + 420x^2y^3 + 210y^5 \\
&\quad - 60x^2y - 60y^3 + 5y \\
Z_{51}(9, 3) &= -672x^6y^3 - 252yx^8 - 504x^4y^5 + 84y^9 + 840x^4y^3 + 504yx^6 \\
&\quad + 168x^2y^5 - 168y^7 - 210x^2y^3 - 315yx^4 + 105y^5 - 20y^3 \\
&\quad + 60x^2y \\
Z_{52}(9, 5) &= -504x^4y^5 + 180yx^8 - 288x^2y^7 + 36y^9 + 504x^2y^5 + 280x^4y^3 \\
&\quad - 280yx^6 - 56y^7 + 21y^5 - 210x^2y^3 + 105yx^4 \\
Z_{53}(9, 7) &= -180x^2y^7 + 126x^4y^5 + 252x^6y^3 - 63yx^8 + 9y^9 - 8y^7 \\
&\quad + 168x^2y^5 - 280x^4y^3 + 56yx^6 \\
Z_{54}(9, 9) &= y^9 - 36x^2y^7 + 126x^4y^5 - 84x^6y^3 + 9yx^8
\end{aligned}$$

$$\begin{aligned}
Z_{55}(10, -10) &= 10x^9y - 120x^7y^3 + 252x^5y^5 - 120x^3y^7 + 10xy^9 \\
Z_{56}(10, -8) &= -80x^9y + 480x^7y^3 - 480x^3y^7 + 80xy^9 + 72x^7y - 504x^5y^3 \\
&\quad + 504x^3y^5 - 72xy^7 \\
Z_{57}(10, -6) &= 270x^9y - 360x^7y^3 - 1260x^5y^5 - 360x^3y^7 + 270xy^9 \\
&\quad - 432x^7y + 1008x^5y^3 + 1008x^3y^5 - 432xy^7 + 168x^5y \\
&\quad - 560x^3y^3 + 168xy^5 \\
Z_{58}(10, -4) &= -480x^9y - 960x^7y^3 + 960x^3y^7 + 480xy^9 + 1008x^7y \\
&\quad + 1008x^5y^3 - 1008x^3y^5 - 1008xy^7 - 672x^5y + 672xy^5 \\
&\quad + 140x^3y - 140xy^3 \\
Z_{59}(10, -2) &= 420x^9y + 1680x^7y^3 + 2520x^5y^5 + 1680x^3y^7 + 420xy^9 \\
&\quad - 1008x^7y - 3024x^5y^3 - 3024x^3y^5 - 1008xy^7 + 840x^5y \\
&\quad + 1680x^3y^3 + 840xy^5 - 280x^3y - 280xy^3 + 30xy \\
Z_{60}(10, 0) &= 252x^{10} + 1260x^8y^2 + 2520x^6y^4 + 2520x^4y^6 + 1260x^2y^8 \\
&\quad + 252y^{10} - 630x^8 - 2520x^6y^2 - 3780x^4y^4 - 2520x^2y^6 \\
&\quad - 630y^8 + 560x^6 + 1680x^4y^2 + 1680x^2y^4 + 560y^6 - 210x^4 \\
&\quad - 420x^2y^2 - 210y^4 + 30x^2 + 30y^2 - 1 \\
Z_{61}(10, 2) &= -420x^4y^2 + 420x^2y^4 + 504x^8 - 504y^8 - 15x^2 + 15y^2 \\
&\quad + 140x^4 - 140y^4 - 630x^8y^2 - 420x^6y^4 + 420x^4y^6 \\
&\quad + 630x^2y^8 - 420x^6 + 420y^6 - 210x^{10} + 210y^{10} + 1008x^6y^2 \\
&\quad - 1008x^2y^6 \\
Z_{62}(10, 4) &= -840x^4y^2 - 840x^2y^4 - 252x^8 - 252y^8 + 210x^2y^2 - 35x^4 \\
&\quad - 35y^4 - 360x^8y^2 - 1680x^6y^4 - 1680x^4y^6 - 360x^2y^8 \\
&\quad + 168x^6 + 168y^6 + 120x^{10} + 120y^{10} + 1008x^6y^2 + 2520x^4y^4 \\
&\quad + 1008x^2y^6 \\
Z_{63}(10, 6) &= -45x^{10} + 585x^8y^2 + 630x^6y^4 - 630x^4y^6 - 585x^2y^8 + 45y^{10} \\
&\quad + 72x^8 - 1008x^6y^2 + 1008x^2y^6 - 72y^8 - 28x^6 + 420x^4y^2 \\
&\quad - 420x^2y^4 + 28y^6 \\
Z_{64}(10, 8) &= 10x^{10} - 270x^8y^2 + 420x^6y^4 + 420x^4y^6 - 270x^2y^8 + 10y^{10} \\
&\quad - 9x^8 + 252x^6y^2 - 630x^4y^4 + 252x^2y^6 - 9y^8 \\
Z_{65}(10, 10) &= -x^{10} + 45x^8y^2 - 210x^6y^4 + 210x^4y^6 - 45x^2y^8 + y^{10}
\end{aligned}$$

# Appendix B

## Important software functions

In the following sections, some significant functions of HSS Simulator 1.x are listed. All program parts are written in C++.

### B.1 Creation of spots

```
void TFake::DrawSpot(double xpos,double ypos,int size,int design) {
    int x,y;
    int beamform=1;
    double cx=384;
    double cy=288;
    double distance;
    int value;
    int altwert;
    int pupil=CSpinEdit3->Value;
    double factor;
    double factor2=CSpinEdit4->Value/100.0;
    double beamd;

    int maxwert=255*65536+255*256+255;
    for(x=xpos-2*size;x<xpos+2*size;x++)
    {
        if(x<0 || x>767) continue;
        for(y=ypos-2*size;y<ypos+2*size;y++)
        {
            if(y<0 || y>575) continue;
            distance=sqrt( (x-xpos)*(x-xpos)+(y-ypos)*(y-ypos) );
            //altwert=Image2->Canvas->Pixels[x][y];
            beamd=sqrt( (x-cx)*(x-cx)+(y-cy)*(y-cy) );
            beamd=beamd/(pupil);

            if(beamform==0)factor=min(1.0,max(0.0,(beamd>1)? 0.0:1.0 ) );
            if(beamform==2)factor=min(1.0,max(0.0,1-1*beamd ) );
            if(beamform==1)factor=min(1.0,max(0.0,exp(-4*(beamd) ) ) );
            factor*=factor2;

            if(design==0)
            {
                value=255;
                value *=factor;
            }
        }
    }
}
```



```

        if(distance<size)
            Image1->Canvas->Pixels[x][y] =(TColor) (value*65536+value*256+value);
    }
    if(design==1)
    {
        value=max(0,(int) (255-255*distance/size) );
        value *=factor;

        Image1->Canvas->Pixels[x][y] =(TColor)(min(maxwert,altwert+value*65536+value*256+value));
    }
    if(design==2)
    {
        value=max(0,(int) (255*exp(-2*(distance*distance)/(size*size)) ));
        value *=factor;

        Image1->Canvas->Pixels[x][y] =(TColor)(min(maxwert,altwert+value*65536+value*256+value));
    }
    }
}
}
}

```

## B.2 Calculation of z-values

```

double TMainForm::GetZ(double x,double y) {
    double z=0.0;

    // 0.order
    z+= zlist[ 0];
    z+= zlist[ 1]*x;
    z+= zlist[ 2]*y;
    z+= zlist[ 3]*2*x*y;
    z+= zlist[ 4]*(2*x*x+2*y*y-1);
    z+= zlist[ 5]*(-x*x+y*y);
    z+= zlist[ 6]*(3*x*y*y-x*x*x);
    z+= zlist[ 7]*(3*x*x*x+3*x*y*y-2*x);
    z+= zlist[ 8]*(3*y*x*x+3*y*y*y-2*y);
    z+= zlist[ 9]*(y*y*y-3*y*x*x);

    // 4.order
    z+= zlist[10]*(-4*x*x*x*y+4*x*y*y*y);
    z+= zlist[11]*(8*x*x*x*y+8*x*y*y*y-6*x*y);
    z+= zlist[12]*(6*x*x*x*x+12*x*x*y*y+6*y*y*y*y-6*x*x-6*y*y+1);
    z+= zlist[13]*(-4*x*x*x*x+4*y*y*y*y+3*x*x-3*y*y);
    z+= zlist[14]*(x*x*x*x-6*x*x*y*y+y*y*y*y);

    // 5.order
    z+= zlist[15]*(5*x*y*y*y*y-10*x*x*x*y*y+x*x*x*x*x);
    z+= zlist[16]*(10*x*x*x*x*y*y-5*x*x*x*x*x+15*x*y*y*y*y-12*x*y*y+4*x*x*x);
    z+= zlist[17]*(10*x*x*x*x*x+20*x*x*x*y*y+10*x*y*y*y*y-12*x*x*x-12*x*y*y+3*x);
    z+= zlist[18]*(10*y*x*x*x*x+20*x*x*y*y*y+10*y*y*y*y*y-12*y*x*x-12*y*y*y+3*y);
    z+= zlist[19]*(-10*x*x*y*y*y-15*y*x*x*x*x+5*y*y*y*y*y-4*y*y*y+12*y*x*x);
    z+= zlist[20]*(y*y*y*y*y-10*x*x*y*y*y+5*y*x*x*x*x);

    // 6.order
    z+= zlist[21]*(6.0*x*x*x*x*x*y-20.0*x*x*x*y*y*y+6.0*x*y*y*y*y*y);
    z+= zlist[22]*(-24.0*x*x*x*x*x*y+24.0*x*y*y*y*y*y+20.0*x*x*x*y-20.0*x*y*y*y);
    z+= zlist[23]*(30.0*x*x*x*x*x*y+60.0*x*x*x*y*y*y+30.0*x*y*y*y*y*y-40.0*x*x*x*y
        -40.0*x*y*y*y+12.0*x*y);
}

```

```

z+= zlist[24]*(20.0*x*x*x*x*x*x*x+60.0*x*x*x*x*x*y*y+60.0*x*x*y*y*y*y*y+20.0*y*y*y*y*y*y
-30.0*x*x*x*x*x-60.0*x*x*y*y-30.0*y*y*y*y*y+12.0*x*x+12.0*y*y-1.0);
z+= zlist[25]*(-15.0*x*x*x*x*x*x*x-15.0*x*x*x*x*x*y*y+15.0*x*x*y*y*y*y*y+15.0*y*y*y*y*y*y
+20.0*x*x*x*x*x-20.0*y*y*y*y-6.0*x*x+6.0*y*y);
z+= zlist[26]*(6.0*x*x*x*x*x*x*x-30.0*x*x*x*x*x*y*y-30.0*x*x*y*y*y*y*y+6.0*y*y*y*y*y*y
-5.0*x*x*x*x*x+30.0*x*x*y*y-5.0*y*y*y*y);
z+= zlist[27]*(-x*x*x*x*x*x*x+15.0*x*x*x*x*x*y*y-15.0*x*x*y*y*y*y+y*y*y*y*y*y);

// 7.order
z+= zlist[28]*(7.0*x*y*y*y*y*y*y-35.0*x*x*x*x*y*y*y+21.0*x*x*x*x*x*y*y-x*x*x*x*x*x*x);
z+= zlist[29]*(-35.0*x*x*x*x*y*y*y-63.0*x*x*x*x*x*y*y+7.0*x*x*x*x*x*x*x
+35.0*x*y*y*y*y*y-30.0*x*y*y*y*y+60.0*x*x*x*x*y-6.0*x*x*x*x*x);
z+= zlist[30]*(21.0*x*x*x*x*x*x*y-21.0*x*x*x*x*x*x*x+105.0*x*x*x*x*y*y*y
+63.0*x*y*y*y*y*y-60.0*x*x*x*x*y+30.0*x*x*x*x*x-90.0*x*y*y*y*y+30.0*x*y*y-10.0*x*x*x);
z+= zlist[31]*(35.0*x*x*x*x*x*x*x+105.0*x*x*x*x*x*x*y+105.0*x*x*x*x*y*y*y+35.0*x*y*y*y*y*y
-60.0*x*x*x*x*x*x-120.0*x*x*x*x*x*y-60.0*x*y*y*y*y+30.0*x*x*x+30.0*x*y*y-4.0*x);
z+= zlist[32]*(35.0*y*x*x*x*x*x+105.0*x*x*x*x*x*y*y+105.0*x*x*y*y*y*y*y+35.0*y*y*y*y*y*y
-60.0*y*x*x*x*x*x-120.0*x*x*y*y*y-60.0*y*y*y*y*y+30.0*x*x*y+30.0*y*y*y-4.0*y);
z+= zlist[33]*(-105.0*x*x*x*x*x*y*y-63.0*y*x*x*x*x*x*x-21.0*x*x*y*y*y*y*y+21.0*y*y*y*y*y*y
+60.0*x*x*y*y*y+90.0*y*x*x*x*x-30.0*y*y*y*y*y+10.0*y*y*y-30.0*x*x*x);
z+= zlist[34]*(-63.0*x*x*x*y*y*y*y-35.0*x*x*x*x*x*x*y+35.0*y*x*x*x*x*x*x+7.0*y*y*y*y*y*y
-6.0*y*y*y*y*y+60.0*x*x*y*y*y-30.0*y*x*x*x*x);
z+= zlist[35]*(y*y*y*y*y*y*y-21.0*x*x*y*y*y*y*y+35.0*x*x*x*x*x*y*y-7.0*y*x*x*x*x*x*x);

// 8.order
z+= zlist[36]*(-8.0*x*x*x*x*x*x*x*x*x*y+56.0*x*x*x*x*x*x*x*y*y-56.0*x*x*x*x*y*y*y*y
+8.0*x*y*y*y*y*y*y);
z+= zlist[37]*(48.0*x*x*x*x*x*x*x*x*y-112.0*x*x*x*x*x*x*y*y-112.0*x*x*x*x*y*y*y*y
+48.0*x*y*y*y*y*y*y-42.0*x*x*x*x*x*x*y+140.0*x*x*x*x*y*y*y-42.0*x*y*y*y*y*y);
z+= zlist[38]*(-112.0*x*x*x*x*x*x*x*x*y-112.0*x*x*x*x*x*x*x*y*y+112.0*x*x*x*x*y*y*y*y
+112.0*x*y*y*y*y*y*y+168.0*x*x*x*x*x*x*y-168.0*x*y*y*y*y*y-60.0*x*x*x*y+60.0*x*y
*y*y);
z+= zlist[39]*(112.0*x*x*x*x*x*x*x*x*y+336.0*x*x*x*x*x*x*y*y+336.0*x*x*x*x*y*y*y*y
+112.0*x*y*y*y*y*y*y-210.0*x*x*x*x*x*x*y-420.0*x*x*x*x*y*y-y-210.0*x*y*y*y*y*y
+120.0*x*x*x*x*y+120.0*x*y*y*y-20.0*x*x);
z+= zlist[40]*(70.0*x*x*x*x*x*x*x*x+280.0*x*x*x*x*x*x*x*y+420.0*x*x*x*x*x*y*y*y
+280.0*x*x*x*y*y*y*y*y+70.0*y*y*y*y*y*y*y-140.0*x*x*x*x*x*x-420.0*x*x*x*x*x*y
-420.0*x*x*y*y*y*y-140.0*y*y*y*y*y*y+90.0*x*x*x*x+180.0*x*x*x*y+90.0*y*y*y*y
-20.0*x*x-20.0*y*y+1.0);
z+= zlist[41]*(-56.0*x*x*x*x*x*x*x*x*x-112.0*x*x*x*x*x*x*x*x*y+112.0*x*x*x*y*y*y*y
+56.0*y*y*y*y*y*y*y+105.0*x*x*x*x*x*x+105.0*x*x*x*x*x*y-105.0*x*x*y*y*y*y
-105.0*y*y*y*y*y-y-60.0*x*x*x*x+60.0*y*y*y*y+10.0*x*x-10.0*y*y);
z+= zlist[42]*(28.0*x*x*x*x*x*x*x*x-112.0*x*x*x*x*x*x*x*y-280.0*x*x*x*x*x*y*y*y
-112.0*x*x*x*y*y*y*y+28.0*y*y*y*y*y*y-42.0*x*x*x*x*x*x+210.0*x*x*x*x*x*y
+210.0*x*x*x*y*y*y-42.0*y*y*y*y*y+15.0*x*x*x*x-90.0*x*x*x*y+15.0*y*y*y*y);
z+= zlist[43]*(-8.0*x*x*x*x*x*x*x*x+112.0*x*x*x*x*x*x*x*y-112.0*x*x*x*y*y*y*y
+8.0*y*y*y*y*y*y*y+7.0*x*x*x*x*x*x-105.0*x*x*x*x*x*y+105.0*x*x*x*y*y*y
-7.0*y*y*y*y*y);
z+= zlist[44]*(x*x*x*x*x*x*x*x*x-28.0*x*x*x*x*x*x*x*y+70.0*x*x*x*x*x*y*y*y
-28.0*x*x*x*y*y*y*y+y*y*y*y*y*y);

// 9.order
z+= zlist[45]*(9.0*x*y*y*y*y*y*y-84.0*x*x*x*x*x*y*y*y+126.0*x*x*x*x*x*x*y*y*y
-36.0*x*x*x*x*x*x*x*x*y+x*x*x*x*x*x*x*x);
z+= zlist[46]*(-252.0*x*x*x*x*y*y*y*y-126.0*x*x*x*x*x*x*y*y*y+180.0*x*x*x*x*x*x*x*x*y
-9.0*x*x*x*x*x*x*x*x*x+63.0*x*y*y*y*y*y*y-56.0*x*y*y*y*y*y+280.0*x*x
*x*y*y*y-168.0*x*x*x*x*x*y+8.0*x*x*x*x*x*x*x);
z+= zlist[47]*(-504.0*x*x*x*x*x*x*y*y-288.0*x*x*x*x*x*x*x*x*y+36.0*x*x*x*x*x*x*x*x
+180.0*x*x*x*y*y*y*y+280.0*x*x*x*x*y*y*y+504.0*x*x*x*x*x*x*x*y-56.0*x*x*x
*x*x*x-280.0*x*y*y*y*y*y+105.0*x*y*y*y-210.0*x*x*x*x*y+21.0*x*x*x*x*x);
z+= zlist[48]*(-84.0*x*x*x*x*x*x*x*x+504.0*x*x*x*x*x*x*x*y+672.0*x*x*x*x*y*y*y
+252.0*x*y*y*y*y*y-y-168.0*x*x*x*x*x*x*y+168.0*x*x*x*x*x*x-x-840.0*x*x*x
*y*y*y-504.0*x*x*y*y*y+y+210.0*x*x*x*x*y-105.0*x*x*x*x*x+315.0*x*y*y*y
-60.0*x*x*y+20.0*x*x*x);
z+= zlist[49]*(126.0*x*x*x*x*x*x*x*x+504.0*x*x*x*x*x*x*x*y+756.0*x*x*x*x*x*x*y

```

```

+504.0*x*x*x*y*y*y*y*y+126.0*x*y*y*y*y*y*y*y-280.0*x*x*x*x*x*x*x-840.0*x
*x*x*x*x*y*y-840.0*x*x*x*y*y*y*y-280.0*x*y*y*y*y*y*y+210.0*x*x*x*x*x+420.0*x*x
*x*y*y+210.0*x*y*y*y*y-60.0*x*x*x-60.0*x*y*y+5.0*x);
z+= zlist[50]*(126.0*y*x*x*x*x*x*x*x+504.0*x*x*x*x*x*x*y*y*y+756.0*x*x*x*x*y*y*y*y
+504.0*x*x*y*y*y*y*y*y*y+126.0*y*y*y*y*y*y*y*y-280.0*y*x*x*x*x*x*x-840.0*x
*x*x*x*y*y*y-840.0*x*x*y*y*y*y*y-280.0*y*y*y*y*y*y*y+210.0*y*x*x*x*x+420.0*x*x
*y*y+210.0*y*y*y*y*y-60.0*x*x*y-60.0*y*y*y+5.0*y);
z+= zlist[51]*(-672.0*x*x*x*x*x*x*x*y*y-252.0*y*x*x*x*x*x*x*x-504.0*x*x*x*x*y*y*y*y
+84.0*y*y*y*y*y*y*y*y+840.0*x*x*x*x*y*y*y+504.0*y*x*x*x*x*x*x+168.0*x*x*y
*y*y*y-168.0*y*y*y*y*y*y-210.0*x*x*y*y*y-315.0*y*x*x*x*x+105.0*y*y*y*y*y
-20.0*y*y*y+60.0*x*x*y);
z+= zlist[52]*(-504.0*x*x*x*x*x*y*y*y*y+180.0*y*x*x*x*x*x*x*x-288.0*x*x*y*y*y*y*y*y
+36.0*y*y*y*y*y*y*y*y+504.0*x*x*y*y*y*y*y+280.0*x*x*x*x*y*y*y-280.0*y*x*x
*x*x*x-56.0*y*y*y*y*y*y*y+21.0*y*y*y*y*y-210.0*x*x*y*y*y+105.0*y*x*x*x*x);
z+= zlist[53]*(-180.0*x*x*y*y*y*y*y*y+126.0*x*x*x*x*y*y*y*y+252.0*x*x*x*x*x*x*y*y
-63.0*y*x*x*x*x*x*x*x+9.0*y*y*y*y*y*y*y*y-8.0*y*y*y*y*y*y*y+168.0*x*x*y
*y*y*y-280.0*x*x*x*x*y*y+56.0*y*x*x*x*x*x*x);
z+= zlist[54]*(y*y*y*y*y*y*y*y-36.0*x*x*y*y*y*y*y+126.0*x*x*x*x*y*y*y*y
-84.0*x*x*x*x*x*x*y*y+9.0*y*x*x*x*x*x*x*x);

// 10.order
z+= zlist[55]*(10.0*x*x*x*x*x*x*x*x*y-120.0*x*x*x*x*x*x*x*x*y*y+252.0*x*x*x*x*x*y*y*y*y
-120.0*x*x*x*y*y*y*y*y*y+10.0*x*y*y*y*y*y*y*y);
z+= zlist[56]*(-80.0*x*x*x*x*x*x*x*x*y+480.0*x*x*x*x*x*x*x*y*y-480.0*x*x*x*y*y*y*y*y
+80.0*x*y*y*y*y*y*y*y+72.0*x*x*x*x*x*x*x*y-504.0*x*x*x*x*x*y*y+
504.0*x*x*x*y*y*y*y-72.0*x*y*y*y*y*y*y);
z+= zlist[57]*(270.0*x*x*x*x*x*x*x*x*y-360.0*x*x*x*x*x*x*x*y*y-1260.0*x*x*x*x*x*x*y*y*y
-360.0*x*x*x*y*y*y*y*y*y+270.0*x*y*y*y*y*y*y*y-432.0*x*x*x*x*x
*x*x*y+1008.0*x*x*x*x*x*x*y*y+1008.0*x*x*x*y*y*y*y-432.0*x*y*y*y*y*y*y+168.0
*x*x*x*x*x*y-560.0*x*x*x*y*y+168.0*x*y*y*y*y);
z+= zlist[58]*(-480.0*x*x*x*x*x*x*x*x*y-960.0*x*x*x*x*x*x*x*x*y+960.0*x*x*x*y*y*y*y*y
+480.0*x*y*y*y*y*y*y*y+1008.0*x*x*x*x*x*x*x*y+1008.0*x*x*x*x*x*y
*y-1008.0*x*x*x*y*y*y*y-1008.0*x*y*y*y*y*y*y-672.0*x*x*x*x*x*y+672.0*x*y*y
*y*y+140.0*x*x*x*y-140.0*x*y*y);
z+= zlist[59]*(420.0*x*x*x*x*x*x*x*x*x*y+1680.0*x*x*x*x*x*x*x*x*y*y+2520.0*x*x*x*x*x*x*y*y*y
+1680.0*x*x*x*y*y*y*y*y*y+420.0*x*y*y*y*y*y*y*y-1008.0*x*x*x
*x*x*x*y-3024.0*x*x*x*x*x*x*y*y-3024.0*x*x*x*y*y*y*y-1008.0*x*y*y*y*y*y*y+
840.0*x*x*x*x*x*x*y+1680.0*x*x*x*y*y*y+840.0*x*y*y*y*y-280.0*x*x*x*y-280.0*x*y
*y+30.0*x*y);
z+= zlist[60]*(252.0*pow(x,10.0)+1260.0*x*x*x*x*x*x*x*x*y+2520.0*x*x*x*x*x*x*x*y*y
+2520.0*x*x*x*x*y*y*y*y*y+1260.0*x*x*y*y*y*y*y*y+252.0*pow(y,10.0)
-630.0*x*x*x*x*x*x-2520.0*x*x*x*x*x*x*y-3780.0*x*x*x*x*x*y*y-2520.0*x*x
*y*y*y*y*y-630.0*y*y*y*y*y*y+560.0*x*x*x*x*x+1680.0*x*x*x*x*y+1680.0*
*x*x*y*y*y+560.0*y*y*y*y*y-210.0*x*x*x-420.0*x*x*y-210.0*y*y*y+30.0*x*
x+30.0*y-1.0);
z+= zlist[61]*(-420.0*x*x*x*x*x*x-15.0*x*x+15.0*y*y+210.0*pow(y,10.0)+140.0*x*x*x
-504.0*y*y*y*y*y-420.0*x*x*x*x*x*x*y*y+420.0*x*x*x*x*x*y*y*y+
630.0*x*x*y*y*y*y*y-630.0*x*x*x*x*x*x*x*x*y-210.0*pow(x,10.0)-140.0*y*y
*y+420.0*y*y*y*y*y+504.0*x*x*x*x*x*x*x-420.0*x*x*x*x*x*y+420.0*x*x*y*y*y
-1008.0*x*x*y*y*y*y+1008.0*x*x*x*x*x*x*y);
z+= zlist[62]*(168.0*x*x*x*x*x+120.0*pow(y,10.0)-35.0*x*x*x-252.0*y*y*y*y*y*y
-1680.0*x*x*x*x*x*x*x*y*y-1680.0*x*x*x*x*x*y*y*y*y-360.0*x*x*y*y*y*y*y
*y-360.0*x*x*x*x*x*x*x*x*y+210.0*x*x*y+120.0*pow(x,10.0)-35.0*y*y*y+
168.0*y*y*y*y*y-252.0*x*x*x*x*x*x*x-840.0*x*x*x*x*x*y-840.0*x*x*y*y*y+
2520.0*x*x*x*x*x*y*y+1008.0*x*x*y*y*y*y+1008.0*x*x*x*x*x*x*y);
z+= zlist[63]*(-45.0*pow(x,10.0)+585.0*x*x*x*x*x*x*x*x*y+630.0*x*x*x*x*x*x*y*y
-630.0*x*x*x*x*x*y*y*y*y-585.0*x*x*y*y*y*y*y+45.0*pow(y,10.0)+72.0*x*x
*x*x*x*x*x-1008.0*x*x*x*x*x*x*x*y+1008.0*x*x*y*y*y*y-72.0*y*y*y*y*y*y
-28.0*x*x*x*x*x*x+420.0*x*x*x*x*x*x*x-420.0*x*x*y*y*y+28.0*y*y*y*y);
z+= zlist[64]*(10.0*pow(x,10.0)-270.0*x*x*x*x*x*x*x*x*y+420.0*x*x*x*x*x*x*x*y*y
+420.0*x*x*x*x*x*x*y*y*y-270.0*x*x*y*y*y*y*y+10.0*pow(y,10.0)-9.0*x*x*x
*x*x*x*x+252.0*x*x*x*x*x*x*x*y-630.0*x*x*x*x*y*y+252.0*x*x*y*y*y*y
-9.0*y*y*y*y);
z+= zlist[65]*(-pow(x,10.0)+45.0*x*x*x*x*x*x*x*x*y-210.0*x*x*x*x*x*x*x*y*y
+210.0*x*x*x*x*x*y*y*y-45.0*x*x*y*y*y*y+y+pow(y,10.0));

```

```

return z;
}

```

## B.3 Calculation of spot positions

```

void TMainForm::DrawSpots() {

    double x,y,dx,dy;
    int i,j;
    double d=lens/pixel;

    for (i=1;i<=rows;i++){
        for (j=1;j<=rows;j++){
            x=-1+(i-1)*(2.0/(rows-1));
            y=-1+(j-1)*(2.0/(rows-1));
            if(x*x+y*y>1+1/(rows+0.0) && isround==0)continue;

            // 1. Order
            dx =zlist[ 1]*(1);
            dx+=zlist[ 2]*(0);

            dy =zlist[ 1]*(0);
            dy+=zlist[ 2]*(1);

            // 2.Order
            dx+=zlist[ 3]*(2*y);
            dx+=zlist[ 4]*(4*x);
            dx+=zlist[ 5]*(-2*x);

            dy+=zlist[ 3]*(2*x);
            dy+=zlist[ 4]*(4*y);
            dy+=zlist[ 5]*(2*y);

            // 3.Order
            dx+=zlist[ 6]*(3*y*y);
            dx+=zlist[ 7]*(9*x*x+3*y*y-2);
            dx+=zlist[ 8]*(6*y*x);
            dx+=zlist[ 9]*(-6*y*x);

            dy+=zlist[ 6]*(6*x*y);
            dy+=zlist[ 7]*(6*x*y);
            dy+=zlist[ 8]*(3*x*x+9*y*y-2);
            dy+=zlist[ 9]*(3*y*y-3*x*x);

            // 4.Order
            dx+=zlist[10]*(-12*x*x*y-4*y*y*y);
            dx+=zlist[11]*(24*x*x*y+8*y*y*y-6*y);
            dx+=zlist[12]*(24*x*x*x+24*x*y*y-12*x);
            dx+=zlist[13]*(-16*x*x*x+6*x);
            dx+=zlist[14]*(4*x*x*x-12*x*y*y);

            dy+=zlist[10]*(-4*x*x*x+12*x*y*y);
            dy+=zlist[11]*(8*x*x*x+24*x*y*y-6*x);
            dy+=zlist[12]*(24*x*x*y+24*y*y*y-12*y);
            dy+=zlist[13]*(16*y*y*y-6*y);
            dy+=zlist[14]*(-12*x*x*y+4*y*y*y);

            // 5.Order

```

```

dx+=zlist[15]*(5*y*y*y*y-30*x*x*y*y+5*x*x*x*x);
dx+=zlist[16]*(30*x*x*y*y-25*x*x*x*x+15*y*y*y*y-12*y*y+12*x*x);
dx+=zlist[17]*(50*x*x*x*x+60*x*x*y*y+10*y*y*y*y-36*x*x-12*y*y+3);
dx+=zlist[18]*(40*y*x*x*x+40*x*y*y*y-24*y*x);
dx+=zlist[19]*(-20*x*y*y*y-60*y*x*x*x+24*y*x);
dx+=zlist[20]*(-20*x*y*y*y+20*y*x*x*x);

dy+=zlist[15]*(20*x*y*y*y-20*x*x*x*y);
dy+=zlist[16]*(20*x*x*x*y+60*x*y*y*y-24*x*y);
dy+=zlist[17]*(40*x*x*x*y+40*x*y*y*y-24*x*y);
dy+=zlist[18]*(10*x*x*x*x+60*x*x*y*y+50*y*y*y*y-12*x*x-36*y*y+3);
dy+=zlist[19]*(-30*x*x*y*y-15*x*x*x*x+25*y*y*y*y-12*y*y+12*x*x);
dy+=zlist[20]*(5*y*y*y*y-30*x*x*y*y+5*x*x*x*x);

// 6.Order
dx+=zlist[21]*(30.0*y*x*x*x*x-60.0*x*x*y*y*y+6.0*y*y*y*y*y);
dx+=zlist[22]*(-120.0*y*x*x*x*x+24.0*y*y*y*y*y+60.0*y*x*x-20.0*y*y*y);
dx+=zlist[23]*(150.0*y*x*x*x*x+180.0*x*x*y*y*y+30.0*y*y*y*y*y-120.0*y*x*x
-40.0*y*y*y+12.0*y);
dx+=zlist[24]*(120.0*x*x*x*x*x+240.0*x*x*x*y*y+120.0*x*y*y*y*y-120.0*x*x*x
-120.0*y*y*x+24.0*x);
dx+=zlist[25]*(-90.0*x*x*x*x*x-60.0*x*x*x*y*y+30.0*x*y*y*y*y
+80.0*x*x*x-12.0*x);
dx+=zlist[26]*(36.0*x*x*x*x*x-120.0*x*x*x*y*y-60.0*x*y*y*y*y
-20.0*x*x*x+60.0*x*y*y);
dx+=zlist[27]*(-6.0*x*x*x*x*x+60.0*x*x*x*y*y-30.0*x*y*y*y*y);

dy+=zlist[21]*(6.0*x*x*x*x*x-60.0*y*y*x*x*x+30.0*y*y*y*y*x);
dy+=zlist[22]*(-24.0*x*x*x*x*x+120.0*y*y*y*y*x+20.0*x*x*x-60.0*x*y*y);
dy+=zlist[23]*(30.0*x*x*x*x*x+180.0*y*y*x*x*x+150.0*y*y*y*y*x-40.0*x*x*x
-120.0*x*y*y+12.0*x);
dy+=zlist[24]*(120.0*y*x*x*x*x+240.0*y*y*y*x*x+120.0*y*y*y*y*y-120.0*y*x*x
-120.0*y*y*y+24.0*y);
dy+=zlist[25]*(-30.0*y*x*x*x*x+60.0*y*y*y*x*x+90.0*y*y*y*y*y-80.0*y*y*y
+12.0*y);
dy+=zlist[26]*(-60.0*y*x*x*x*x-120.0*y*y*y*x*x+36.0*y*y*y*y*y+60.0*y*x*x
-20.0*y*y*y);
dy+=zlist[27]*(30.0*y*x*x*x*x-60.0*y*y*y*x*x+6.0*y*y*y*y*y);

// 7.Order
dx+=zlist[28]*(7.0*y*y*y*y*y-105.0*x*x*y*y*y+105.0*x*x*x*x*y*y
-7.0*x*x*x*x*x*x);
dx+=zlist[29]*(-105.0*x*x*y*y*y-315.0*x*x*x*x*y*y+49.0*x*x*x*x*x
+35.0*y*y*y*y*y-30.0*y*y*y*y+180.0*y*y*x*x-30.0*x*x*x*x);
dx+=zlist[30]*(105.0*x*x*x*x*y-y-147.0*x*x*x*x*x*x+315.0*x*x*y*y*y*y
+63.0*y*y*y*y*y-180.0*y*y*x*x+150.0*x*x*x*x-90.0*y*y*y*y+30.0*y*y
-30.0*x*x);
dx+=zlist[31]*(245.0*x*x*x*x*x+525.0*x*x*x*x*y*y+315.0*x*x*y*y*y*y
+35.0*y*y*y*y*y-300.0*x*x*x*x-360.0*y*y*x*x-60.0*y*y*y*y+90.0*x*x
+30.0*y*y-4.0);
dx+=zlist[32]*(210.0*y*x*x*x*x+420.0*x*x*x*y*y*y+210.0*x*y*y*y*y*y
-240.0*y*x*x*x-240.0*y*y*y*x+60.0*y*x);
dx+=zlist[33]*(-420.0*x*x*x*y*y-y-378.0*y*x*x*x*x*x-42.0*x*y*y*y*y*y
+120.0*y*y*y*x+360.0*y*x*x*x-60.0*x*y);
dx+=zlist[34]*(-126.0*x*y*y*y*y-140.0*x*x*x*y*y+y+210.0*y*x*x*x*x*x
+120.0*y*y*y*x-120.0*y*x*x*x);
dx+=zlist[35]*(-42.0*x*y*y*y*y+140.0*x*x*x*y*y-y-42.0*y*x*x*x*x*x);

dy+=zlist[28]*(42.0*x*y*y*y*y-140.0*x*x*x*y*y+y+42.0*x*x*x*x*x*y);
dy+=zlist[29]*(-140.0*x*x*x*y*y-y-126.0*x*x*x*x*x*y+210.0*x*y*y*y*y*y
-120.0*x*y*y*y+120.0*x*x*x*y);
dy+=zlist[30]*(42.0*x*x*x*x*x+y+420.0*x*x*x*y*y+y+378.0*x*y*y*y*y*y
-120.0*x*x*x*y-360.0*x*y*y*y+60.0*x*y);
dy+=zlist[31]*(210.0*x*x*x*x*x+y+420.0*x*x*x*y*y+y+210.0*x*y*y*y*y*y
-240.0*x*x*x*y-240.0*x*y*y*y+60.0*x*y);

```

```

dy+=zlist[32]*(35.0*x*x*x*x*x*x*x+315.0*x*x*x*x*x*y*y+525.0*x*x*y*y*y*y
+245.0*y*y*y*y*y*y*y-60.0*x*x*x*x*x-360.0*x*x*y*y*y-300.0*y*y*y*y*y+30.0*x*x
+90.0*y*y-4.0);
dy+=zlist[33]*(-315.0*x*x*x*x*x*y*y-63.0*x*x*x*x*x*x*x-105.0*x*x*y*y*y*y
+147.0*y*y*y*y*y*y*y+180.0*x*x*y*y*y+90.0*x*x*x*x*x-150.0*y*y*y*y*y+30.0*y*y
-30.0*x*x);
dy+=zlist[34]*(-315.0*x*x*y*y*y*y*y-105.0*x*x*x*x*x*y*y+35.0*x*x*x*x*x*x*x
+49.0*y*y*y*y*y*y*y-30.0*y*y*y*y*y+180.0*x*x*y*y*y-30.0*x*x*x*x*x);
dy+=zlist[35]*(7.0*y*y*y*y*y*y*y-105.0*x*x*y*y*y*y*y+105.0*x*x*x*x*x*y*y
-7.0*x*x*x*x*x*x*x);

//8.Order
dx+=zlist[36]*(-56.0*y*x*x*x*x*x*x*x+280.0*x*x*x*x*x*y*y*y-168.0*x*x*y*y*y*y*y
+8.0*y*y*y*y*y*y*y);
dx+=zlist[37]*(336.0*y*x*x*x*x*x*x*x-560.0*x*x*x*x*x*y*y*y-336.0*x*x*y*y*y*y*y
+48.0*y*y*y*y*y*y*y-210.0*y*x*x*x*x*x+420.0*y*y*y*y*x*x-42.0*y*y*y*y*y);
dx+=zlist[38]*(-784.0*y*x*x*x*x*x*x*x-560.0*x*x*x*x*x*y*y*y+336.0*x*x*y*y*y*y*y
+112.0*y*y*y*y*y*y*y+840.0*y*x*x*x*x-168.0*y*y*y*y*y-180.0*x*x*y+60.0*y*y*y);
dx+=zlist[39]*(784.0*x*x*x*x*x*x*x*y+1680.0*x*x*x*x*x*y*y*y+1008.0*x*x*y*y*y*y*y
+112.0*y*y*y*y*y*y*y-1050.0*y*x*x*x*x-1260.0*x*x*y*y*y-210.0*y*y*y*y*y
+360.0*x*x*y+120.0*y*y*y-20.0*y);
dx+=zlist[40]*(560.0*x*x*x*x*x*x*x+1680.0*x*x*x*x*x*y*y+1680.0*x*x*x*y*y*y*y
+560.0*x*y*y*y*y*y*y-840.0*x*x*x*x*x-1680.0*x*x*x*y*y-840.0*x*y*y*y*y
+360.0*x*x*x+360.0*x*y*y-40.0*x);
dx+=zlist[41]*(-448.0*x*x*x*x*x*x*x-672.0*x*x*x*x*x*y*y+224.0*x*y*y*y*y*y*y
+630.0*x*x*x*x*x*x+420.0*x*x*x*y*y-210.0*x*y*y*y*y-240.0*x*x*x+20.0*x);
dx+=zlist[42]*(224.0*x*x*x*x*x*x*x-672.0*x*x*x*x*x*y*y-1120.0*x*x*x*y*y*y*y
-224.0*x*y*y*y*y*y*y-252.0*x*x*x*x*x+840.0*x*x*x*y*y+420.0*x*y*y*y*y
+60.0*x*x*x-180.0*x*y*y);
dx+=zlist[43]*(-64.0*x*x*x*x*x*x*x+672.0*x*x*x*x*x*y*y-224.0*x*y*y*y*y*y*y
+42.0*x*x*x*x*x-420.0*x*x*x*y*y+210.0*x*y*y*y*y);
dx+=zlist[44]*(8.0*x*x*x*x*x*x*x-168.0*x*x*x*x*x*y*y+280.0*x*x*x*y*y*y*y
-56.0*x*y*y*y*y*y*y);

dy+=zlist[36]*(-8.0*x*x*x*x*x*x*x+168.0*x*x*x*x*x*y*y-280.0*x*x*x*y*y*y*y
+56.0*x*y*y*y*y*y*y);
dy+=zlist[37]*(48.0*x*x*x*x*x*x*x-336.0*x*x*x*x*x*y*y-560.0*x*x*x*y*y*y*y
+336.0*x*y*y*y*y*y*y-42.0*x*x*x*x*x+420.0*x*x*x*y*y-210.0*x*y*y*y*y);
dy+=zlist[38]*(-112.0*x*x*x*x*x*x*x-336.0*x*x*x*x*x*y*y+560.0*x*x*x*y*y*y*y
+784.0*x*x*y*y*y*y*y+168.0*x*x*x*x*x-840.0*x*y*y*y*y-60.0*x*x*x+180.0*x*y*y);
dy+=zlist[39]*(112.0*x*x*x*x*x*x*x+1008.0*x*x*x*x*x*y*y+1680.0*x*x*x*y*y*y*y
+784.0*x*y*y*y*y*y*y-210.0*x*x*x*x*x-1260.0*x*x*x*y*y-1050.0*x*y*y*y*y
+120.0*x*x*x+360.0*x*y*y-20.0*x);
dy+=zlist[40]*(560.0*x*x*x*x*x*x*x+1680.0*x*x*x*x*x*y*y+1680.0*x*x*y*y*y*y*y
+560.0*y*y*y*y*y*y*y-840.0*x*x*x*x*x-1680.0*x*x*x*y*y-840.0*y*y*y*y*y
+360.0*x*x*y+360.0*y*y*y-40.0*y);
dy+=zlist[41]*(-224.0*x*x*x*x*x*x*x+672.0*x*x*x*y*y*y*y+448.0*y*y*y*y*y*y*y
+210.0*x*x*x*x*x*y-420.0*x*x*y*y*y-630.0*y*y*y*y*y+240.0*y*y*y-20.0*y);
dy+=zlist[42]*(-224.0*x*x*x*x*x*x*x-1120.0*x*x*x*x*x*y*y-672.0*x*x*y*y*y*y*y
+224.0*y*y*y*y*y*y*y+420.0*x*x*x*x*x+840.0*x*x*y*y*y-252.0*y*y*y*y*y
-180.0*x*x*y+60.0*y*y*y);
dy+=zlist[43]*(224.0*x*x*x*x*x*x*x-672.0*x*x*x*y*y*y*y+64.0*y*y*y*y*y*y*y
-210.0*x*x*x*x*x*y+420.0*x*x*y*y*y-42.0*y*y*y*y*y);
dy+=zlist[44]*(-56.0*x*x*x*x*x*x*x+280.0*x*x*x*x*x*y*y-168.0*x*x*x*y*y*y*y
+8.0*y*y*y*y*y*y*y);

// 9.order
dx+=zlist[45]*(9.0*y*y*y*y*y*y*y-252.0*x*x*y*y*y*y*y+630.0*x*x*x*x*x*y*y*y
-252.0*x*x*x*x*x*x*x*y+9.0*x*x*x*x*x*x*x);
dx+=zlist[46]*(-756.0*x*x*y*y*y*y*y-630.0*x*x*x*x*x*y*y*y+1260.0*x*x*x*x*x*x*x*y
-81.0*x*x*x*x*x*x*x*x+63.0*y*y*y*y*y*y*y-56.0*y*y*y*y*y*y+840.0*y*y*y*y*x*x
-840.0*y*y*x*x*x*x+56.0*x*x*x*x*x);
dx+=zlist[47]*(-2520.0*x*x*x*x*x*y*y-2016.0*x*x*x*x*x*x*x*y+324.0*x*x*x*x*x*x*x*x
+180.0*y*y*y*y*y*y*y+840.0*y*y*y*y*x*x+2520.0*y*x*x*x*x-392.0*x*x*x*x*x*x
-280.0*y*y*y*y*y*y+105.0*y*y*y-630.0*x*x*y+105.0*x*x*x*x);

```

```

dx+=zlist[48]*(-756.0*x*x*x*x*x*x*x*x+2520.0*x*x*x*x*x*y*y*y+2016.0*x*x*y*y*y*y*y*y
+252.0*y*y*y*y*y*y*y*y-840.0*x*x*x*x*x*y*y+1176.0*x*x*x*x*x*x*x-2520.0*x*x*y*y*y*y
-504.0*y*y*y*y*y*y+630.0*x*x*y*y-525.0*x*x*x*x+315.0*y*y*y*y-60.0*y*y+60.0*x*x);
dx+=zlist[49]*(1134.0*x*x*x*x*x*x*x*x+3528.0*x*x*x*x*x*x*y*y+3780.0*x*x*x*x*x*y*y*y
+1512.0*x*x*y*y*y*y*y*y+126.0*y*y*y*y*y*y*y-y-1960.0*x*x*x*x*x*x-4200.0*x*x*x*x
*y*y-2520.0*x*x*y*y*y*y-280.0*y*y*y*y*y*y+1050.0*x*x*x*x+1260.0*x*x*y*y+210.0*y
*y*y-y-180.0*x*x-60.0*y*y+5.0);
dx+=zlist[50]*(1008.0*y*x*x*x*x*x*x*x+3024.0*x*x*x*x*x*y*y*y+3024.0*x*x*x*x*y*y*y*y
+1008.0*x*y*y*y*y*y*y-y-1680.0*y*x*x*x*x*x-3360.0*x*x*x*x*y*y-y-1680.0*x*y*y*y*y*y
y+840.0*x*x*x*x*y+840.0*x*y*y*y-120.0*x*y);
dx+=zlist[51]*(-4032.0*x*x*x*x*x*x*y*y-2016.0*y*x*x*x*x*x*x*x-2016.0*x*x*x*x*y*y*y*y
+3360.0*x*x*x*x*y*y+3024.0*y*x*x*x*x*x*x+336.0*x*y*y*y*y*y-y-420.0*x*y*y*y-y-1260.0*
x*x*x*x*y+120.0*x*y);
dx+=zlist[52]*(-2016.0*x*x*x*x*y*y*y*y+1440.0*y*x*x*x*x*x*x*x-576.0*x*y*y*y*y*y*y
+1008.0*x*y*y*y*y*y*y+1120.0*x*x*x*x*y*y-y-1680.0*y*x*x*x*x*x-420.0*x*y*y*y+420.0*x
*x*x*y);
dx+=zlist[53]*(-360.0*x*y*y*y*y*y*y+y+504.0*x*x*x*x*y*y*y*y+1512.0*x*x*x*x*x*x*y*y
-504.0*y*x*x*x*x*x*x*x+336.0*x*y*y*y*y*y-y-1120.0*x*x*x*x*y*y+336.0*y*x*x*x*x*x);
dx+=zlist[54]*(-72.0*x*y*y*y*y*y*y+y+504.0*x*x*x*x*y*y*y*y-504.0*x*x*x*x*x*x*y*y
+72.0*y*x*x*x*x*x*x*x);

dy+=zlist[45]*(72.0*x*y*y*y*y*y*y-y-504.0*x*x*x*x*y*y*y*y+504.0*x*x*x*x*x*x*y*y
-72.0*x*x*x*x*x*x*x*x);
dy+=zlist[46]*(-1512.0*x*x*x*x*y*y*y*y-504.0*x*x*x*x*x*x*y*y+360.0*x*x*x*x*x*x*x*x
+504.0*x*y*y*y*y*y*y-y-336.0*x*y*y*y*y*y+1120.0*x*x*x*x*y*y-y-336.0*x*x*x*x*x*x);
dy+=zlist[47]*(-2016.0*x*x*x*x*x*x*y*y-576.0*x*x*x*x*x*x*x*x+1440.0*x*y*y*y*y*y*y
+1120.0*x*x*x*x*y*y+1008.0*x*x*x*x*x*x-y-1680.0*x*y*y*y*y*y+420.0*x*y*y*y-y-420.0*x
*x*x*y);
dy+=zlist[48]*(2016.0*x*x*x*x*x*x*y+y+4032.0*x*x*x*x*y*y*y*y+2016.0*x*y*y*y*y*y*y
-336.0*x*x*x*x*x*x-y-3360.0*x*x*x*x*y*y-y-3024.0*x*y*y*y*y*y+420.0*x*x*x*x+y+1260.0*x
*y*y-y-120.0*x*y);
dy+=zlist[49]*(1008.0*x*x*x*x*x*x*x*x+3024.0*x*x*x*x*x*x*y*y+3024.0*x*x*x*x*y*y*y*y
+1008.0*x*y*y*y*y*y*y-y-1680.0*x*x*x*x*x*x-y-3360.0*x*x*x*x*y*y-y-1680.0*x*y*y*y*y*y
y+840.0*x*x*x*x*y+840.0*x*y*y*y-120.0*x*y);
dy+=zlist[50]*(126.0*x*x*x*x*x*x*x*x+1512.0*x*x*x*x*x*x*x*x*y+3780.0*x*x*x*x*x*x*y*y
+3528.0*x*x*x*y*y*y*y*y+1134.0*y*y*y*y*y*y*y-y-280.0*x*x*x*x*x*x-2520.0*x*x*x*x
*y-y-4200.0*x*x*x*y*y*y-y-1960.0*y*y*y*y*y*y+210.0*x*x*x*x+1260.0*x*x*y*y+1050.0*y
*y*y-y-60.0*x*x-180.0*y*y+5.0);
dy+=zlist[51]*(-2016.0*x*x*x*x*x*x*x*x-2520.0*x*x*x*x*x*x*x*x-2520.0*x*x*x*x*x*x*y
+756.0*y*y*y*y*y*y*y+y+2520.0*x*x*x*x*x*x*y+504.0*x*x*x*x*x*x*x+840.0*x*x*x*y*y*y
-1176.0*y*y*y*y*y*y-630.0*x*x*x*x-315.0*x*x*x*x+525.0*y*y*y*y-60.0*y*y+60.0*x*x);
dy+=zlist[52]*(-2520.0*x*x*x*x*x*x*y+y+180.0*x*x*x*x*x*x*x*x-2016.0*x*x*x*x*x*x
+324.0*y*y*y*y*y*y*y+y+2520.0*x*x*x*y*y*y+840.0*x*x*x*x*x*x-y-280.0*x*x*x*x*x*x
-392.0*y*y*y*y*y*y+105.0*y*y*y-y-630.0*x*x*x*y+y+105.0*x*x*x*x);
dy+=zlist[53]*(-1260.0*x*x*x*y*y*y*y+y+630.0*x*x*x*x*x*x*x*x+756.0*x*x*x*x*x*x*x*x
-63.0*x*x*x*x*x*x*x*x+81.0*y*y*y*y*y*y*y-y-56.0*y*y*y*y*y*y+840.0*x*x*x*y*y*y
-840.0*x*x*x*x*x*x*y+y+56.0*x*x*x*x*x*x);
dy+=zlist[54]*(9.0*y*y*y*y*y*y*y-y-252.0*x*x*x*x*y*y*y+y+630.0*x*x*x*x*x*x*y*y
-252.0*x*x*x*x*x*x*x*x+y+9.0*x*x*x*x*x*x*x*x);

// 10.order
dx+=zlist[55]*(10.0*y*y*y*y*y*y*y-y-360.0*x*x*x*y*y*y*y*y
+1260.0*x*x*x*x*x*x*y*y*y-y-840.0*x*x*x*x*x*x*x*x+y+90.0*y*x*x*x*x*x*x*x*x);
dx+=zlist[56]*(-1440.0*x*x*x*y*y*y*y*y+y+3360.0*x*x*x*x*x*x*x*x*y*y
-720.0*y*x*x*x*x*x*x*x*x+80.0*y*y*y*y*y*y*y-y-72.0*y*y*y*y*y*y
+1512.0*y*y*y*y*y*x*x-2520.0*y*y*y*x*x*x*x+504.0*y*x*x*x*x*x*x);
dx+=zlist[57]*(-6300.0*x*x*x*x*x*x*y*y-y-2520.0*x*x*x*x*x*x*x*x*y
+2430.0*y*x*x*x*x*x*x*x-1080.0*x*x*x*y*y*y*y*y+y+270.0*y*y*y*y*y*y*y
+3024.0*y*y*y*y*x*x+5040.0*y*y*y*x*x*x-3024.0*y*x*x*x*x*x
-432.0*y*y*y*y*y+y+168.0*y*y*y-y-1680.0*y*y*y*x*x+840.0*y*x*x*x);
dx+=zlist[58]*(-6720.0*y*y*y*x*x*x*x-4320.0*y*x*x*x*x*x*x*x
+2880.0*y*y*y*y*y*x*x+480.0*y*y*y*y*y*y*y+y+5040.0*y*y*y*x*x*x
+7056.0*y*x*x*x*x*x-3024.0*y*y*y*x*x-1008.0*y*y*y*y*y
-3360.0*y*x*x*x*x+672.0*y*y*y-y-140.0*y*y+y+420.0*x*x*y);
dx+=zlist[59]*(3780.0*y*x*x*x*x*x*x+11760.0*y*y*y*x*x*x*x*x

```

```

+12600.0*y*y*y*y*y*x*x*x*x+5040.0*y*y*y*y*y*y*x*x+420.0*y*y*y*y*y*y*y*y
-7056.0*y*x*x*x*x*x*x-15120.0*y*y*y*y*x*x*x*x-9072.0*y*y*y*y*y*x*x
-1008.0*y*y*y*y*y*y*y+4200.0*y*x*x*x*x+5040.0*y*y*y*x*x+840.0*y*y*y*y*y
-840.0*x*x*y-280.0*y*y*y+30.0*y);
dx+=zlist[60]*(2520.0*x*x*x*x*x*x*x*x*x+10080.0*x*x*x*x*x*x*x*y
+15120.0*x*x*x*x*x*x*y*y*y+10080.0*x*x*x*x*y*y*y*y+2520.0*x*y*y*y*y*y*y
-5040.0*x*x*x*x*x*x*x-15120.0*x*x*x*x*x*x*y-15120.0*x*x*x*x*y*y*y
-5040.0*x*y*y*y*y*y+3360.0*x*x*x*x*x+6720.0*x*x*x*y+3360.0*x*y*y*y
-840.0*x*x*x-840.0*x*y*y+60.0*x);
dx+=zlist[61]*(-30.0*x+4032.0*x*x*x*x*x*x*x+560.0*x*x*x+6048.0*x*x*x*x*x*y
-2016.0*x*x*y*y*y*y-5040.0*x*x*x*x*x*x*x*x*y-2520.0*x*x*x*x*x*y*y
+1680.0*x*x*x*x*y*y*y*y+1260.0*x*y*y*y*y*y*y-2520.0*x*x*x*x*x
-2100.0*x*x*x*x*x*x*x*x*x+840.0*x*y*y*y-1680.0*x*x*x*y);
dx+=zlist[62]*(-2016.0*x*x*x*x*x*x*x-140.0*x*x*x+6048.0*x*x*x*x*x*y
+10080.0*x*x*x*x*y*y*y+2016.0*x*y*y*y*y*y-2880.0*x*x*x*x*x*x*x*y
-10080.0*x*x*x*x*x*x*x*y-6720.0*x*x*x*x*y*y*y*y-720.0*x*y*y*y*y*y*y
+1008.0*x*x*x*x*x+1200.0*x*x*x*x*x*x*x*x+420.0*x*y*y-1680.0*x*y*y*y
-3360.0*x*x*x*y);
dx+=zlist[63]*(-2520.0*x*x*x*x*y*y*y*y+3780.0*x*x*x*x*x*y*y*y
+4680.0*x*x*x*x*x*x*x*x*y-450.0*x*x*x*x*x*x*x*x*x-1170.0*x*y*y*y*y*y*y
+2016.0*x*x*y*y*y*y-6048.0*x*x*x*x*x*x*x*y+576.0*x*x*x*x*x*x*x-840.0*x*y*y*y
+1680.0*x*x*x*x*y-168.0*x*x*x*x*x);
dx+=zlist[64]*(-540.0*x*y*y*y*y*y*y+1680.0*x*x*x*x*y*y*y*y
+2520.0*x*x*x*x*x*x*y*y*y-2160.0*x*x*x*x*x*x*x*x*y+100.0*x*x*x*x*x*x*x*x
+504.0*x*y*y*y*y*y-2520.0*y*y*y*y*x*x*x+1512.0*x*x*x*x*x*x*y
-72.0*x*x*x*x*x*x*x);
dx+=zlist[65]*(-90.0*x*y*y*y*y*y*y+840.0*x*x*x*x*y*y*y*y
-1260.0*x*x*x*x*x*x*y*y*y+360.0*x*x*x*x*x*x*x*x*y-10.0*x*x*x*x*x*x*x*x);

dy+=zlist[55]*(10.0*x*x*x*x*x*x*x*x*x-360.0*x*x*x*x*x*x*x*y
+1260.0*x*x*x*x*x*x*y*y*y-840.0*x*x*x*x*y*y*y*y+90.0*x*y*y*y*y*y);
dy+=zlist[56]*(-80.0*x*x*x*x*x*x*x*x+1440.0*x*x*x*x*x*x*x*y
-3360.0*x*x*x*x*y*y*y*y+720.0*x*y*y*y*y*y*y+72.0*x*x*x*x*x*x*x
-1512.0*x*x*x*x*x*x*y+2520.0*x*x*x*x*y*y*y-504.0*x*y*y*y*y);
dy+=zlist[57]*(270.0*x*x*x*x*x*x*x*x-1080.0*x*x*x*x*x*x*x*y
-6300.0*x*x*x*x*x*x*y*y*y-2520.0*x*x*x*x*y*y*y*y+2430.0*x*y*y*y*y*y
-432.0*x*x*x*x*x*x*x+3024.0*x*x*x*x*x*x*y+5040.0*x*x*x*x*y*y
-3024.0*x*x*y*y*y*y+168.0*x*x*x*x*x-1680.0*x*x*x*x*y+840.0*x*y*y*y);
dy+=zlist[58]*(-480.0*x*x*x*x*x*x*x*x-2880.0*x*x*x*x*x*x*x*y
+6720.0*x*x*x*x*x*y*y*y+4320.0*x*y*y*y*y*y*y+1008.0*x*x*x*x*x*x*x
+3024.0*x*x*x*x*x*x*y-5040.0*x*x*x*x*y*y-7056.0*x*y*y*y*y*y
-672.0*x*x*x*x*x+3360.0*x*y*y*y+140.0*x*x*x-420.0*x*y*y);
dy+=zlist[59]*(420.0*x*x*x*x*x*x*x*x+5040.0*x*x*x*x*x*x*x*y
+12600.0*x*x*x*x*x*x*y*y+y+11760.0*x*x*x*x*y*y*y+y+3780.0*x*y*y*y*y*y
-1008.0*x*x*x*x*x*x*x-9072.0*x*x*x*x*x*x*y-15120.0*x*x*x*x*y*y*y
-7056.0*x*y*y*y*y+y+840.0*x*x*x*x*x+5040.0*x*x*x*x*y+4200.0*x*y*y*y
-280.0*x*x*x-840.0*x*y*y+30.0*x);
dy+=zlist[60]*(2520.0*x*x*x*x*x*x*x*x+y+10080.0*x*x*x*x*x*x*x*y
+15120.0*x*x*x*x*x*x*y*y+y+10080.0*x*x*x*y*y*y+y+2520.0*y*y*y*y*y*y
-5040.0*x*x*x*x*x*x*x-15120.0*x*x*x*x*x*x*y-15120.0*x*x*x*y*y*y
-5040.0*y*y*y*y*y+y+3360.0*x*x*x*x*x+y+6720.0*x*x*x*y+y+3360.0*y*y*y
-840.0*x*x*x-840.0*y*y+y+60.0*y);
dy+=zlist[61]*(30.0*y+2100.0*y*y*y*y*y+y-6048.0*x*x*x*y*y*y
+2016.0*x*x*x*x*x*x*x-4032.0*y*y*y*y*y-y-1260.0*x*x*x*x*x*x*x
-1680.0*x*x*x*x*x*x*x*y+y+2520.0*x*x*x*x*x*y+y+5040.0*x*x*x*y*y*y
-560.0*y*y+y+2520.0*y*y*y-y-840.0*x*x*x*x+y+1680.0*x*x*x*y);
dy+=zlist[62]*(1200.0*y*y*y*y*y+y+6048.0*x*x*x*y*y+y+2016.0*x*x*x*x*x*x
+10080.0*x*x*x*x*x*x*x-2016.0*y*y*y*y-y-720.0*x*x*x*x*x*x*x
+420.0*x*x*x-y-6720.0*x*x*x*x*x*x*x*x*y-10080.0*x*x*x*x*x*x*y
-2880.0*x*x*x*y*y*y-y-140.0*y*y+y+1008.0*y*y*y-y-1680.0*x*x*x*x
-3360.0*x*x*x*y);
dy+=zlist[63]*(1170.0*x*x*x*x*x*x*x*x+y+2520.0*x*x*x*x*x*x*x*y
-3780.0*x*x*x*x*x*x*x*y-4680.0*x*x*x*y*y*y+y+450.0*y*y*y*y*y
-2016.0*x*x*x*x*x*x*x+y+6048.0*x*x*x*y*y-y-576.0*y*y*y*y+y+840.0*x*x*x*x
-1680.0*x*x*x*y+y+168.0*y*y*y);

```



---

```

dy+=zlist[64]*(-540.0*x*x*x*x*x*x*x*x*x*x*y+1680.0*x*x*x*x*x*x*x*y*y*y
+2520.0*x*x*x*x*x*y*y*y*y*y*y-2160.0*x*x*y*y*y*y*y*y*y*y+100.0*y*y*y*y*y*y*y*y*y
+504.0*x*x*x*x*x*x*x*y-2520.0*x*x*x*x*y*y*y+1512.0*x*x*y*y*y*y*y*y
-72.0*y*y*y*y*y*y*y*y);
dy+=zlist[65]*(90.0*x*x*x*x*x*x*x*x*x*y-840.0*x*x*x*x*x*x*x*y*y*y
+1260.0*x*x*x*x*x*y*y*y*y*y-360.0*x*x*y*y*y*y*y*y*y+10.0*y*y*y*y*y*y*y*y*y);

spotx[i][j]= 0.5*768+(i-0.5*rows-0.5)*d+dx*(focal*1000)/pixel    ;
spoty[i][j] = 0.5*576+(j-0.5*rows-0.5)*d +dy*(focal*1000)/pixel    ;
DrawSpotNew(spotx[i][j],spoty[i][j],10,1);
}

```

# References

- [Art95] Pablo Artal, Susana Marcos, Rafael Navarro, David R. Williams  
*Odd aberrations and double-pass measurement of retinal image quality* Journal of the  
Optical Society of America A, Vol. 12, No. 2, pp. 195-201 (1995)
- [Atc00] David A. Atchinson, George Smith  
*Optics of the Human Eye*  
Butterworth Heinemann Oxford Auckland Boston (2000)
- [Bas00] Björn Baschek  
*Entwicklung eines Hartmann-Shack-Wellenfrontensensors für sphäro-zylindrisch vor-  
korrigierte Messungen am menschlichen Auge*  
Diplomarbeit, University of Heidelberg (2000)
- [Bil02] Bille, Harner, Loesel  
*New Frontiers in Vision and Refractive Surgery*  
Springer Berlin, Heidelberg New York (2002)
- [Bor89] M. Born, E. Wolf  
*Principles of Optics: Electromagnetic Theory of Propagation, Interference, and  
Diffraction of Light*  
Cambridge University Press (1989)
- [Buc75] R.A. Buchroeder, R.B. Hooker  
*Aberration Generator*  
Applied Optics, 14, 2476 (1975)
- [Fis99] Burkhardt Fischer  
*Blickpunkte*  
Verlag Hans Huber, Bern (1999)

- 
- [Fri60] D.L. Fridge  
*Aberration Synthesizer*  
J. Opt. Soc. Am., 50, 87 (1960)
- [Hec02] Eugene Hecht  
*Optics Fourth Edition*  
Addison Wesley Longman, Inc. (2002)
- [Ids02] IDS Imaging Development Systems GmbH  
*The FALCON/EAGLE family Handbuch*  
IDS Imaging Development Systems GmbH (2002)
- [Lia91] J.Liang  
*A new method of precisely measure the wave aberrations of the human eye with a Hartmann-Shack wavefront sensor*  
Dissertation, University of Heidelberg (1991)
- [Lia94] J.Liang  
*Objective measurement of wave aberrations of the human eye with use of a Hartmann-Shack wavefront sensor*  
Opt. Soc. Am. 11,1949 (1994)
- [Mal 92] Daniel Malacara  
*Optical Shop Testing*  
John Wiley & Sons (1992)
- [Mil98] Matrox  
*MIL Lite - User Guide and Command Reference*  
Matrox Electronix Systems Ltd. (1998)
- [Meh96] Dieter Mehling  
*Bestimmen von Sehhilfen*  
Ferdinand Enke Verlag, Stuttgart (1996)
- [Mol96] V.V.Molebny  
*Adaptive optics for measuring eye refraction distribution*  
SPIE Vol. 2903 147 (1996)

- 
- [Mue98] Frank Müller  
*Hartmann-Shack Wellenfrontsensor in der Ophthalmologie*  
Diplomarbeit, University of Heidelberg (1998)
- [Mue01] Frank Müller  
*Konzeption und Entwicklung eines adaptiv-optisch korrigierten Laser-Scanning  
Retina-Tomographen*  
Dissertation, University of Heidelberg (2001)
- [Mue98] Frank Müller  
*Weiterentwicklung eines Hartmann-Shack-Wellenfrontsensors zur Verwendung am  
menschlichen Auge*  
Diplomarbeit, University of Heidelberg (1998)
- [Pap99] Ulrich von Pape  
*Aufbau eines kompakten Hartmann-Shack-Wellenfrontsensors zur Vermessung der  
Hornhauttopographie und der Refraktion des Auges*  
Diplomarbeit, University of Heidelberg (1999)
- [Pap01] Ulrich von Pape  
*Wavefront Sensing in the Human Eye*  
Dissertation, University of Heidelberg (2002)
- [Rat95] H. Rath  
*Messung der Hornhauttopographie mit Hilfe eines Hartmann-Shack-Wellenfrontsensors*  
Diplomarbeit, University of Heidelberg (1995)
- [Sch95] R. Schmidt, G. Thews  
*Physiologie des Menschen*  
Springer Verlag Berlin Heidelberg New York (1995)
- [Sch97] Michael Schottner  
*Aufbau eines kompakten Hartmann-Shack-Wellenfrontsensor für der Einsatz in der  
Ophthalmologie*  
Diplomarbeit, University of Heidelberg (1997)
- [Sha71] Ben Platt, Roland V.Shack  
*Lenticular Hartmann Screen*

---

Opt. Science Center Newsletter, University of Ariyona, 5,1 (1971)

[Str98] Bjarne Stroustrup

*Die C++ -Programmiersprache*

Addison Wesley Longman (1998)

[Wan80] J.Y. Wang, D.E. Silva

*Wave-front interpretation with Zernike polynomials*

Applied Optics, Vol 19, No. 9, pp. 1510-1518 (1980)

[Wei02] Eric W. Weisstein

*Eric Weisstein's World of Mathematics (MathWorld<sup>TM</sup>)*

<http://mathworld.wolfram.com> (05/01/2002)

Wolfram Research, Inc.

[Zer34] Fritz Zernike

Physica 1, 689 (1934)

# Acknowledgements

My Thanks go to...

- Prof. Dr. Josef Bille for the possibility to do such an interesting work in the field of medical physics and his great interest in interdisciplinary work in the field of ophthalmology
- Prof. Dr. Brenner for his interest in this work and the willingness to take on the second referee
- Denwood Ross for numerous helpful discussion and the support from Vistakon
- Albert Bijlsma and Dr. Stefan Bäumer for the cooperation with Philips, Eindhoven
- Dr. Ingo Müller-Vogt for the reading of the manuscript and for the unforgettable time inside and outside the lab
- Dipl.-Phys. Björn Baschek for his great assistance and skills during the first experiments
- Dr. Christian Rumpf for the unforgettable time having lunch
- Dr. Frank Müller and Dr. Ulrich von Pape for numerous helpful discussions
- Dr. Ralf Kessler, Dr. Alexander Türpitz and Dipl.-Phys. Jürgen Fröhlich for the time we shared